Design, Construction, and Testing of an Intermediate Strain Rate Loading Device for Synchrotron-Based Testing of Geological Materials

By
Andrew Kearney Robinson

A Master's Essay submitted to Johns Hopkins University in conformity with the requirements for the degree of Master of Science in Mechanical Engineering

Baltimore, MD
September 2016

Abstract

Brittle geological materials are very common building materials for impact and penetration resistant structures. From bunkers dug into rock to gabions filled with sand, many military and civilian protective structures use these materials. Although impact events are dynamic events by nature, the strain rate dependent constitutive behavior and deformation mechanisms of these geologic materials are poorly understood. This study focuses on the dynamic brittle fracture process that develops in these impact events.

Recent advances in user facilities with synchrotron radiation sources now allow for the interrogation of dynamic fracture through the use of phase contrast imaging. A phase contrast imaging experiment has been conducted on millimeter-sized notched three point bend specimens of single crystal α-quartz. Instead of using a Kolsky bar based loading solution, a piezoelectric actuator driven system, PAIRLS (Piezo Actuated Intermediate Rate Loading System), has been developed to allow for acquisition of force and displacement data across the low and intermediate strain rate ranges. This essay outlines the design process of this device with proof-of-concept mechanical tests and accompanying in-situ phase contrast imaging results.

Acknowledgements

There are multitudes of people who deserve my humble thanks for helping me throughout the course of my studies. No one deserves more thanks than my parents. My Mom has always been good at showing us the brighter side of life no matter what happens. Although my Dad passed away when I was in second grade, I'm sure his engineering background and mentoring strategies early in life are the main reason I enjoy engineering to this day. I have to thank my brother for all the fun we had as kids blowing things up in the backyard with gasoline, dry ice bombs, and Mom's hairspray. Also, a thanks goes to my brother for joining in while we explored the mechanical failure of objects around the house. It really helped divert some of the blame when it was time for discipline. Lastly, I have to thank my sister for loaning us a few Barbie dolls to perform skull fracture experiments even though she stopped loaning them to us after that. It's pretty clear to me that all those childhood experiments in failure analysis and dynamic fracture were a precursor to the work I do today.

On the professional side of things, I have to first and foremost thank my advisor, Professor K.T. Ramesh. Thank you for always being honest and strait forward regarding career advice. Despite my decision to leave early,

you still worked hard to get me hired at my dream job. I can't thank you enough for always considering the interests of the student first. I owe you a huge debt for this opportunity. I also wish to thank Professor Todd Hufnagel who wrote all the proposals for beam time at APS, and organized the trips to Chicago. Without his intricate knowledge of synchrotron facilities, this work would not have been possible. A thanks also goes to the Defense Threat Reduction Agency for sponsoring this work. The DTRA mission is very important, and I hope that this work has been useful to that mission.

Lastly, I must thank all the graduate students who provided academic assistance and entertainment along the way. I thank Debjoy Mallick and Amy Dagro for providing a bed to sleep in during the writing of this essay. I have to thank Meng Zhao and Vignesh Kannan for the lengthy discussions on mechanics and philosophy in Latrobe 26 and showing me the best Chinese and Indian food I've ever had. A big thanks goes to Dr. Andrew Fwu Tay Leong for spending 90 hours notching specimens with me in Latrobe the week before our first APS trip. Without the students and post-docs of HEMI, the east coast would have been much less fun.

Table of Contents

List of Figures

1 Introduction and Background

1.1 Motivation

The rate-dependent fracture behavior of brittle solids is of exceptional importance in the design of ramparts, gabions, bunkers, and other structures built from geologic materials. Unlike concrete or other modern building materials, geologic materials like sand, quartz, sandstone, and basalt can often be found in great abundance very close to the building site with little extraction or mining effort. A historical example of this is the use of gabions for fortress defense. These are portable containers that, when filled with local granular geologic materials, can be stacked to form bunker walls that are far cheaper and more portable than an equivalent concrete structure. A modern example of this medieval technology in modern militaries is the HESCO® bastion used in todays modern militaries for rapid construction of fortified forward operating bases. Not only are granular geologic materials often used, but, as in the case with many more fortified bunkers like Cheyenne Mountain, the building can be cut into existing solid rock formations [1]. Thus, by avoiding large volume concrete pours, these geologic materials can offer large cost benefits in bunker construction. Although these materials are ubiquitous, their strain-rate-dependent

deformation mechanisms and resulting constitutive behavior are still poorly understood.

There are a multitude of deformation and failure processes involved in an impact on geologic materials, which may contribute to their constitutive behavior. There are several proposed deformation mechanisms that may be active in geological materials prior to fracture [2]. Also, the suite of active mechanisms likely varies when the material is under a compressive stress as opposed to a tensile stress [3]. These mechanisms will likely be active in areas of high strain such as in front of a crack tip and may vary with strain rate [4]. The study of these mechanisms, and the progression from pristine material to fractured material has been focused to just two techniques.

The most commonly used experimental approaches to investigate failure processes can be categorized into in-situ or post-mortem techniques. The first, in-situ techniques have been traditionally limited to studies using optical cameras. These optical in-situ visualizations of fracture patterns are limited in that they can only retrieve surface level information such as temperature and strain [5]. In the past, the only way to retrieve more than in-situ surface information was to test transparent materials. For example, in dynamic fracture experiments using a transparent PMMA, stress waves were

found to emanate from the crack front through a backlit shadowgraph technique [6]. In the second approach, post-mortem fractography and materials characterization of fractured specimens has contributed to the discovery of phenomena that likely occurred inside the specimen during deformation but was not possible to see with in-situ surface visualization [7]. However, as with all post-mortem techniques, it can be unclear to the investigator if the observed phenomena occurred during the event or in some relaxation stage after the event. Thus, there exists a large gap between what can be measured during an experiment versus what can be measured afterwards. This gap can be reduced to a certain extent by recent advances in high-speed photography in combination with high brightness synchrotron light sources.

High-speed optical imaging techniques are inherently limited by several factors. Exposure times must be short enough to minimize blurring of moving objects, but long enough for a sufficient amount of photons to contact the sensor and form coherent contrast. This trade off has led to the use of increasingly powerful flash bulbs and laser systems for optical images to attain enough contrast at frame rates in excess of 10^5 fps. Synchrotron light sources run at fluences so high that the pulse length of the x-ray beam can be in the 10's of picoseconds to form a sufficiently bright image [8]. In

fact, the length of the pulse must be capped at 100's of picoseconds to avoid damage to upstream optics, sample materials, scintillators and downstream optics. Thus, imaging-using synchrotrons is uniquely suited for high rate fracture experiments.

Synchrotron light sources can further mitigate the trade-offs between post-mortem analysis and in-situ sample surface imaging through the use of phase-contrast imaging. Using this technique, entire crack planes can be visualized in-situ instead of just the intersection of the crack plane and sample surface [9,10]. Although x-ray phase contrast imaging techniques can theoretically image down into near sub micron level resolutions, current scintillators and beam dimensions typically restrict resolutions to 2 or 3 μm/pixel and view fields of several millimeters, respectively [10]. Thus, to make use of these new techniques, existing materials testing techniques must be adapted for use in synchrotron environments.

1.2 Strain Rate Dependence in Materials

As with many materials testing efforts, the study of constitutive behavior and the corresponding deformation mechanisms often occurs in the context of strain rate through the use of various loading devices. At the low

end of strain rates from creep testing ($<10^{-6}$ s^{-1}) to quasi-static ($10^{-6} – 10^{-1}$ s^{-1}) testing, a servo-hydraulic testing machine is typically utilized. High strain rates of ($10^{2} – 10^{5}$ s^{-1}) can typically be accessed using Kolsky bars of various diameters and using various sample sizes. Above the 10^{5} s^{-1} range, plate-impact systems, gas guns, and laser-driven micro flyer plates can operate into the 10^{7} s^{-1} range or above [11]. Although this range of accessible strain rates can span over 15 orders of magnitude, there are still experimental design difficulties for geologic and brittle materials for many small regions in this strain rate continuum.

A particular difficulty is the so-called intermediate strain rate range spanning 10^{0} s^{-1} to 10^{2} s^{-1}. During impact events of concern for bunker design or penetrator design, there is often a region of material deformation far enough from the impact point that experiences strain rates in this intermediate rate regime. For this range, most servo-hydraulic systems do not have crosshead velocities high enough, and Kolsky bars cannot typically be modified enough to achieve these lower strain rates for brittle materials. Thus, for geologic materials to be tested in this intermediate strain rate regime, a customized intermediate strain rate testing device must be designed.

1.3 Intermediate Rate Testing

There have been several efforts in the past to access the intermediate strain rate regime using a variety of loading devices. Perhaps the most common system used for this range is a drop tower. Drop towers make use of a tup, which, after release, falls in a guided path, due to gravity, towards the sample. Once in contact with the sample, the tup has the velocity to deform the material under an intermediate strain rate. There are multiple standard industrial quality control tests and ASTM standards, which have been developed using drop-weight systems [12]. Intermediate rates can also be achieved through the modification of a servo-hydraulic system by stacking hydraulics in series, then simultaneously triggering them [13]. However, these intermediate strain rate testing systems have several drawbacks, including accuracy and portability, when testing small samples in a synchrotron environment.

1.4 Testing In Synchrotron Environments

For testing in a synchrotron environment, several space limitations must be taken into account. First, synchrotron facilities are typically far from an investigators work location. Furthermore, testing systems cannot usually be stored at the synchrotron facility because floor space is in short supply

and other users may need to temporarily store equipment between experiments. Thus, it is ideal to have equipment that is portable enough to take in a carry-on (22 cm x 35 cm x 56 cm) sized luggage container to ensure it is handled with care during travel. Second, since upstream optics at most synchrotrons generate beams with diameters of roughly 2mm, the samples being tested are usually also on the 1mm to 10mm scale. Both these aspects of synchrotron testing point to the use of a small (<10000 cm^3) loading device as a potential solution. Although small loading devices naturally lend themselves to more precise results, the precision needed for triggering at a synchrotron is a paramount design concern.

Running experiments at a synchrotron facility typically requires the triggering of multiple pieces of equipment at times that must be accurate to the nanosecond scale. For example, in a 5 Mfps experiment, the window to capture the crack nucleation and propagation is approximately 25 μs with current camera technology. Thus, the triggering of the upstream shutters, galvanometers, and camera relative to the sample loading must be accurate to within this window. To catch nucleation, triggering is always biased to trigger too early, so the loading device must consistently cause crack nucleation, and ideally full fracture within the 25 μs window. If this critical constraint cannot be met, hours of valuable beam time will be wasted, and

because data can only be gathered 1 or 2 times per year, it is absolutely critical that the device be as repeatable and predictable as possible. Because of the high value of repeatability and low temporal jitter in synchrotron experiments, the actuator type must be chosen carefully.

To meet the unique demands of intermediate strain rate testing of materials in a synchrotron environment, several design considerations must be taken into account. This design process is detailed in the following section. First, design goals are defined with secondary, lower priority, goals. Next, because the apparatus uses three point bending samples, an overview of the three point bend testing technique is included with some discussion of the sample design process. Last, a comprehensive discussion of each major design feature from the actuator to the loading frame is included.

2 Experimental Design

The design of a device to meet the testing requirements of intermediate rate testing in a synchrotron environment can be broken down into several major categories. First, a set of goals and constraints must be defined to restrict the scope of the project. Second, for the particular testing technique (three point bending in this case), there are special design considerations that need to be addressed. Third, for the particular technique, the design of the sample must be optimized. Last, the design of certain components such as the actuator, the loading frame, or the sample stage must be tailored to meet the goals outlined from the outset.

2.1 Design Goals

The design goals were split into two categories because of the possibility that the device may be used for additional projects or testing outside of the originally funded purpose. The primary goals outline what must be accomplished for the device to successfully test geological materials for the DTRA funded project. The secondary goals consist of goals that, if met, would benefit the materials testing efforts for other funded research projects.

2.1.1 Primary Goals

Below are the primary design constraints for the PAIRLS. These were chosen based on conversations and meetings with the DTRA research team.

1. The device should be small enough to transport via carry-on luggage on any domestic North American airline.
2. The device should output the time-dependent displacement of the top of the beam during loading.
3. The device should output the time-dependent force transmitted through the supports of the beam.
4. The device should be able to consistently acquire data in the collection window during the fracture process. To effectively match actuation time with imaging time, an actuation time repeatability less than +/- 100 ns will likely be required. Actuation time is defined as the time from actuator triggering to reaching 70% of max displacement. This requirement ensures that the fracture event can be reliably captured in the context of the synchrotron shutter triggering sequence.

5. The device should be able to test 3 point bend samples of quartz, sandstone, and gneiss with lengths from 4mm to 10mm. Height and width of beams will be less than 2mm for all lengths.

6. The compliance of the superstructure should be small enough to reliably induce fracture in beams up to 100 N loads.

7. The device should be able to test three point bend specimens up to notch tip strain rates of 100 s^{-1}.

2.1.2 Secondary Goals

8. The device should be able to reliably induce fracture in 10mm long beams of boron carbide.

9. The device should be functional also as a fatigue loading device. This functionality should be able to produce fatigue pre-cracks in notched beams.

2.2 Three Point Bend Testing

Due to the small fields of view used for synchrotron-based experiments, the origin site of the crack must be in the field of view prior to the experiment. To accomplish this, crack nucleation can be promoted through the use of a notch or fatigue pre crack [5]. In practice, the fracture properties of materials are usually quantified using a fracture toughness value representative of the fracture mode. ASTM has outlined in detail how

to perform fracture toughness testing for advanced ceramics using three-point bend specimens with pre-cracks or notches to promote stress concentration [14]. A schematic taken from the ASTM standard of the sample geometry and loading is shown below.

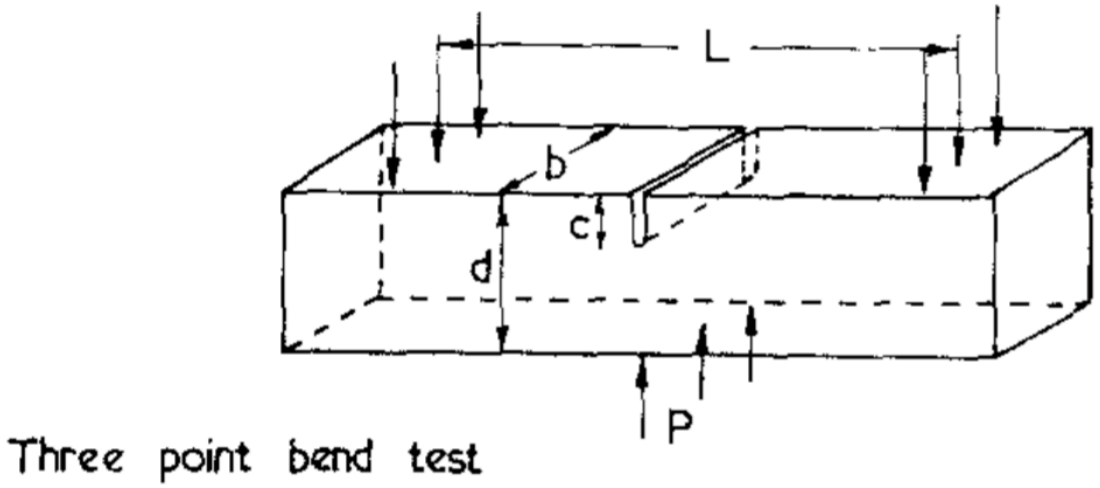

Figure 1 - The three point bend test with corresponding dimensions as presented in ASTM standard 1412

To obtain an estimate of the K_1 as a function of the force on the top of the beam, P, the Equations 1 and 2 can be used as long as a sharp, vertical crack is assumed to exist at the notch tip [14].

$$G_{1c} = \frac{P_f^2 L^2}{8b^2 d^3 E} * [31.7 * (\frac{c}{d}) - 64.8 * (\frac{c}{d})^2 + 211 * (\frac{c}{d})^3] \qquad (1)$$

$$K_{1c} = \sqrt{\frac{EG_{1c}}{1-\nu^2}} \qquad (2)$$

The strain rates in front of the crack tip may vary locally due to asperities, but can be roughly estimated regionally by a finite element analysis at the notch tip in a similar fashion to what was done by Casem et. al. for un-notched three point bending samples [15]. Prior to Casem et. al. in 2015, there have been many previous attempts to measure the dynamic fracture toughness of ceramics using various modifications of the three point bend Kolsky bar technique [16-18]. These attempts, with the exception of Casem et. al., performed little exploration of the strain rates experienced by the material prior to fracture due to the complexity of the sample geometry. Casem et. al. identified peak strain rates of ~15 s^{-1} for un-notched beams near the location of maximum tensile strain using a commercial FEM software. However, when using a notched beam, strain accumulates locally at the notch over similar time scales to un-notched beams, so strain rates for notched specimens may be above the intermediate range when using a Kolsky bar technique. To accomplish intermediate strain rates with a predictable location of fracture, specimen geometry and technique must be modified beyond the Kolsky bar technique. Thus, for strain rates from 10^0 – 10^2 s^{-1}, both the design of the loading device and sample design play critical roles.

2.3 Sample Design

The dimensions of samples for three point bend tests must be optimized for the testing conditions. Using the specifications of the x-ray beam at the Advanced Photon Source, the ASTM standard for three point bend testing, and simulations conducted in the commercial FEM solver, Abaqus, the three point bend sample can be designed to fit the needs of the intermediate strain rate experiment.

2.3.1 Sample Sizing

Since these intermediate rate experiments were conducted in parallel with Kolsky bar experiments on the same specimens, it was important to keep sample geometry the same between both experiments to show rate dependent behavior. Because the 3-point bend Kolsky bar specimen has a support spacing, L = 8mm, the beams were cut to 10mm in length. The sample thickness in the x-ray propagation direction was chosen by using past experimental results at the Advanced Photon Source on 5mm thick quartz in conjunction with the NIST Xcom Photon Cross-sections Database [19]. For example, using the chemical constituents, their mass fractions, the x-ray accelerating voltage, and the density of the material as inputs, the attenuation coefficient was found to be 3.28 cm^{-1}. Using Lambert's Law with this attenuation coefficient, and the image signal to

noise ratio of the 5mm sample experimental results, it was decided that the maximum thickness of the samples would be 2mm to achieve acceptable signal to noise ratio. Because the samples were single crystal quartz, and a square specimen profile was desired, the other dimension was always chosen to be 0.1mm longer to identify crystal orientation while preserving a relatively square cross-section.

2.3.2 Sample Notch Size

The notch size was dictated using guidelines from ASTM for 3 point bend fracture toughness testing [14]. Guidelines indicate that notches lengths are governed be sample height and should be $0.12 \leq \frac{c}{d} \leq 0.3$. Thus, for 2mm tall beams, the maximum-targeted notch length was 600 μm. Actually achieving these target notch lengths using diamond wire machining proved difficult and time consuming.

Using the commercial FEM software Abaqus, a dynamic, explicit, plane strain analysis with tetrahedral elements was also performed on different sample geometries to determine sensitivity to aspect ratio $\left(\frac{L}{d}\right)$ and notch size. The results are shown in Figure 2, and indicate that for the same loading conditions, notch-tip stress at a given time after impact is largely independent of aspect ratio. Stress increases slightly (~10%) for

shorter notches of $\frac{c}{d} = 0.25$ versus long notches of $\frac{c}{d} = 0.375$ so machining errors in maintaining identical notch lengths could have a measurable affect on the failure time of the beam.

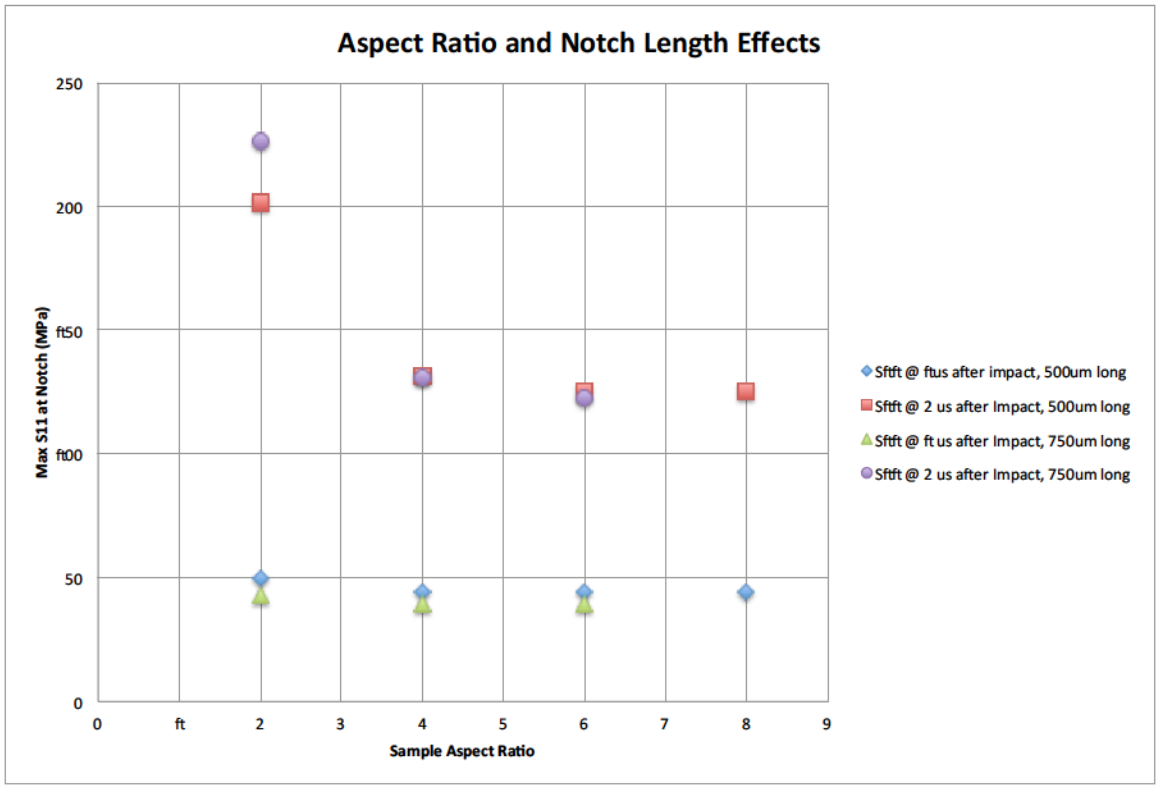

Figure 2- Summary of Abaqus results from simulations ran on a variety of sample aspect ratios and notch lengths

2.3.3 Notch Machining

There are many techniques that could be used to generate a notch in three point bend specimens. ASTM standards recommend the use of a fatigue pre-crack method or a complex "Chevron" notch geometry [14].

However, these methods were found to be too time consuming for our testing schedule so a modified commercial diamond wire saw was used.

2.3.3.1 Diamond Wire Technique

To machine the 120 μm wide notches in the samples, a diamond wire technique was used. The diamond wire apparatus used was a Well Diamond Wire Saw Model 3241. Originally, the cut speed was adjusted by changing the angle of a ramp. The saw rolled down the ramp due to gravity, so for faster cuts, higher ramp angles were required. This was found to produce very low cutting forces. Thus, the saw stage was fixed, and an independent x-y stage was added to translate the specimen into the wire. The wire tension developed by translating the specimen into the wire was much higher than the stock configuration, and could be controlled much more precisely with the micrometer used to advance the stage. For a typical cut into single crystal quartz, the stage was advanced till the wire contacted the specimen. At this point the stage was then advanced further (forward advance distance) into the wire to develop wire tension, and initiate the cut. These forward advance distances were typically 1.5 times the desired notch length for single crystal quartz.

2.4 Actuator Selection

The central part to any mechanical testing system is the means of actuation used to fracture the specimen. As outlined in section 1.2, a variety of techniques can be used to induce strain in a sample depending on the strain rate. However, for intermediate strain rates, many of the traditional quasi-static devices such as servo-hydraulics are not fast enough, and do not have the temporal repeatability for synchrotron triggering. Thus, finding actuators capable of both high velocities and low temporal jitter is a key challenge. This section outlines the procedure used to select the actuator for the intermediate strain rate testing of geological materials.

Piezoelectric actuators can achieve extremely high levels of temporal repeatability relative to other classes of actuators (i.e. voice coils, pneumatics, electromagnetic solenoids, or linear electric motors) [20]. Linear electric motors and pneumatics can go to millisecond time scales without distortion of the input signal, but for μs time scales, the displacement of the actuator will begin lagging the input signal for most applications [20]. This leaves voice coils and solenoids to compete at μs time scales. Most audio speakers consist of voice coils because of their distortion free performance for frequencies in the human hearing range (up to 20 kHz for healthy ears). However, voice coils and solenoids cannot

typically apply large forces (>20 N) without substantial, expensive amplification equipment [20]. Thus, piezoelectric actuators are the most compact, accurate, and repeatable actuator class to use for this application.

2.4.1 Piezoelectric Actuators

Certain types of crystals, called piezoelectric crystals, have a coupling between an applied electric field and lattice strain. These strains are often very small (< 0.1%), so the displacement across a bulk crystal is also very small (hundreds of nm) [21]. However, these crystals can be stacked in series, and when triggered simultaneously, can produce net displacements on the order of tens of microns. Then, these stacks can then be packaged inside of a flexible, mountable metallic case to form a viable actuator for a variety of precision applications. Depending on the application, this metallic case can be constructed to structurally amplify the displacement of the actuator further, but at the cost of actuation velocity [22]. Thus, for high velocity (>100 mm/s) applications, a stacked, unamplified actuator is used. If large displacements are more necessary than high velocities, then amplified actuators can be used. These tradeoffs are more clearly illustrated through the primary characteristics of a piezoelectric actuator: blocking force and maximum displacement.

Actuators are specified chiefly by their blocking force and free stroke (maximum displacement) at a certain maximum applied voltage. Blocking force is the force an actuator can apply to a fixed support without displacing at all. At maximum displacement, no further force can be applied so at the free stroke, there is no applied force, and at zero displacement, maximum force is applied. Both these are linearly related for a given applied voltage. This concept is best illustrated in Figure 3 below by comparing examples of amplified and stacked actuator operation spaces with different system responses. Thus, for a particular application, there likely exists an optimal actuator choice, especially when resonant frequency and response time are taken into account.

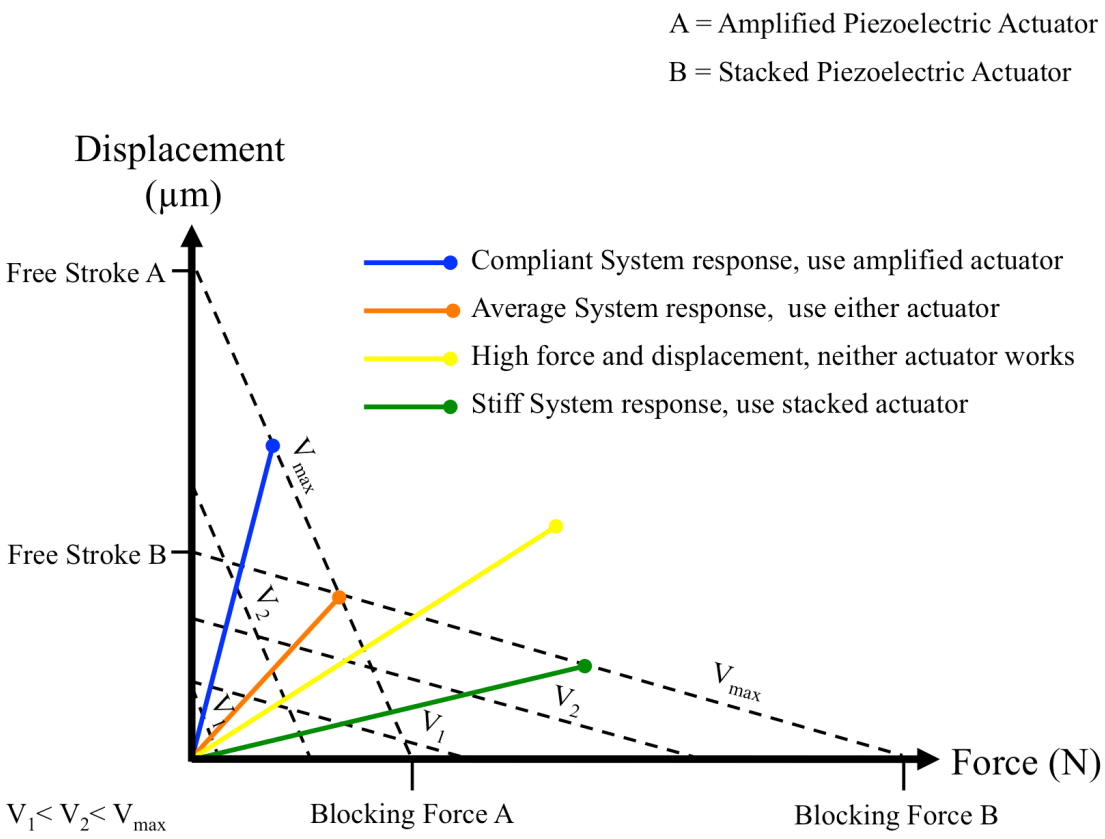

Figure 3- An example design space for two types of piezoelectric actuators

In addition to blocking force and free stroke, there are other specifications needed to characterize an actuators performance, especially when driven at high accelerations. As shown in Figure 4 (illustration of signals), the actual displacement history of an actuator may vary drastically from the desired displacement history applied to the actuator through a signal generator. In this example figure, a trapezoidal step signal is sent to the actuator with some rise time (input rise time). The actuator takes some

time to begin moving (response time), and then overshoots the desired displacement by some amount (displacement overshoot). Choosing an actuator with a small capacitance can minimize these distortions. This concept can be shown in Equation 3. Thor Labs application engineers use the equation to estimate piezoelectric actuators response time given the actuator capacitance, peak to peak voltage, and maximum applied current [23].

$$t \approx C \frac{V_{pp}}{I_{max}} \tag{3}$$

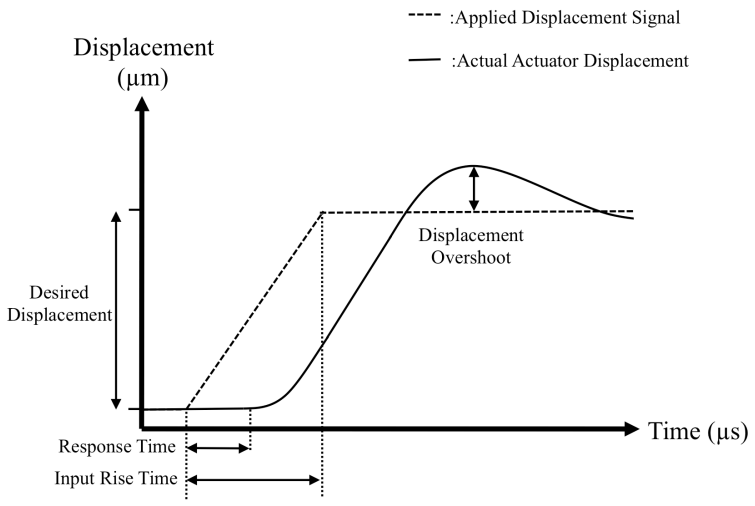

Figure 4- Illustration of the distortions caused by a theoretical mechanical actuator to the initial input signal. Units are included to give a sense of scale for typical piezoelectric actuator performance.

2.4.2 Anticipated System Load-Displacement Response

As indicated in section 2.4.1, the major design specifications for piezoelectric actuators are blocking force and free stroke. Once a line is drawn between these two points at maximum voltage, the operational space of the actuator is defined. It is critical to have an estimate of the displacements and/or forces required to cause specimen failure before an actuator is chosen. To estimate the compliance of the beam, the FEM software package Abaqus was used in similar fashion to section 2.3.2 to run a static, explicit, plane strain simulation with tetrahedral elements. The geometry used was for a 1mm tall beam with a plane strain thickness of 1mm, a length of 10mm, and a span of 8mm. The notch is 120 μm wide, and the displacement field is shown in Figure 5, with the samples load displacement response shown in Figure 6. In both Figures 5 and 6, the displacement tracked is the displacement of the node on the top surface in the exact middle of the beam.

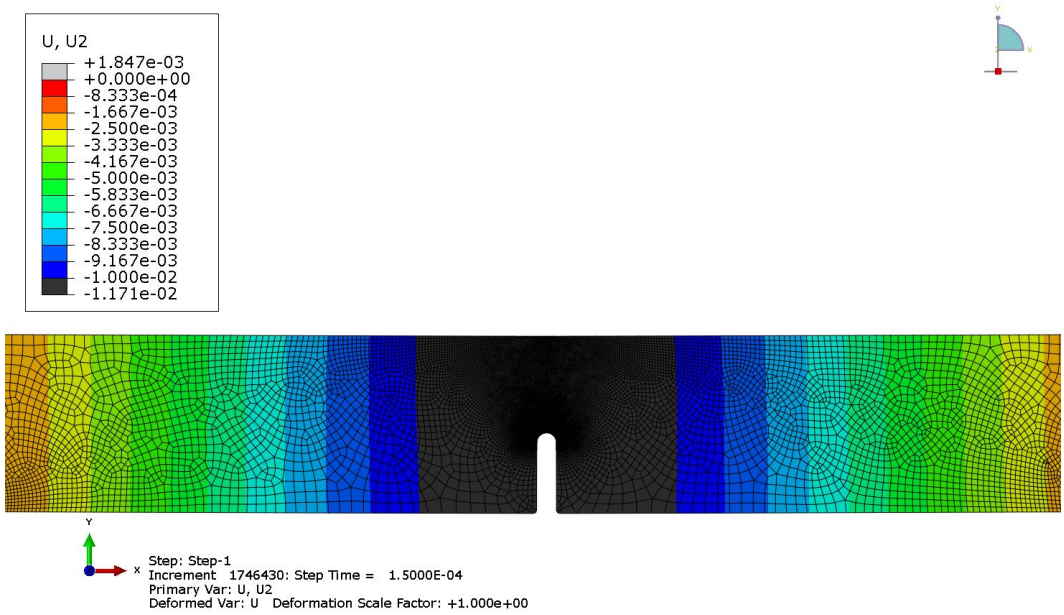

Figure 5- Displacement field in the vertical direction for the example single crystal quartz sample used for actuator selection. Units for U2 are mm. Note that the entire width of the beam is not captured in the field of view shown.

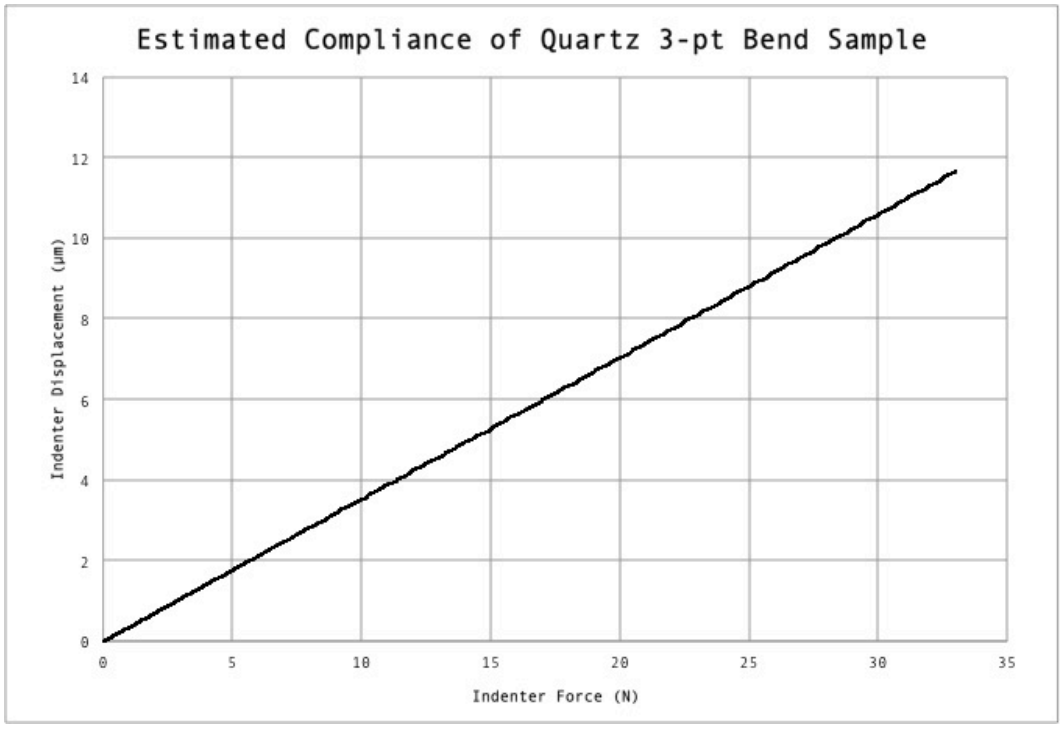

Figure 6- Load vs. Displacement response for the single crystal quartz notched beam shown above.

Based on the results shown in Figure 5 and 6, the actuators design space can be safely reduced to displacements of less than 20 μm. Because of the additional requirement that the actuator accelerate quickly to high velocities (~1 m/s), the low displacement requirement is a welcome one. It should be kept in mind that the results of Figure 5 and 6 only apply to the relatively stiff single crystal quartz system, so a different actuator choice will have to be made for softer systems with a higher displacement to failure.

2.4.3 Requirements for Rapid Actuation

Another primary requirement for an intermediate rate loading system is an actuator that can reach very high velocities, and thus develop high strain rates in the specimen. In fact, for this particular application, the requirement to reach high velocities with high repeatability ends up having the highest weight in final actuator selection due to the low resonant frequency of most actuators. The main requirements for high velocity actuators are high power supply slew rate, high peak voltage, high peak current, low actuator capacitance and high actuator resonant frequency.

To meet the high slew rate requirement, the high voltage requirement and the high peak current requirement, the PD200 built by PiezoDrive© was chosen. It can supply peak currents of 10 A, peak voltages of 200 V, and

slew rates of 150 V/μs. Thus, in theory, it can accommodate rise times of 1 μs for a 150 V actuator.

2.4.4 Final Actuator Selection

The actuator was chosen based on the several specifications outlined above. Because the test specimens are brittle, the displacement till failure is small, and the force required for failure may be high. This means a high blocking force; low free stroke actuator can be selected. Furthermore, a low capacitance, high resonant frequency actuator should also be chosen for high peak actuation velocity. To meet these requirements, a Cedrat Technologies© PPA20M was purchased. It has a free stroke of 20 μm at 150 V and a resonant frequency of 33 kHz. Also, the PPA20M utilizes a stiff metallic outer frame to pre-stress the piezoelectric material stack. This allows the actuator tip to accelerate and decelerate at very high rates without fracturing the piezoelectric material stack through high tensile stresses. These specifications enable the actuator to achieve response times quoted by the manufacturer to be 10 μs.

2.5 Fixture Design

There are several parts that had to be manufactured to build the PAIRLS, but a few in particular, required special attention to reduce overall load path compliance. The outer frame had to be designed to withstand the high blocking forces possible from the PPA20M actuator without significant compliance. Also, the translation stage had to be selected to balance the benefits of accuracy in displacement control and low compliance under load. Figure 7 shows the final design with parts labeled.

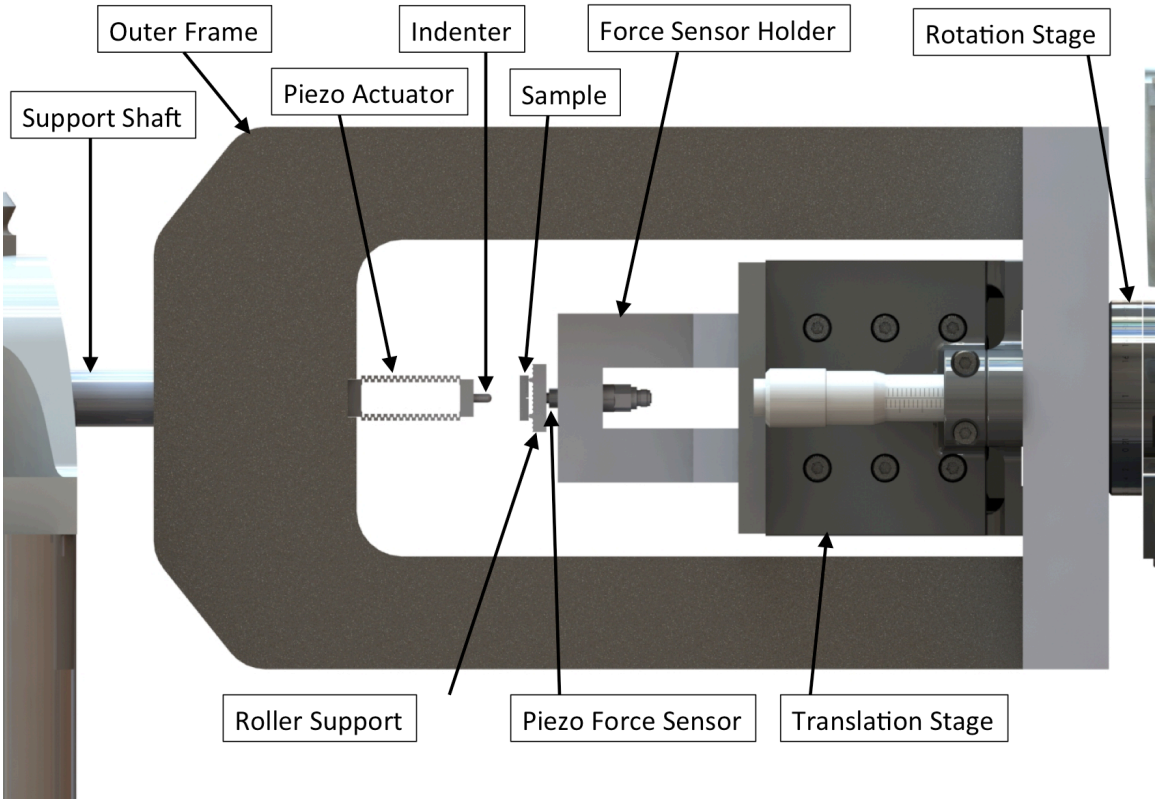

Figure 7- The final design of the PAIRLS (Piezo Actuated Intermediate Rate Loading System) with components labeled.

2.5.1 Outer Frame

The last major design consideration is the overall system compliance. Because the displacements of interest are on the micron or even sub-micron scale, an extremely stiff structure must be built to restrict the total compliance to the lowest value possible. Most quasi-static loading platforms have compliances on the order of 10 microns/kN. Our system was designed to a stricter stiffness standard to accommodate the small displacements and high forces of the piezoelectric actuator. FEM analysis using the commercial software package Abaqus was performed in order to get the displacement of the frame below 1 μm at 700N, the peak load of the actuator. The analysis was done using a static, explicit computational framework with linear elastic, isotropic material behavior. Material properties used for mild steel were $E = 200\ GPa$ and $\nu = 0.3$. The plot of vertical displacement contours is shown in Figure 8, and indicates a maximum displacement of 0.902 μm at the actuator mounting location for the maximum applied design load of 700 N.

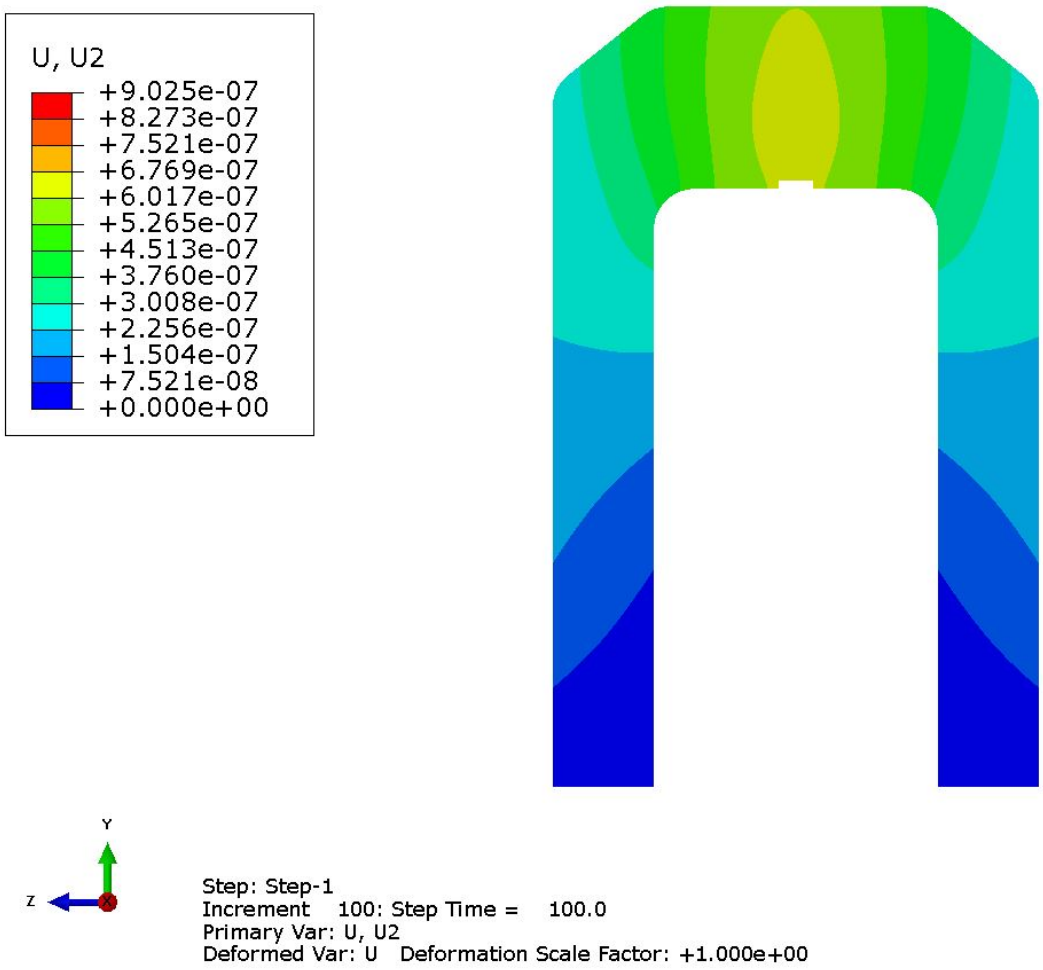

Figure 8- Displacement contours in the vertical direction for the outer frame when subjected to a 700 N static load at the actuator mounting location. Units for U2 are mm.

2.5.2 Translation Stage Selection

A primary compromise that had to be made was in the compliance of the movable support platform. Because the support platform must have the accuracy to displace by microns, it cannot handle high loads without significant displacement. Manufacturers do not typically quote translation stage compliances in the specifications. Instead, a maximum load is

quoted, so this, in addition to discussions with the application engineers can be used to guess at stage compliance. Lab jacks can handle high loads into the kN range, but backlash alone can be as much as 100 μm. Nano-positioning stages for optics cannot usually handle loads higher than mN, but can adjust position with accuracies of nanometers. Thus, a compromise was made, and a translation stage with 5 μm accuracy was chosen for its higher stiffness over the more delicate, more accurate stages.

3 Experimental Methods

A variety of specific experimental techniques were used to make the measurements required for intermediate strain rate experiments with micron scale displacements. First, a non-contact small displacement measurement technique was developed using state-of-the-art high-speed camera technology to measure the velocity of the actuator tip. Second, certain special considerations had to be made in the selection of the force sensor to allow for measurement of high frequency force signals that arise during intermediate strain rate experiments. Last, because calculating the strain rate for three point bend specimens is not possible using a full-field solution from elasticity, empirical or finite element solutions must be used. For the purposes of this work, a commercial FEM solver was used to estimate the strain rates experienced by the material at the notch tip just prior to fracture.

3.1 Displacement Measurement Procedure

Tracking of the actuator displacement and velocity during the experiment is critical to estimating the stress state of the specimen throughout the test. However, the non-contact measurement of displacements less than 10 μm with sampling rates of >100 kHz to accuracies of ~500 nm is a difficult task for most of the commercially available sensors. Because contact methods like LVDT sensors and

extensometers have inertia themselves, they do not accurately measure time dependent displacement changes over tens of microseconds. Laser interferometry can be used, but due to the additional cost of the optics, laser, and time required to manufacture diffraction gratings, the technique is not practical for this application. Thus, a robust method of displacement measurement utilizing the equipment already available in the laboratory was developed in-house.

The method uses a highly magnified Kirana high-speed optical camera capable of frame rates in excess of 5 Mfps. For lighting, a class 4 visible red laser was used for experiments in the JHU laboratories, and due to safety issues flash bulbs were used at the Advanced Photon Source (APS). The placement of the camera relative to the other experimental equipment for testing at JHU and APS are shown in the experimental schematics in section 3.4. The camera was zoomed into the metal frame just above the indenter location as shown in Figure 9.

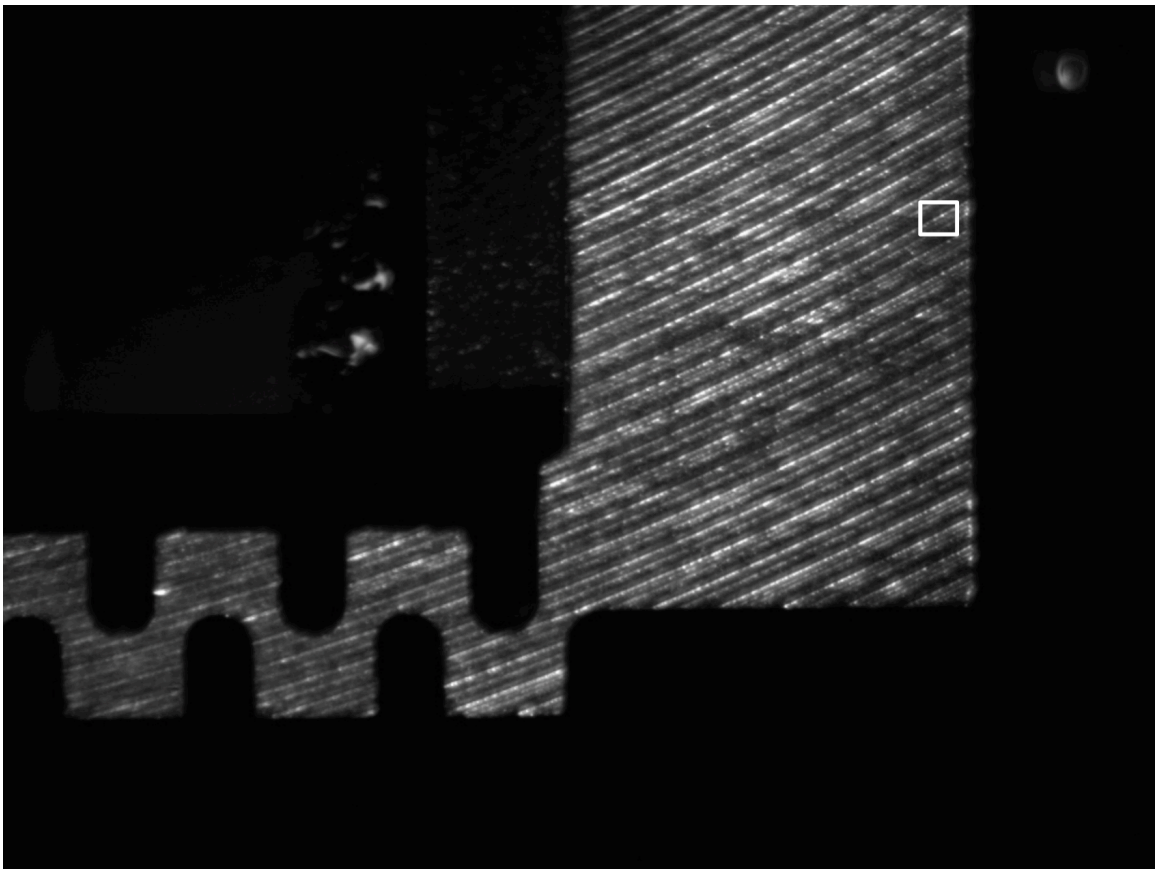

Figure 9- Picture of actuator taken using the Kirana camera using a 105 mm objective lens. The width of the view field is 10 mm. The 430 μm wide white square illustrates the field of view used for displacement measurement.

Because of the rigid nature of the metal used for the frame, the displacement of surface asperities on the end of the frame was assumed to match the displacement of the indenter. This was proved to be true in separate tests. Following imaging, the data was analyzed using a code written in MATLAB to track asperities in images. The procedure used to analyze the images is described in the numbered steps below.

1.) Crop raw camera Image (Figure 10) to isolate one moving asperity in a smaller image (Figure 11) amongst a neutral background.

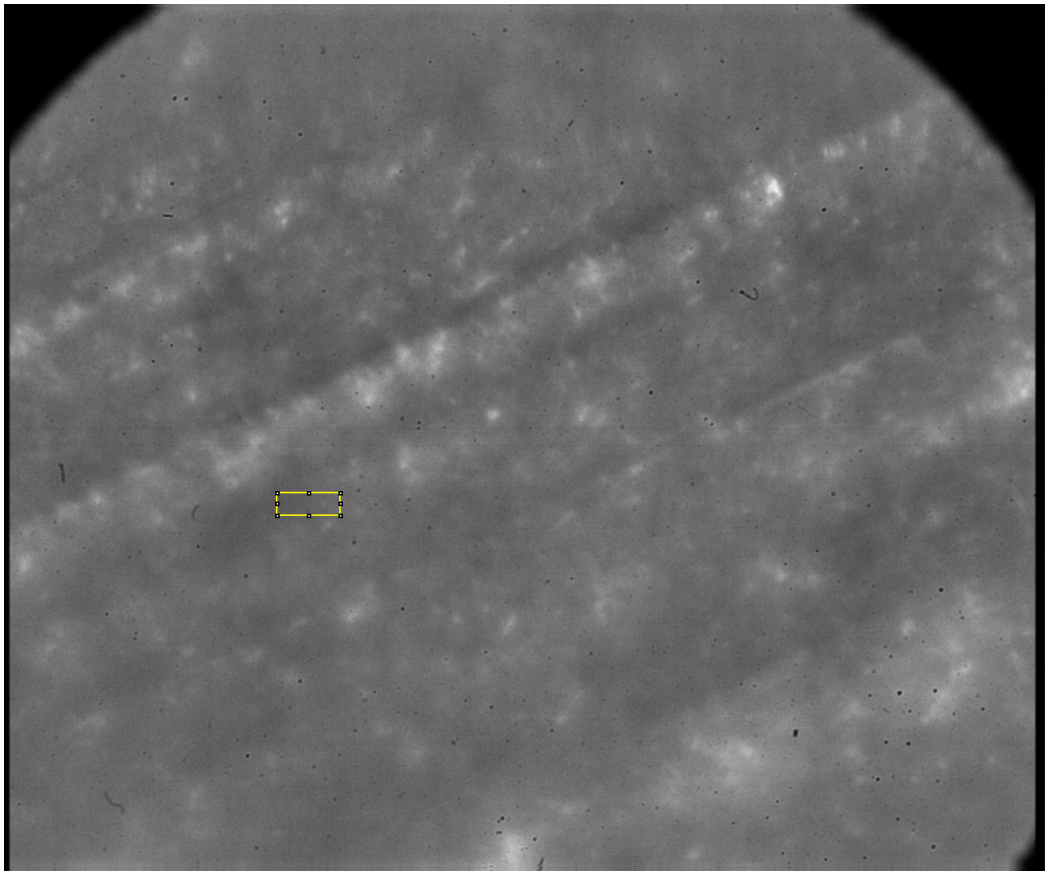

Figure 10- This is the cropped region shown in Figure 9. Image processing requires cropping image further (yellow box) to isolate a single asperity.

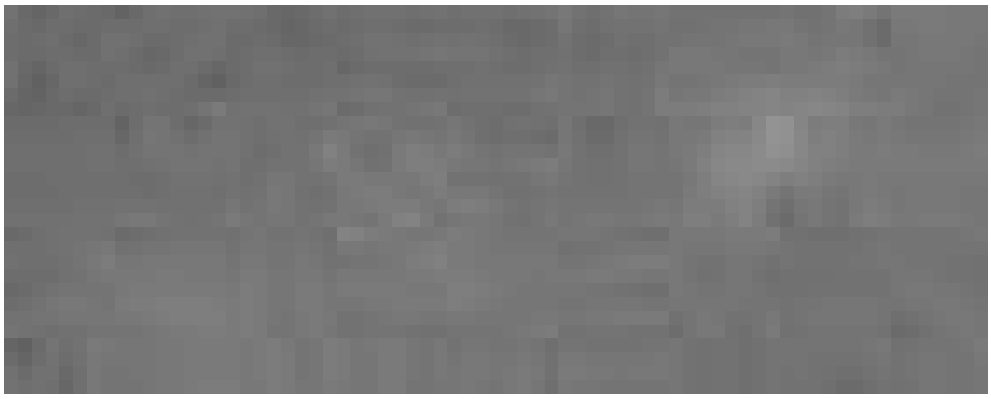

Figure 11- Cropped region from Figure 10 before normalization

2.) Normalize the cropped image (Figure 11) by rescaling all pixel intensity values to cover the entire range from 0% intensity to 100% intensity. This accounts for variations in brightness caused by the flash bulb warm-up and decay and exaggerates the asperity for more robust thresholding as shown in Figure 12:

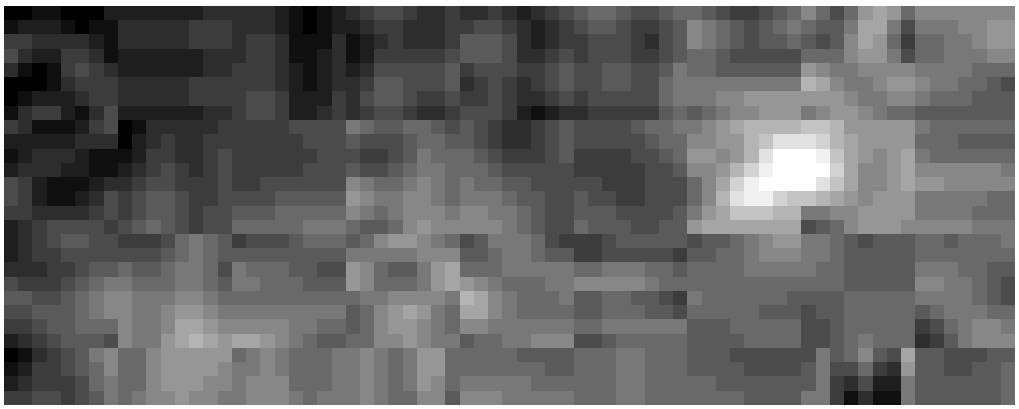

Figure 12- Image from Figure 10 after normalization

3.) Threshold the image to some brightness value i.e. 0.89 for this data set (this number varies data set to data set), and eliminate objects under 10 pixels in size (this number varies data set to data set).

4.) Track the centroid of the remaining objects in the x-direction, correlate the pixel width to the view field width, and use the frame timing to calculate actuator position as a function of time. A final image with centroid shown is in Figure 13.

Figure 13- Figure 12 after thresholding, small object elimination, and centroid identification.

3.2 Force Measurement

For experiments involving fast application of force, a force sensor must meet a few primary requirements. First, the resonant frequency of the sensor should be as high as possible so filtering of high frequency signals is minimized. Second, the force range should match what is expected in the experiment. A Kistler type 9215A force sensor was chosen to accommodate both of these requirements. It has a resonant frequency of 50 kHz and can measure up to 200 N. The force sensor was given a charge by a Kistler type 5018 charge amplifier. The internals of the sensor are shown in Figure 14. The force is applied by attaching a support platform for the roller supports using a small M2 threaded screw. The force is then transmitted through a softer material to the stiffer

sensing element to minimize stress concentrations on the surface of the sensing element.

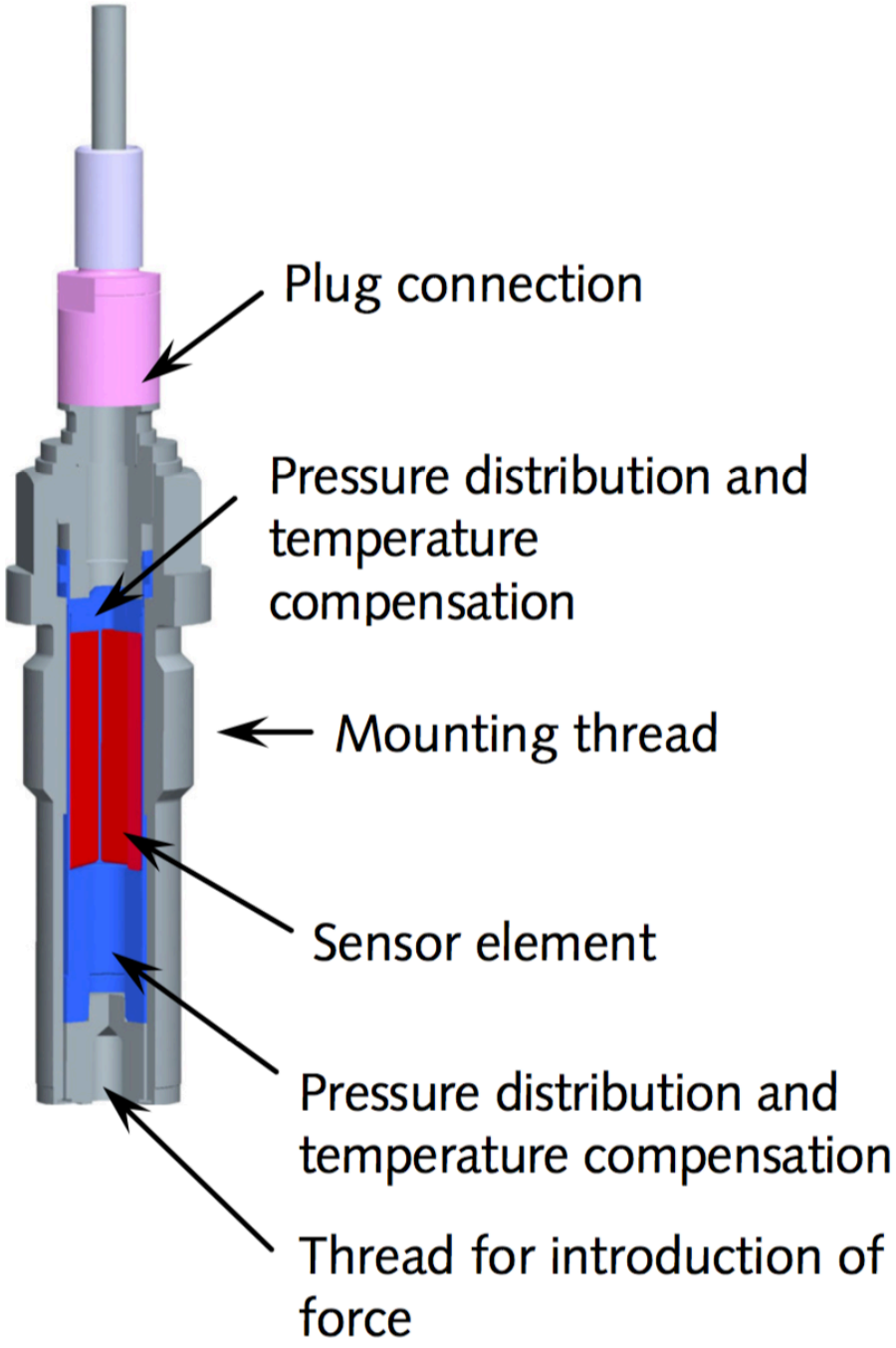

Figure 14- Schematic of the internal construction of the Kistler 9215a force sensor.

3.3 Strain Rate Estimation

For three point bend experiments, the strain rate field is not as homogenous as specimens under a uniaxial stress state so the strain rate cannot be easily defined using a full-field elasticity solution. To complicate matters further, the geological materials such as single crystal quartz have anisotropic elastic constants due to the crystallography of the trigonal 32 space group. Due to these complications, an area of interest must be chosen as a benchmark to define the strain rate at a point. For this experiment, the area of interest chosen is the notch tip because it is the nucleation site of fracture. Thus, linear elastic, dynamic explicit, plane strain simulations were employed to estimate the strain rate just before fracture. After the experimentally determined time of fracture nucleation, the simulation results are no longer valid because the simulation does not define fracture properties.

3.3.1 Input Geometry

The sample geometry was approximated using a 2-D plane strain approximation. Examples of geometries that were also experimentally tested are shown in Figures 15 and 16 with element boundaries. Dimensioned figures of each sample are provided in Figures 17-22.

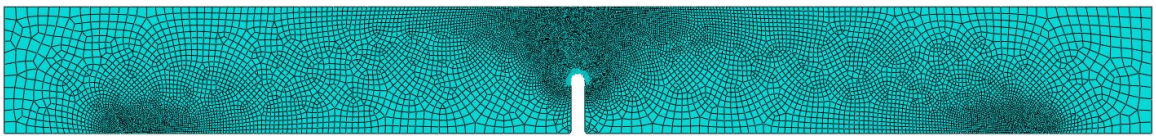

Figure 15- The geometry of sample SQX4_4 with refined mesh near the load bearing points, and a highly refined mesh near the notch. Total number of elements is 26,562.

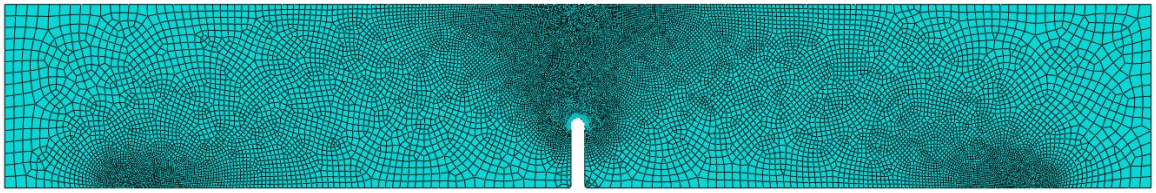

Figure 16- The geometry of sample SQX5_5 with identical seed size and bias as SQX4_4, but with 32,874 elements instead.

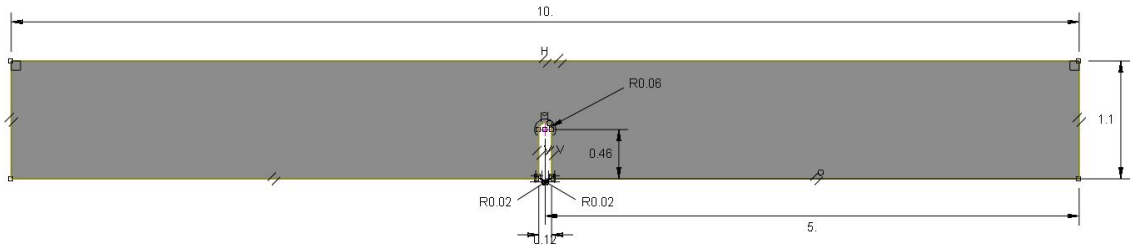

Figure 17- Dimensions for sample SQX4_3 in mm

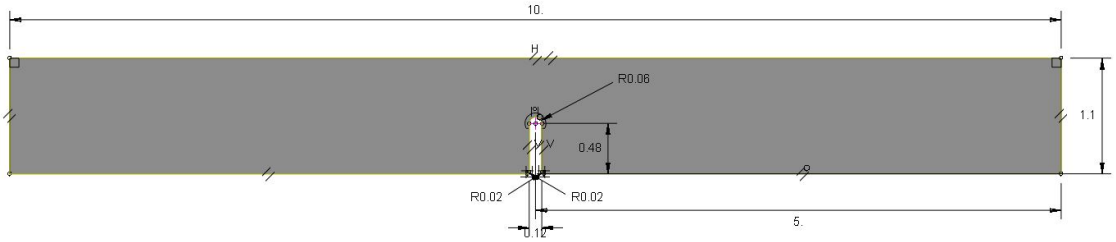

Figure 18- Dimensions for sample SQX4_4 in mm

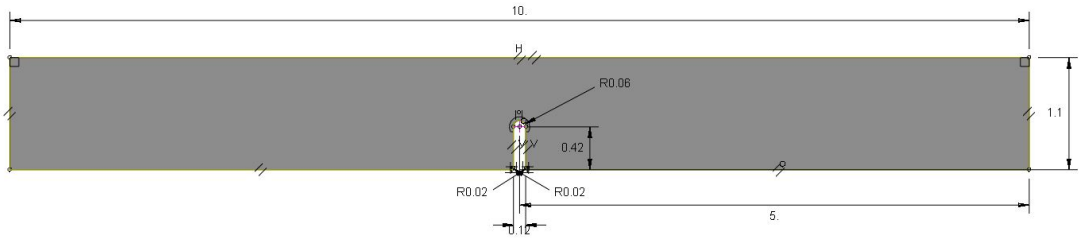

Figure 19- Dimensions for sample SQX4_7 in mm

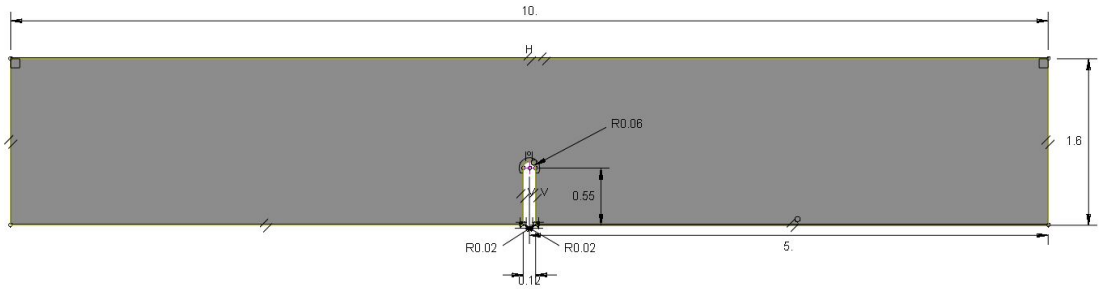

Figure 20- Dimensions for sample SQX5_5 in mm

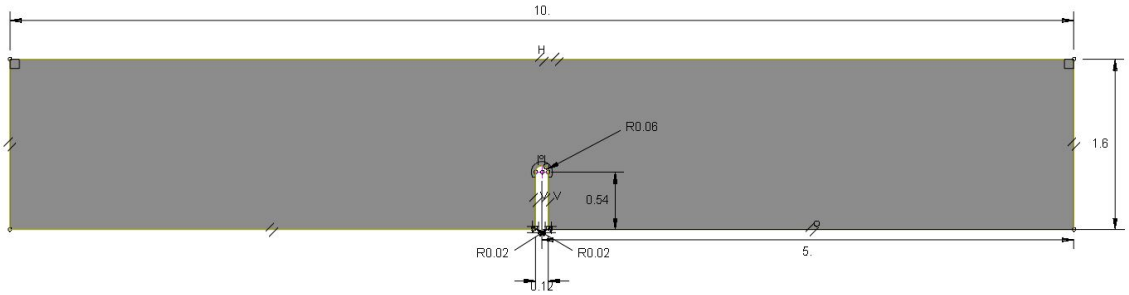

Figure 21- Dimensions for sample SQX5_6 in mm

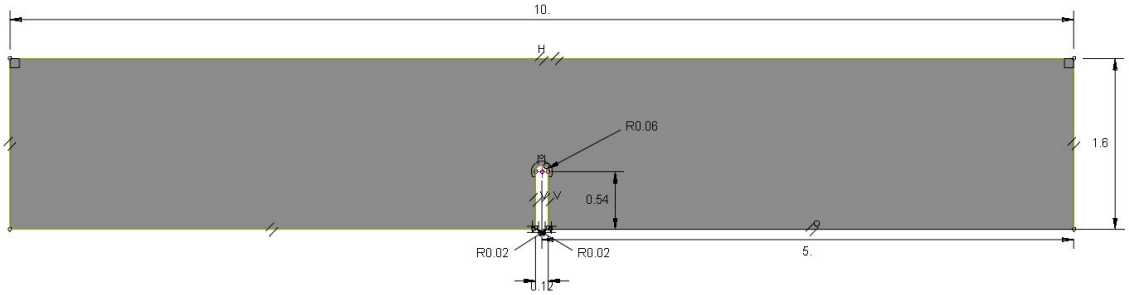

Figure 22- Dimensions for sample SQX5_7 in mm

3.3.2 Loads, Boundary Conditions, and Material Properties

The velocity history measured in the experiment was used as the $v(t)$ boundary condition as shown in Figure 23.

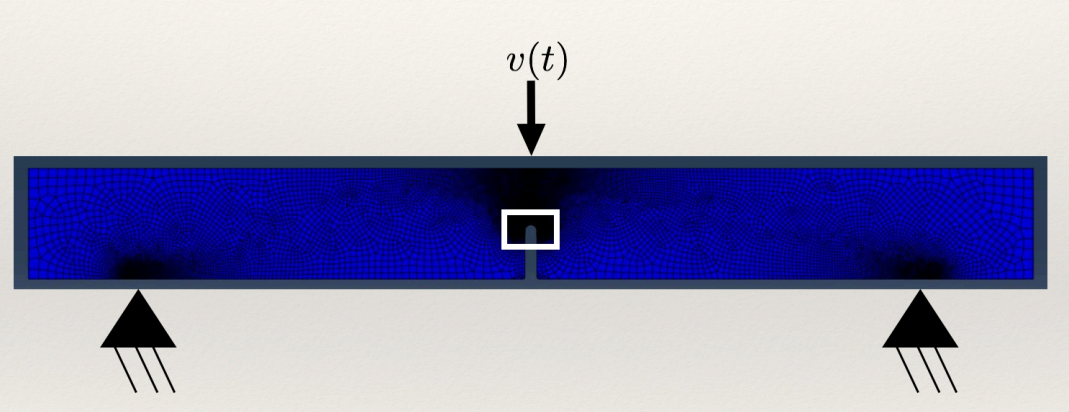

Figure 23- An illustration of the loading and boundary conditions used for the simulations. The white box surrounding the notch tip is the region shown in figure 24.

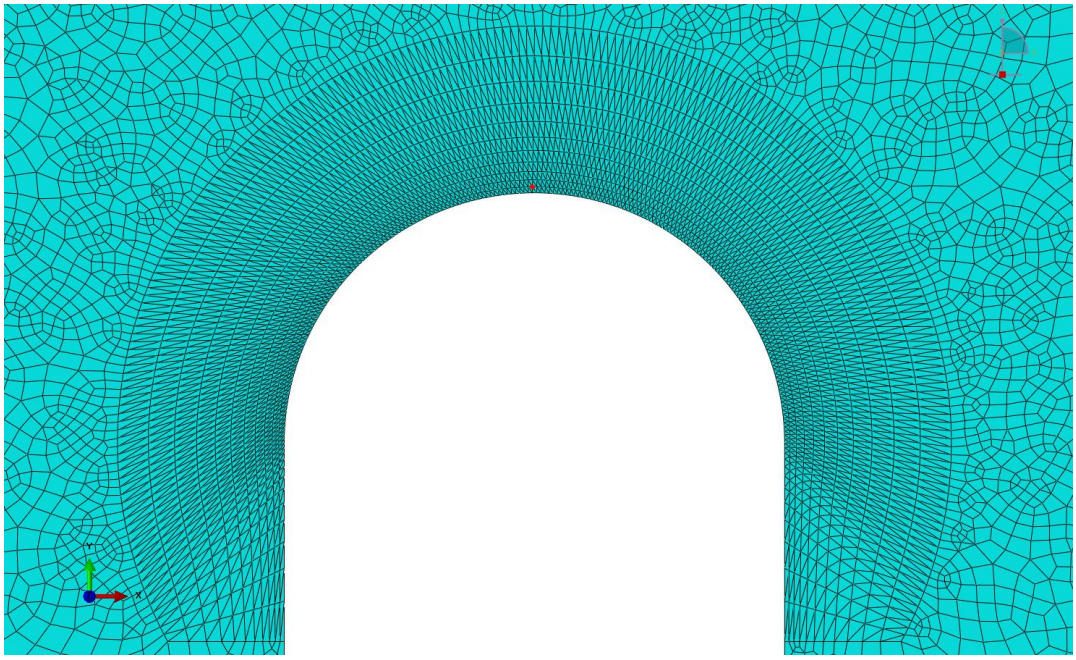

Figure 24- An example of the elements interrogated for the determination of strain rate. The element interrogated in this example is outlined faintly in red at apex of the notch, one row of elements into the sample.

Simulations were done using a mm, N, tonne unit system to better mesh the small dimensions. The density and the stiffness matrix used for the material properties are shown below.

$$\rho = 2.65\ x\ 10^{-9}\ \frac{tonne}{m^3}$$

$$D = \begin{matrix} 86740 & 6990 & 11910 & 17910 & 0 & 0 \\ 6990 & 86740 & 11910 & -17910 & 0 & 0 \\ 11910 & 11910 & 107200 & 0 & 0 & 0 \\ 17910 & -17910 & 0 & 57940 & 0 & 0 \\ 0 & 0 & 0 & 0 & 57940 & 17910 \\ 0 & 0 & 0 & 0 & 17910 & 39880 \end{matrix} MPa$$

The basis vectors used for this compliance matrix are the blue coordinate axes in Figures 25 and 26. The local element coordinates for material properties were rotated in Abaqus to match the actual orientation of the crystal while the global coordinates were kept as shown in the bottom left of Figure 24. The c/a ratio for alpha quartz at ambient pressures has been measured to be around 1.08, so this was the assumed c/a ratio of our alpha quartz samples. Boston Piezo Optics Inc. manufactured the samples, but made a mistake when cutting the SQX5 family of samples. This mistake was discovered

through the use of a Laue X-Ray Diffractometer. X-Ray direction was in line with the x-axis in Figure 24, and the $(11\bar{2}0)$ normal was found to correspond to the front face of the sample. Using a Wulff net, the fully defined orientation of the crystal was then found. As is shown in the SQX4 family, the positive rhombohedral plane, $(\bar{1}101)$, was to be parallel with the notch plane, but the manufacturer accidentally cut the SQX5 family of samples so the positive rhombohedron was rotated 90˚, and then tilted 6.78˚ as shown below in Figure 26. The positive rhombohedral plane was placed in the notch plane due to the findings of Tonge et. al. where fracture was found to propagate preferentially along this plane [24].

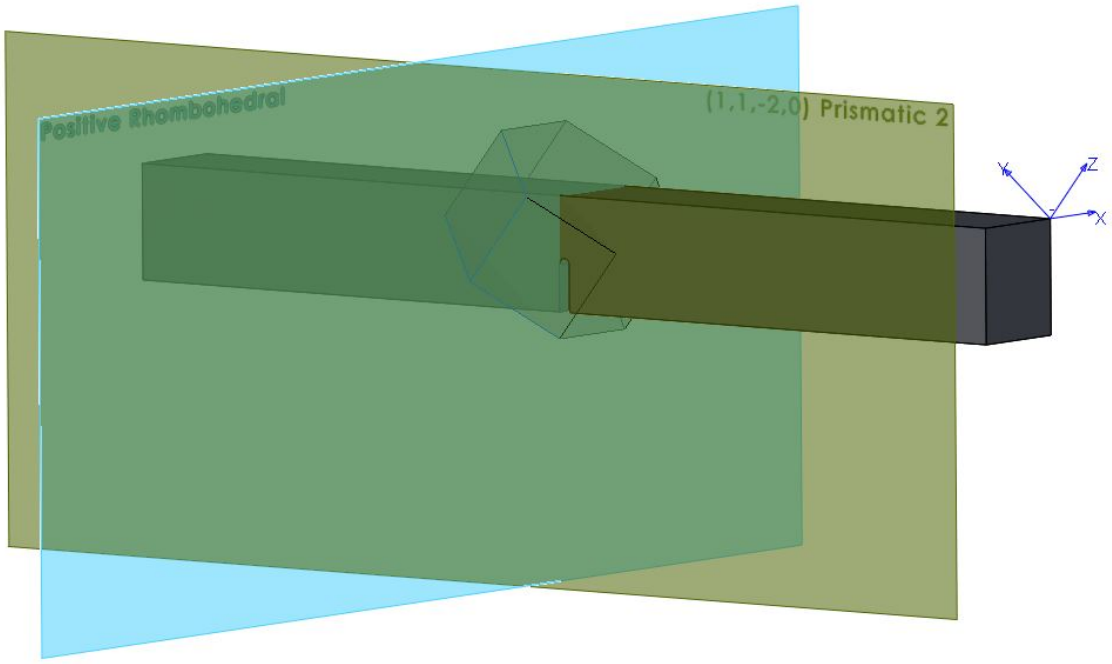

Figure 25- Crystal orientation relative to the SQX4 sample geometry. Coordinate axes shown correspond to the basis used for the compliance matrix. The prismatic plane is shown as the front face of the sample as determined via Laue Diffraction.

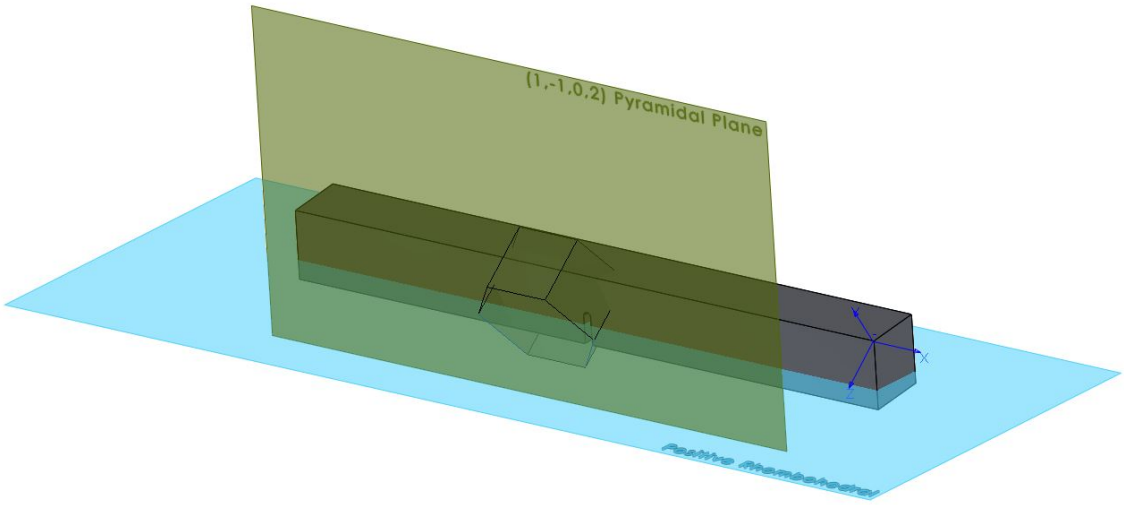

Figure 26- Crystal orientation relative to the SQX5 sample geometry. Coordinate axes shown correspond to the basis used for the compliance matrix. The pyramidal plane is shown on the front face of the sample as determined via Laue Diffraction.

3.3.3 Mesh Structuring

As shown in figures 15, 16, and 24, the mesh was refined near the points of support, the application of load, and the notch. Edges were seeded using bias towards the loading points to refine the mesh in those locations. The area in the vicinity of the notch was also refined. This was accomplished using a partition in Abaqus. Element sizes are refined smaller until convergence of the stress at the notch tip at a certain time is achieved. A mix of quadrilateral (hex) and tetrahedral elements were used to aid in meshing to completion. Once all edges, and partition borders were seeded, the automatic mesh generator was used.

3.4 Experimental Schematics

To better illustrate the experimental setup used at the two laboratories, JHU and APS, the experimental setup for each is shown in Figures 27 and 28, respectively.

3.4.1 Actuator Testing Schematic

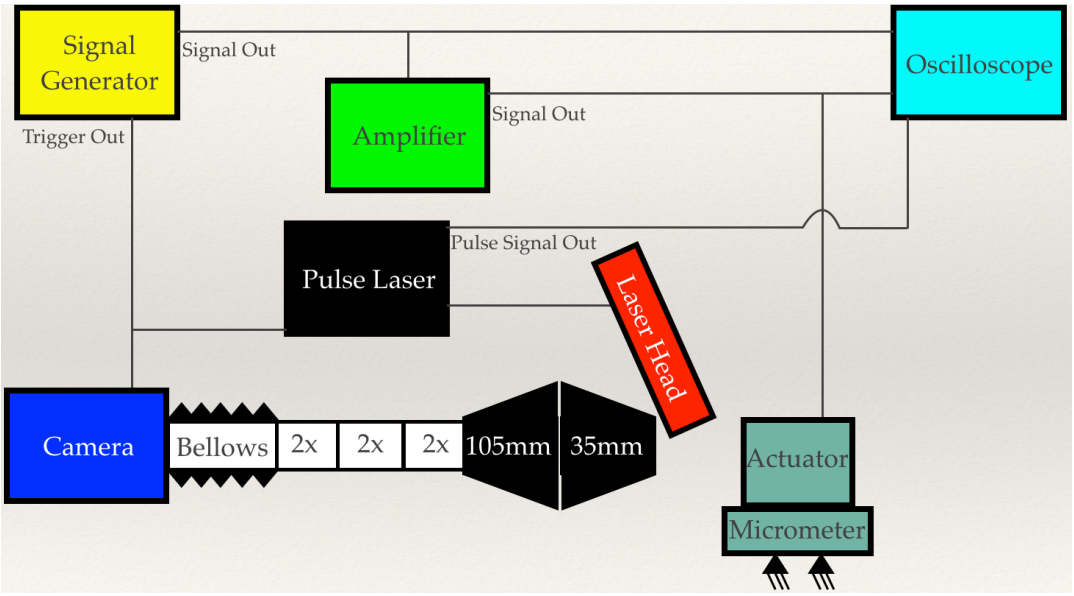

Figure 27- Experimental schematic for tests involving the characterization of the actuators performance

This experimental setup was used to acquire all of the preliminary data to characterize the performance of the actuator. The results of the actuator characterization are presented in section 4.1.1. Only test samples cut from glass microscope slides were used in this setup to practice the experimental technique prior to the APS trip.

3.4.2 Synchrotron Testing Schematic

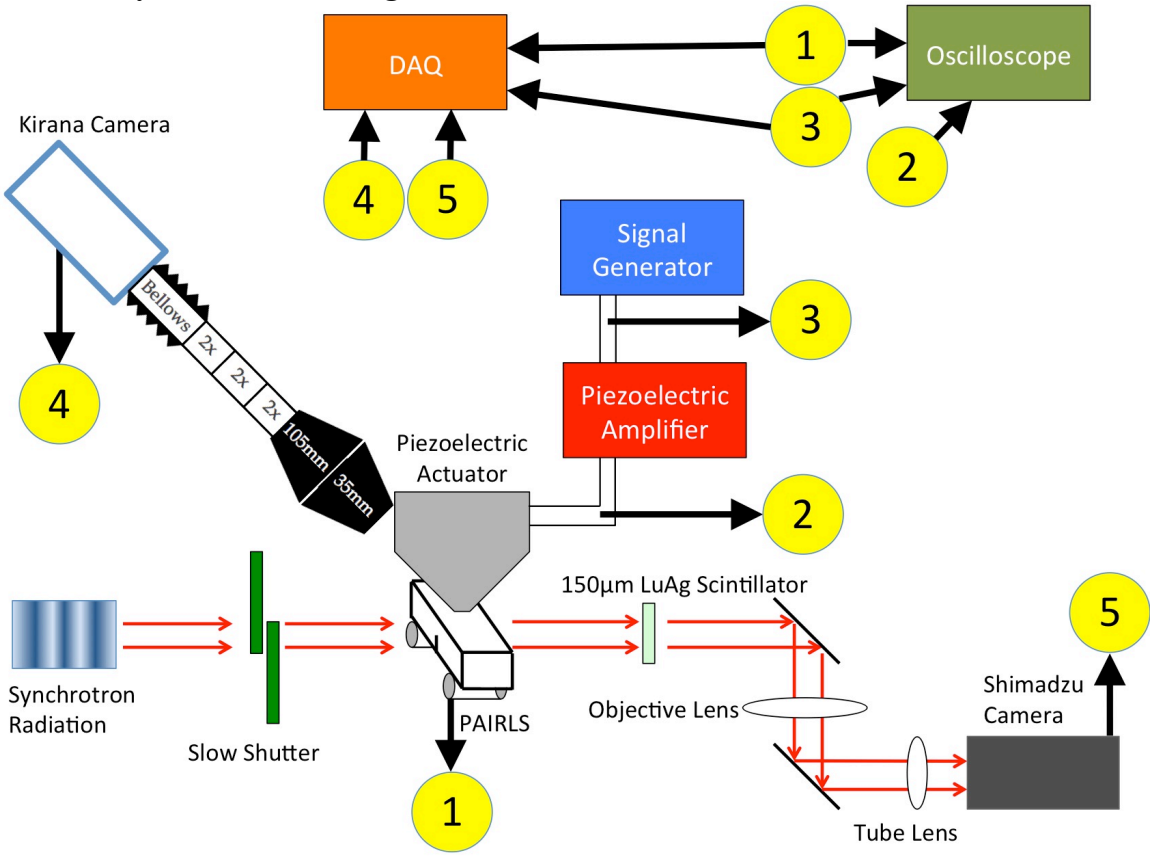

Figure 28- Final experimental schematic used for tests inside the synchrotron hutch. #1 indicates a force vs. time output. #2 indicates the voltage signal sent to the piezoelectric actuator. #3 indicates the voltage signal sent to the piezoelectric amplifier. #4 indicates the displacement measurement output from the Kirana photos. #5 indicates the phase contrast image data stream from the Shimadzu Camera.

The experimental setup used in the hutch is illustrated in Figure 28 with numbers indicating the key experimental measurements taken. Actual photos of the setup taken during testing are shown in Figure 29 with an inset picture showing a closer view of the PAIRLS.

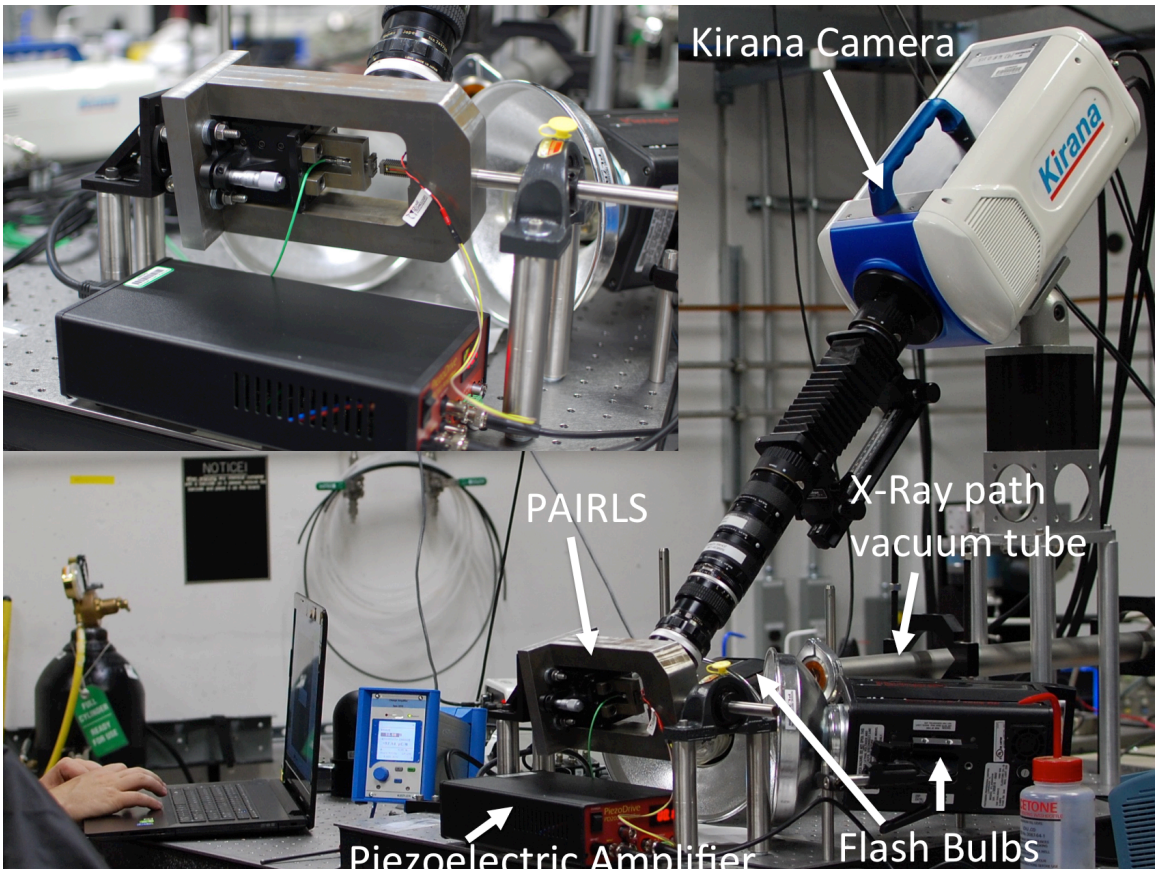

Figure 29- Photos of the experimental setup inside the hutch at APS. The camera is elevated significantly to prevent the long lens stack from interfering with the x-ray path.

3.5 Experimental Procedure

Several separate experimental procedures were used to acquire and interpret data from the PARILS. These are split up into procedures followed during the experiment (In-Hutch Procedure), and procedures used to interpret the data (Post-Processing Procedures).

3.5.1 In-Hutch Procedure

1. Open main beam shutter to expose undulator to radiation

2. Adjust undulator gap to achieve desired accelerating voltage

3. Trigger millisecond (slow) shutter to test for scintillator focus

4. Adjust focus of scintillator using copper mesh till entire view field has a uniform focus

5. Remove copper focusing mesh

6. Apply less than 1 mm^3 of grease to support rollers

7. Place support rollers in the support holder at the desired spacing (8 mm spacing was used for all experiments herein)

8. Place sample on the roller supports, and center in both x and z directions relative to the indenter using jigs built for the sample thickness

9. Check force sensor measurement and verify it is at zero, and a short decay time of τ =10s.

10. Advance translation stage until indenter makes contact with the sample. Contact is identified by a force jump in the force sensor signal.

11. For thin 1.1mm beams (SQX4), preload samples to between 1 N and 2 N. For larger 1.6mm beams (SQX5), preload beam to 4 N and 6 N. Record preload in lab notebook

12. Leave sample to rest for at least 2 minutes so the force signal can decay back to zero

13. Set oscilloscope to use a qualified trigger on a force drop of 1 N, but only after it has experienced a rise of 1.5 N prior to force drop.

14. Check all other triggers on the Kirana, flash bulbs, signal generator, and DAQ

15. Search and clear hutch

16. Trigger signal generator to start the experiment

17. Save all data from DAQ, Kirana, and Oscilloscope

18. Recover two halves of specimen and place back in sample bag

19. Search and exit hutch to re-check scintillator focus, and start back at step 1 for next sample

3.5.2 Post-Processing Procedures

The post-processing procedures are split into the major tasks which were needed to interpret the phase contrast imaging (PCI) data, and those which were needed to interpret the data from the DAQ and oscilloscope.

3.5.2.1 PCI Images

To account for the phase mismatch between the 153ns electron bunch spacing, and the 200ns (5 Mfps) inter-frame timing on the camera, the images must be post-processed to eliminate “blinking”. The images

were all measured for average brightness, and a distribution of brightness's was formed around an average brightness. Then, each image was corrected to the mean using the distance its original brightness was from the mean of the stack.

3.5.2.2 Alignment of Signals

The experiment was started using the TTL signal sent from the signal generator once the pulse signal was sent. Using a delay in the signal generator, the start of the pulse signal reaches the actuator 50 μs after the initial trigger. Because data was read into both the DAQ and the Oscilloscope (used for high voltage signals like the amplifier to actuator voltage), the initial signal generator TTL was read into both as a channel. Using this common experimental start landmark, all of the signals were aligned with each other.

3.5.2.3 Force Data

The force sensor voltages from the charge amplifier were first converted to forces using the sensitivity of the charge amplifier at the time of the experiment. For all of the 6 trials presented here, 5 N/V sensitivity was used. Then, the force signal was adjusted upwards by adding the preload that was recorded in step 11 of the in-hutch procedure.

4 Results and Discussion

The results are split into two sections, experimental results and computational results. The results are then interpreted in an analysis section, and discussed further in the discussion section.

4.1 Experimental Results

The testing of the PAIRLS was separated into two primary experimental environments. In the first, experimental results were collected to analyze the performance of the actuator. In the second, results were collected on samples of single crystal quartz with accompanying phase contrast data.

4.1.1 Actuator Characterization

The Cedrat Technologies PPA20M came from the manufacturer with a quality control test sheet outlining many parameters including its blocking force, free stroke, and resonant frequency. Although these measurements are comforting to the customer in that they prove the advertised specifications, they are not comprehensive enough for design purposes. Because we use Abaqus FEM software to estimate the strain rate, and we estimate the general stress state using a velocity boundary condition on the top of the beam, we need to measure the velocity of the

actuator to estimate the attainable strain rates before experiments on samples are conducted.

Using the experimental setup illustrated in Figure 27, an optical high-speed camera with laser illumination was used to film the free end of the actuator. The technique for measuring displacement is outlined in more detail in section 3.1.

Portions of the results from the actuator characterization testing are shown in Figures 30 and 31. Visual displacement refers to the displacements measured by tracking centroids of objects using the high-speed camera. Amplified signal voltage is the signal measured going into the piezoelectric actuator (data stream #2 in Figure 27). Input signal voltage is the signal measured going into the amplifier (data stream #3 in Figure 27). Input rise time is defined according to Figure 4. Trapezoidal signals are used because the simple shape of the input simplifies the process of quantifying and identifying distortion.

4.1.1.1 100 µs Input Rise Time

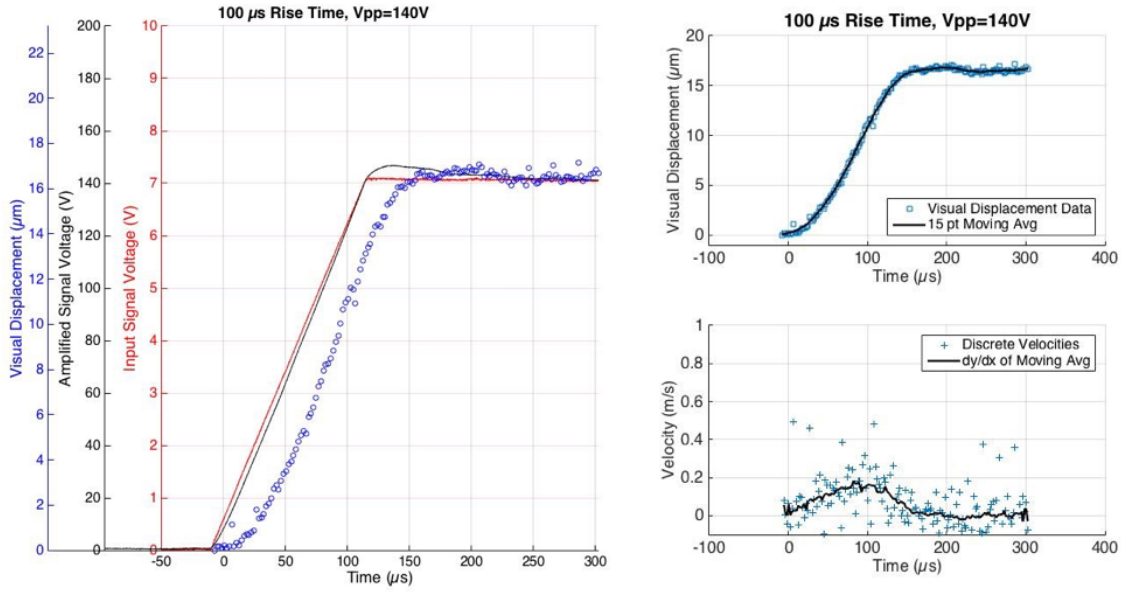

Figure 30- Actuator testing data for a 100 µs input rise time. Displacement tracked at 500,000 fps

4.1.1.2 20 µs Input Rise Time

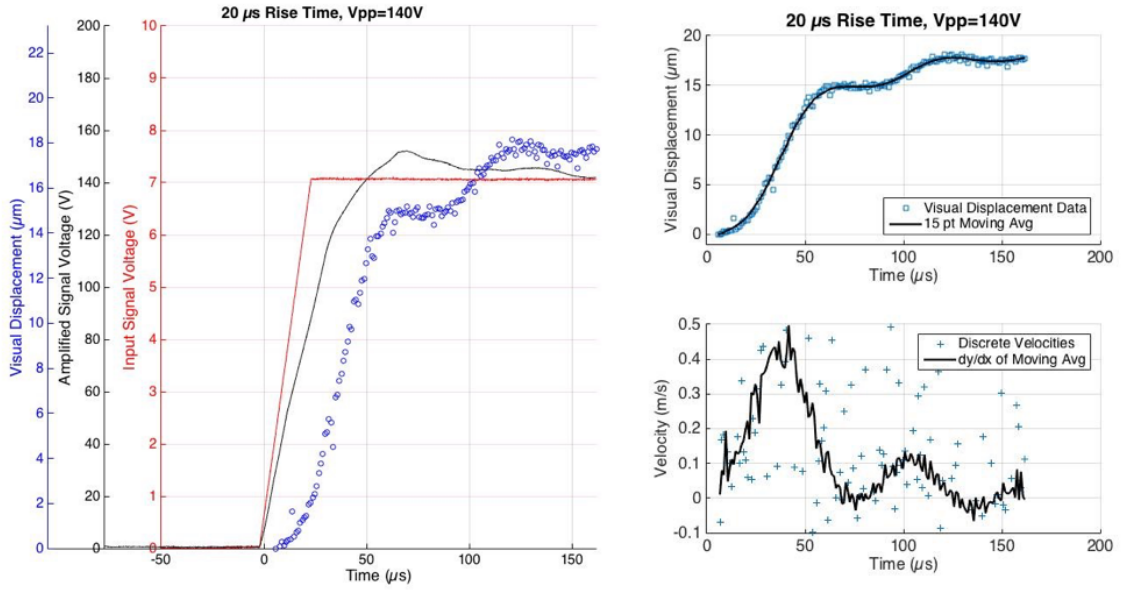

Figure 31- Actuator testing data for a 20 µs input rise time. Displacement tracked at 1,000,000 fps

Actuator testing results for input rise times of 10, 15, 40, 60, and 80 μs can be found in the appendix at 9.1.

By running these experiments, a multitude of key performance parameters not published by the manufacturer were measured. These include response time, minimum rise time, distortion of input signal, displacement overshoot, and time-dependent velocity histories. For instance in Figure 30, the maximum velocity reached by the actuator for a input rise time of 100 μs is approximately 0.2 m/s. Furthermore, the shape of the amplifier response can be seen to overshoot the input signal by 9 V. The amplifier overshoot of 9 V then can be tracked to an overshoot of about 0.5 μm in the actuator response. However, the distortions at 100 μs input rise times are insignificant to the distortions when the system is driven using 20 μs input rise times. For 20 μs, the amplified signal ramp slope does not match the input signal. At 120 V, the amplified signal ramp slope deteriorates further, and then overshoots by nearly 15 V. These distortions manifest themselves in the actuator response through a slight retraction by the actuator beginning at 50 μs, then a severe 2 μm overshoot at 125 μs. Thus, it seems that both the amplifier and the actuator are overdriven when 20 μs input rise time pulses are used so there

must exist a clear cutoff point which defines the safe operational range of the actuator, amplifier system.

Using the results from the appendix, the operational characteristics of the actuator under a variety of input rise times can be cataloged and used to inform the testing conditions at the synchrotron. For instance, it can be seen from Figure 53 that distortions from the amplifier start when using input rise times of 40μs and below. Overshoot in the amplifier signal is an issue at all input rise times, but its magnitude reduces as input rise times increase. Using the results from the actuator characterization, it was determined that 300 μs rise times would be used as an initial starting point for synchrotron testing due to the low distortion and overshoot observed.

4.1.2 Synchrotron Testing Results

The testing of samples in the synchrotron to prove functionality of the PAIRLS was limited severally by beam time. Accordingly, only 6 successful tests were conducted, and all were conducted at the low range of strain rates attainable by the PARILS. A summary of the sample testing conditions is given in Figure 32.

Sample	Length (mm)	Height (mm)	Depth (mm)	Notch Length (μm)	Input Rise Time (μs)	Peak X-Ray Energy (keV)	Preload (N)
SQX4_3	10	1.1	1	520	300	16.146	1.62
SQX4_4	10	1.1	1	540	300	15.902	1.42
SQX4_7	10	1.1	1	480	300	15.902	1.87
SQX5_5	10	1.6	1.5	610	300	16.146	5.95
SQX5_6	10	1.6	1.5	600	300	16.146	4.69
SQX5_7	10	1.6	1.5	600	300	16.146	4.88

Figure 32- Summary table of experimental parameters

To compress the body of this document, only the results of sample SQX4_4 are shown in this results section. Results from the other five samples are shown in the Appendix in section 7.2.

4.1.2.1 SQX4_4

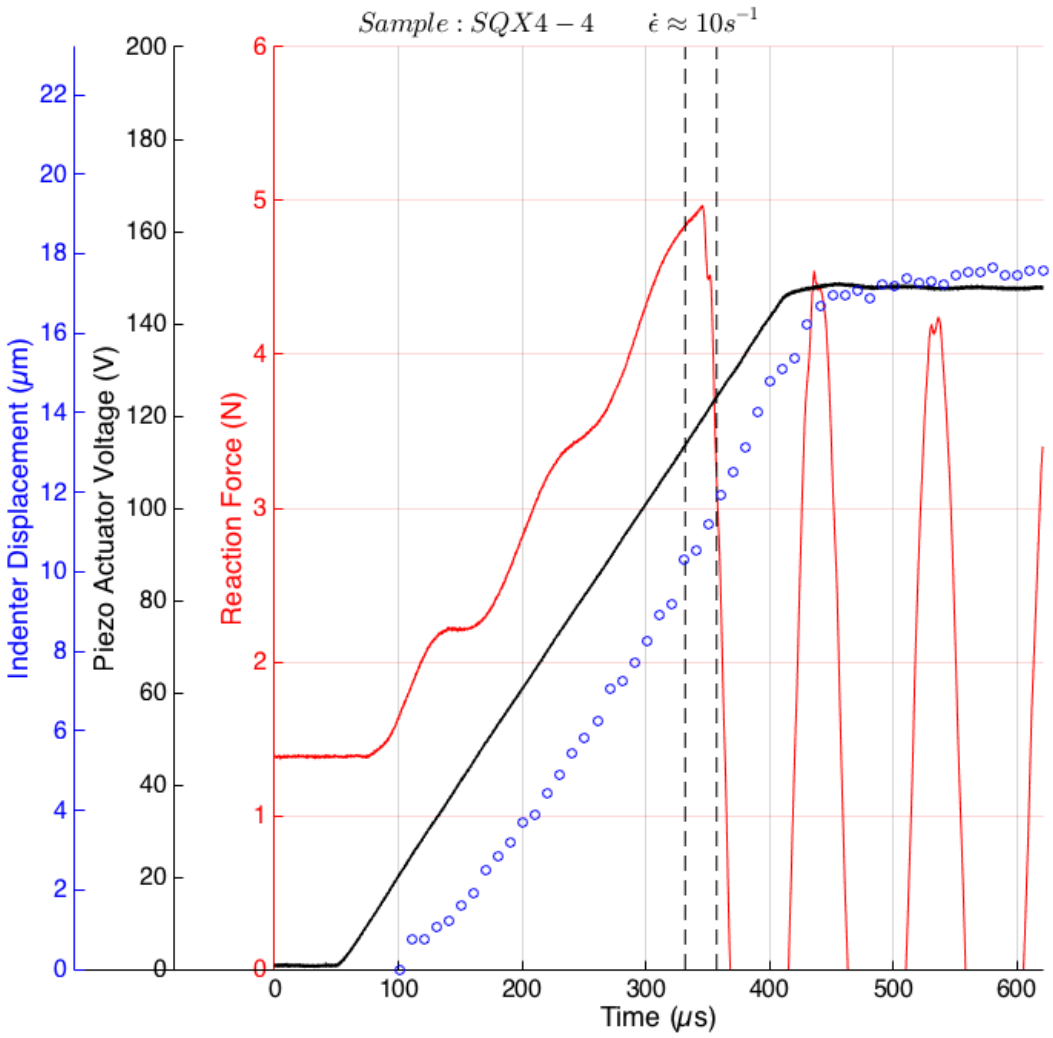

Figure 33- Actuator displacement was imaged at 100,000 fps. PCI images were taken at 15.902 keV. Sample preload was 1.42 N.

The results from SQX4_4 are qualitatively similar to the results of the other 5 samples. Each shows a very repeatable step pattern in the force signal on loading, and oscillations in the force signal after failure of the sample. These oscillations are discussed further in section 4.4.1.2.

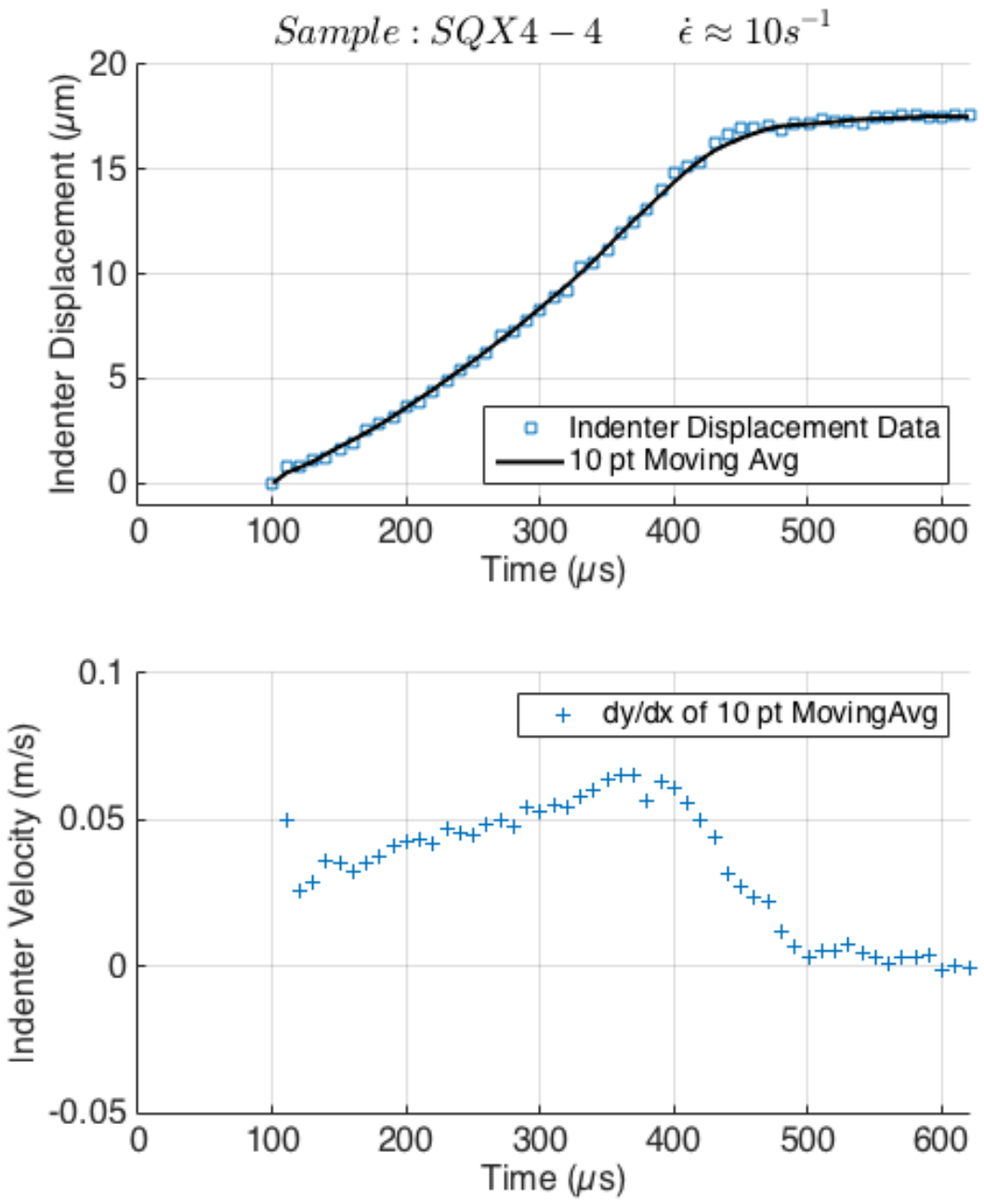

Figure 34- Top: Indenter displacement with a 10 pt moving average fit. Bottom: Indenter velocity generated from discrete derivatives of the 10 pt moving average fit.

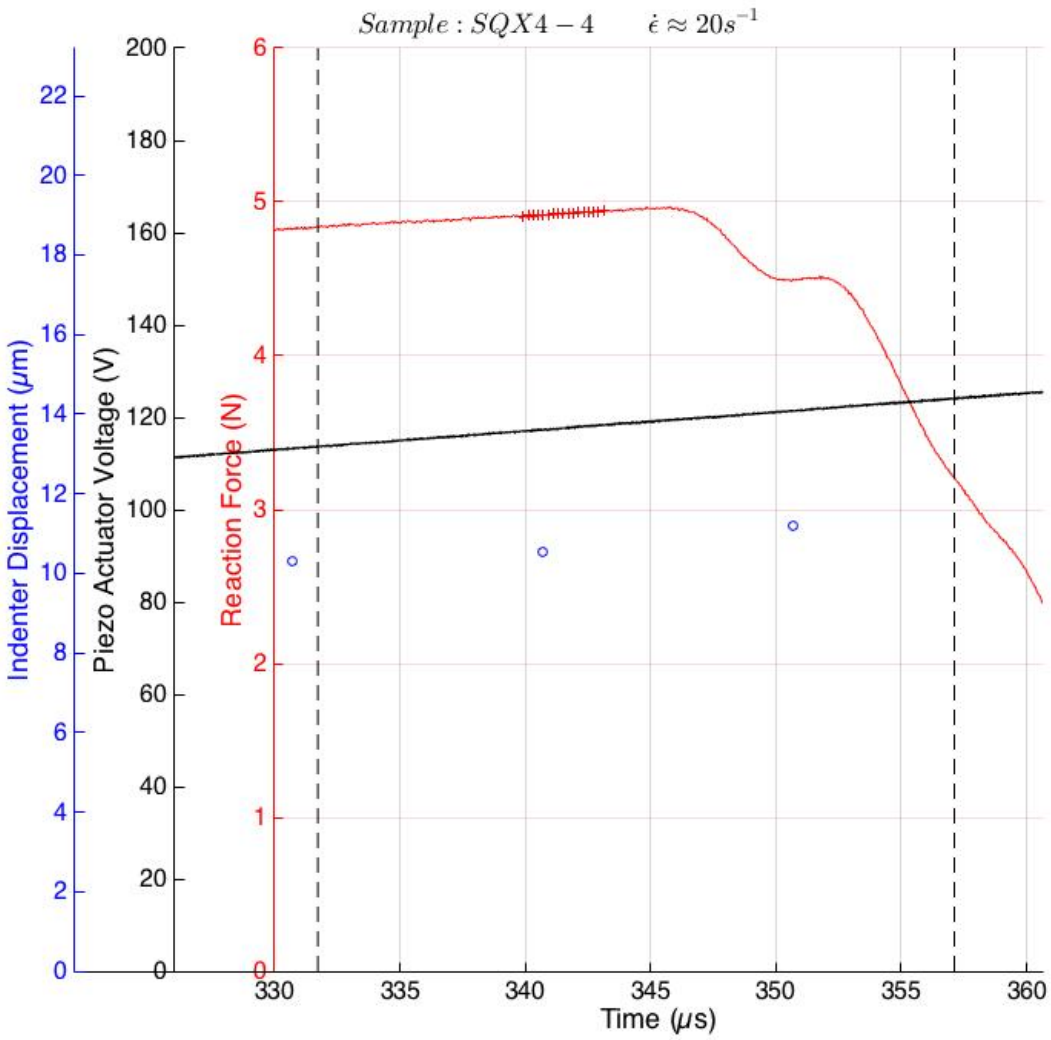

Figure 35- Vertical dotted lines indicate the beginning and end of the phase contrast imaging window. Small cluster of red markers on F(t) curve indicates the window from crack nucleation to complete fracture for t=[339.92, 343.12] μs

In the actuator performance data shown in Figure 34, the peak actuator velocity of 70 mm/s occurs 375 μs after the triggering event. In Figure 35, failure can be seen to occur at 346 μs, but the PCI images show the crack fully propagated across the sample at 343.52 μs (Figure 39). This ~3 μs delay indicates a certain level of delay in the force signal.

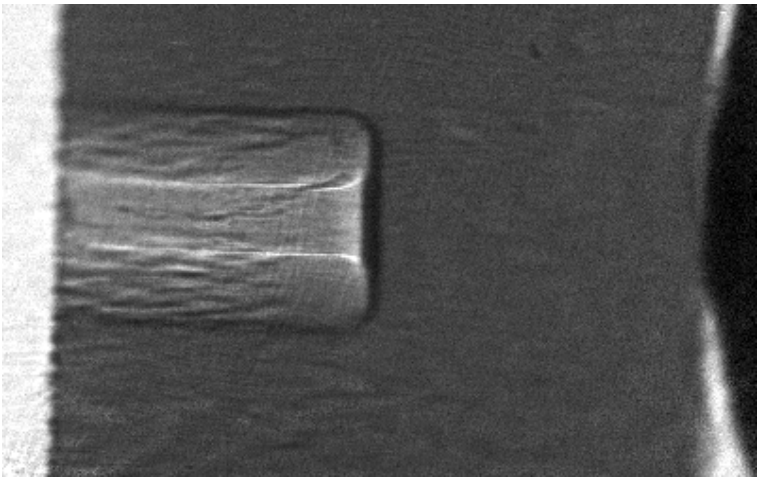

Figure 36- PCI image at t=339.92 μs. First evidence of crack nucleation

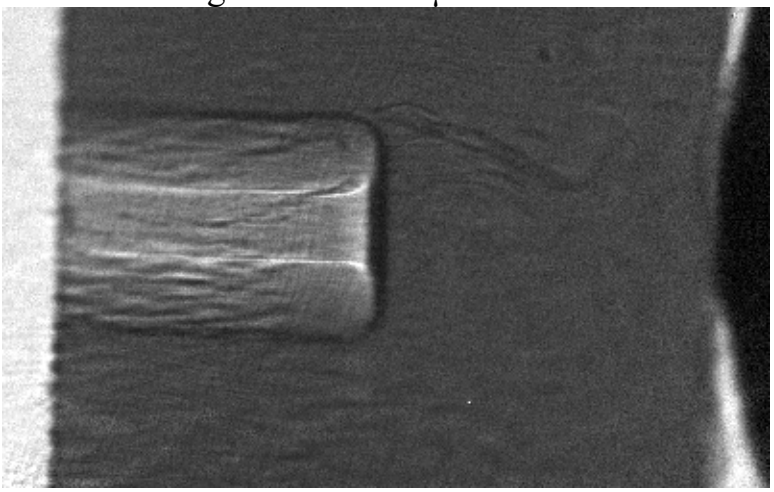

Figure 37- PCI Image at t=340.52 μs

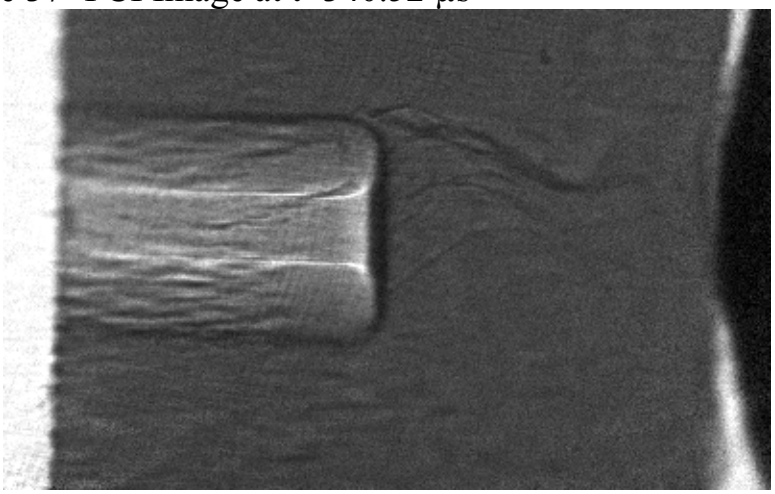

Figure 38- PCI Image at t=341.52 μs

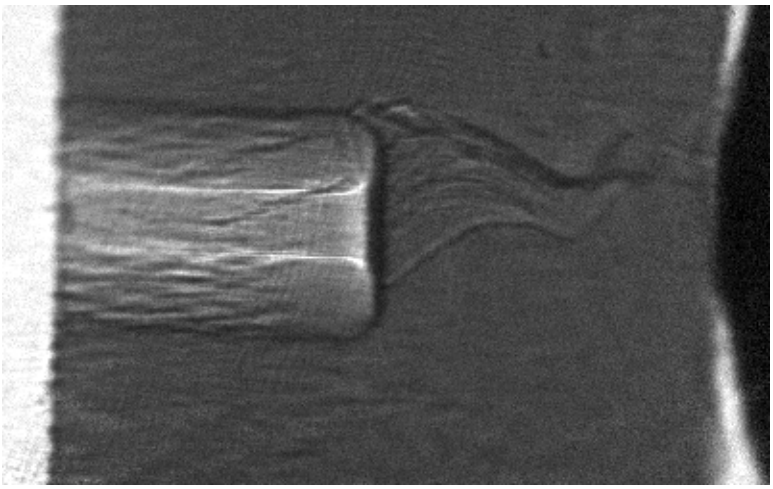

Figure 39- PCI Image at t= 343.52 µs. Crack appears to have propagated completely across the sample to the indenter

4.1.3 Summary of Experimental Results

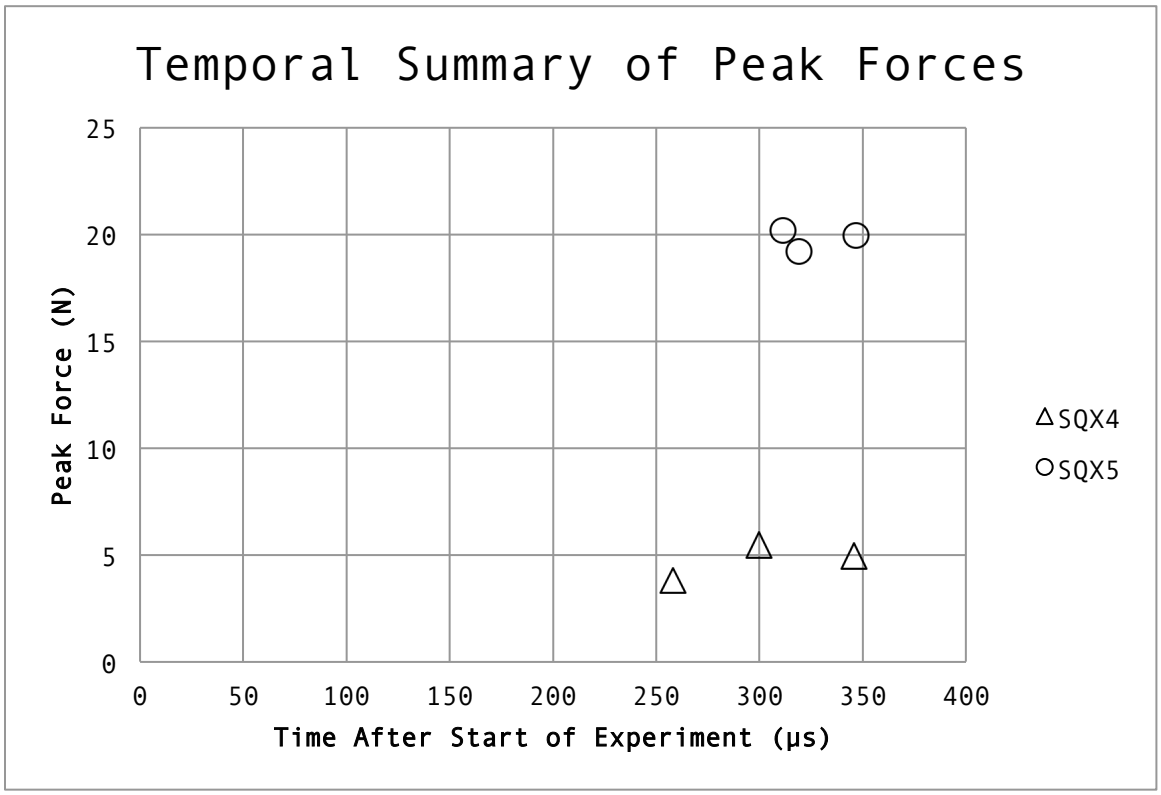

Figure 40- The timing of peak force transmitted through sample for each sample family. The results of the 5 other tests can be found in the appendix.

4.2 Computational Results

As described in section 3.3, to estimate the strain rate for three point bend specimens, it is necessary to use an empirical relation or perform a finite element simulation. For our purposes, finite element simulations were chosen. The results presented in the body are for SQX4_4, but the results for the remaining 5 samples can be found in section 7.3 in the appendix. First, a sample specific (SQX4_4) strain rate history is presented. Last, the estimated strain rates for a variety of input rise times are presented to allow for prediction of the strain rate based on experimental inputs.

4.2.1 SQX4_4

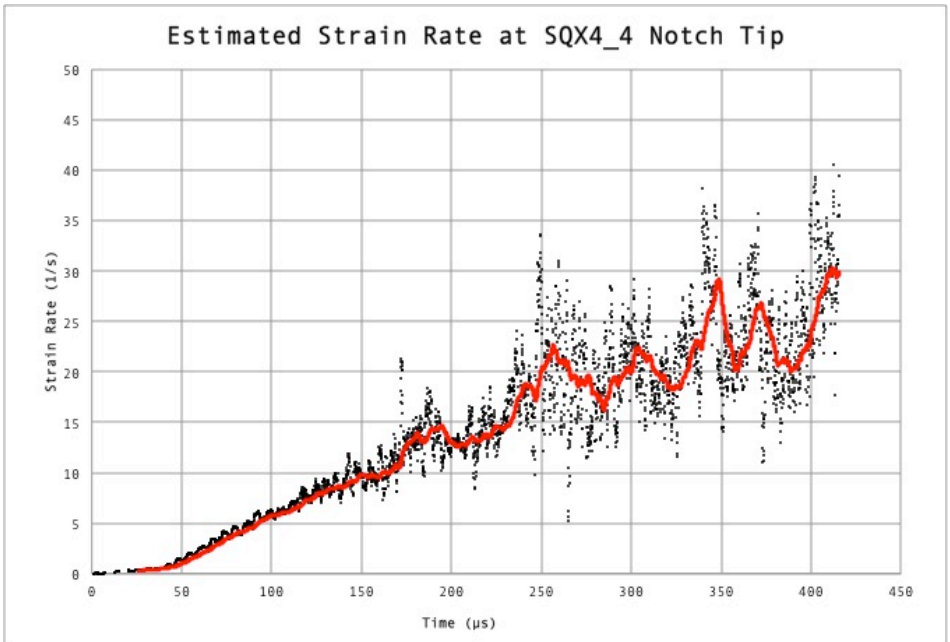

Figure 41- Strain rate history for the element at the apex of the notch tip.

Because of the high repeatability in the actuator velocity for SQX4 samples, the peak strain rates for SQX4_3 and SQX4_7 were found to be nearly identical to SQX4_4 despite the different notch lengths. Just prior to the time of failure, results indicate the strain rate at the notch in SQX4_4 to be between 20 and 25 s^{-1}. A range of strain rates is presented due to the high level of noise in the simulations. The noise is believed to be the result of internal wave reflection in the sample and structural harmonics of the beam oscillating. With the anisotropy of the sample, the internal wave reflections are not symmetric so although the boundary conditions are symmetric about the notch, the strain field will not be symmetric. Thus, the wave reflections will interfere with each other in non-intuitive ways. This is especially true because the timescale difference between the wave reflections (tens of nanoseconds) is vastly shorter than the simulation time; allowing for hundreds of interference events to occur.

4.2.2 Input Rise Time Testing

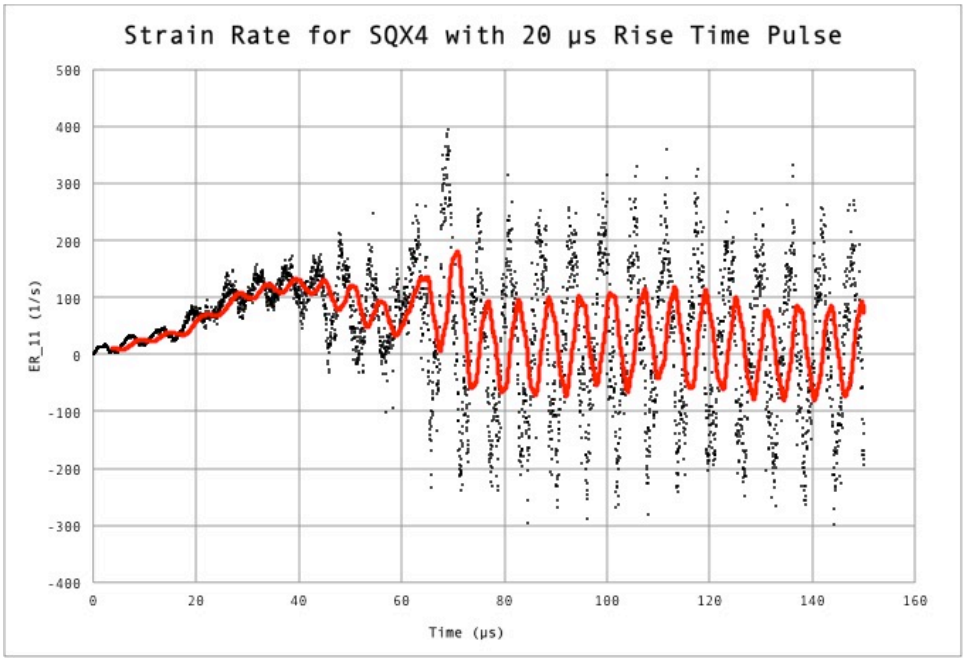

Figure 42- Red line is the 100-pt moving average of the raw discrete data. Peak strain rate is approximately 150 s^{-1} at roughly t=40 µs

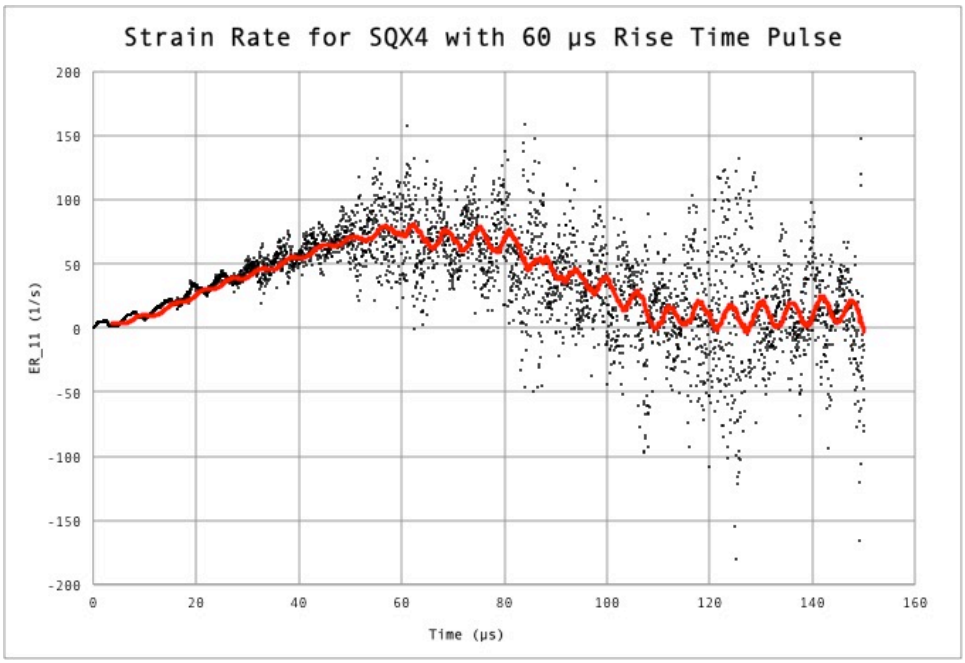

Figure 43- Red line is the 100-pt moving average of the raw discrete data. Peak strain rate is approximately 80 s^{-1} at roughly t=60 µs

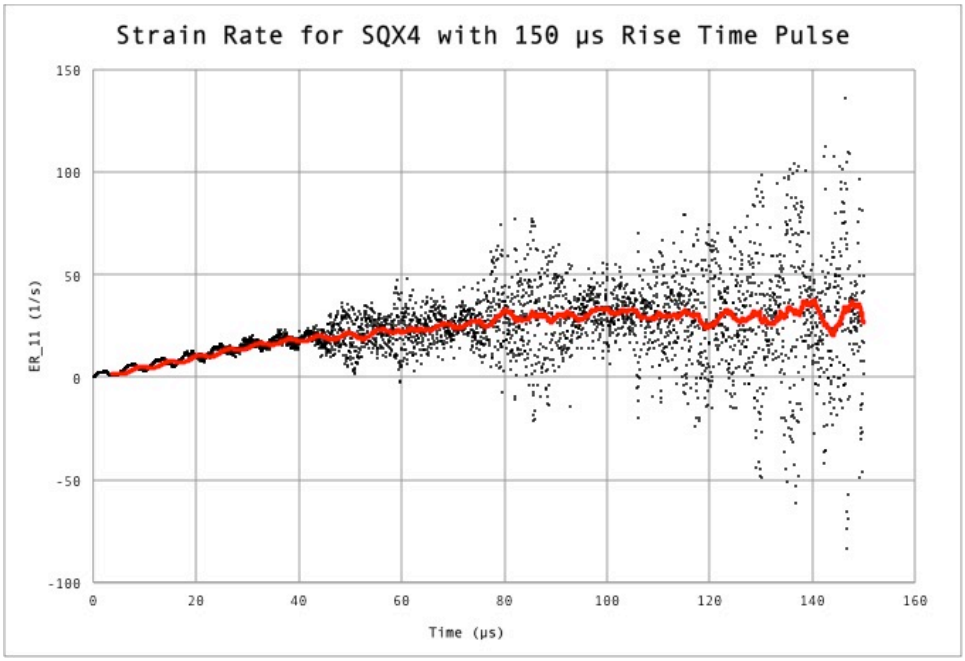

Figure 44- Red line is the 100-pt moving average of the raw discrete data. Peak strain rate is approximately 40 s^{-1} at roughly t=140 µs

Computational results for the estimated strain rate histories in samples SQX4_3, SQX4_7, and SQX5 samples can be found in the appendix at 9.3.1. Computational estimates of the strain rate histories in SQX5 samples were not distinguishable from each other due to noise, similarity in velocity boundary conditions, and similarity in notch size so they are presented as a single graph to represent the entire SQX5 sample family. Computational estimates of the strain rate history for the SQX5 family of samples can be found in the appendix at 9.3.2.

4.3 Analysis of Results

Analysis of the data was focused on to two areas where simple analysis of the data was possible. To allow for future users of the PAIRLS to predict the strain rate in their samples (assuming 10 mm long beams), a simple fitting procedure was conducted on the data from section 4.2.2. Then, crack speeds were measured for two locations along the same crack front.

4.3.1 Estimates of Strain Rate From Input Rise Time

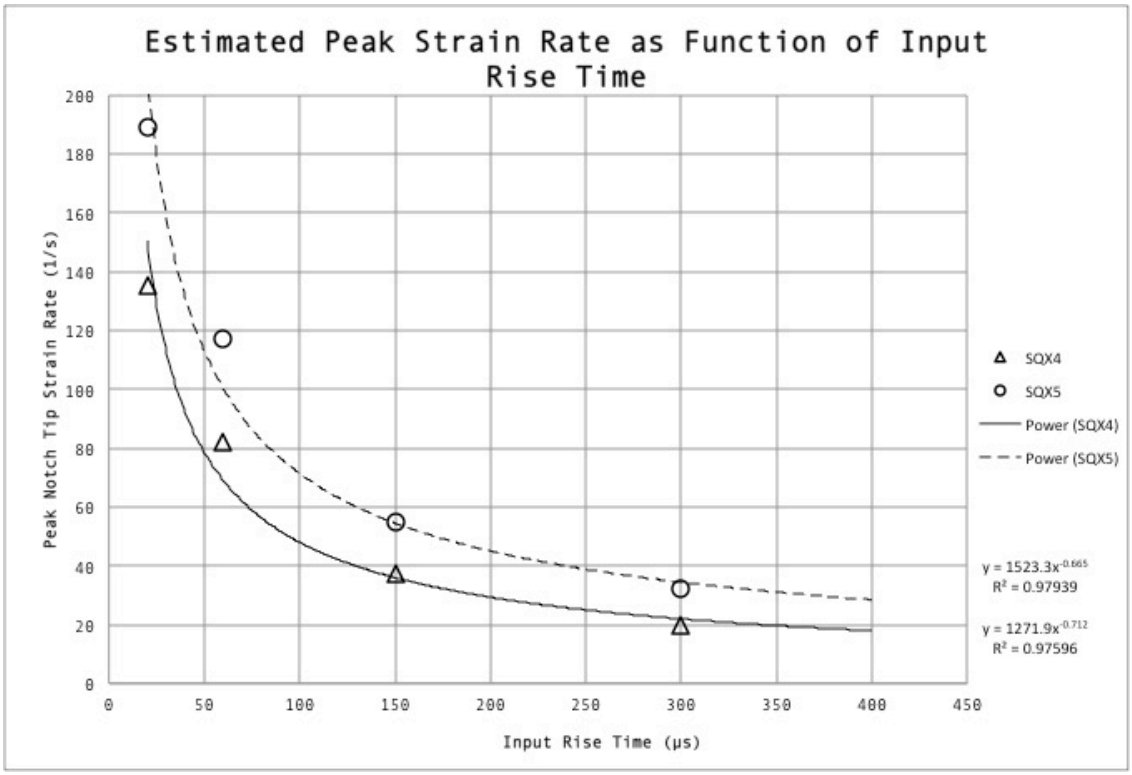

Figure 45- Peak strain rates are taken as the maximum strain rate observed in the Abaqus simulations. This is true except for the 20µs cases where harmonics dominate after ~60µs, so the peak was chosen to be the peak at around 40 µs into the experiment. The top equation is associated with SQX5.

4.3.1.1 SQX4 Peak Strain Rate Estimates

$$\dot{\varepsilon}_{p,SQX4} \approx 1271.9(t_{rise})^{-0.712}$$

4.3.1.2 SQX5 Peak Strain Rate Estimates

$$\dot{\varepsilon}_{p,SQX5} \approx 1523.3(t_{rise})^{-0.665}$$

The results of the simulations indicate that when very low input rise times are used, the actuator can be driven at speeds which are high enough to induce notch strain rates at the low end of the Kolsky bar range. Although the distortions in the signal for those high peak actuation velocities are high and impossible to remove, the strain rate histories for those samples are actually quite smooth. To reach strain rates of >100 s^{-1}, the equations predict maximum input rise times of 35 μs for SQX4 and 60 μs for SQX5. This aligns relatively well with the safe operational space for the amplifier and actuator as found in section 4.1.1. To design experiments for higher strain rates, taller samples should be used according to the equations. The equations are meant to provide rough ±10 s^{-1} estimates of the notch strain rates. This is due to the oscillations in the strain rate histories, and the imperfect fitting of the equations to the data.

4.3.2 Crack Speeds

Using the PCI images, crack speeds can be estimated by identifying the crack tip locations at each time step. Because of the increased contrast for cracks intersecting with the surface of the specimen ("front" and "rear" cracks), the tips of the cracks intersecting the surface are the most easily identifiable. Although the PCI images are only 2-D projections, the front can be distinguished from the rear because it is known what side of the notch was tilted towards the camera. For instance, in sample SQX4_4, the angle between the front sample surface normal and imaging direction was 8°. It is also important to consider the normalization techniques used for post-processing of the images due to the phase mismatch between the 153ns electron bunch spacing, and the 200ns (5 Mfps) inter-frame timing on the camera. The images were all measured for average brightness, and a distribution of brightness's was formed around an average brightness. Then, each image was corrected to the mean using the distance its original brightness was from the mean of the stack. Figure 47 shows how the cracks were identified for purposes of measuring velocity.

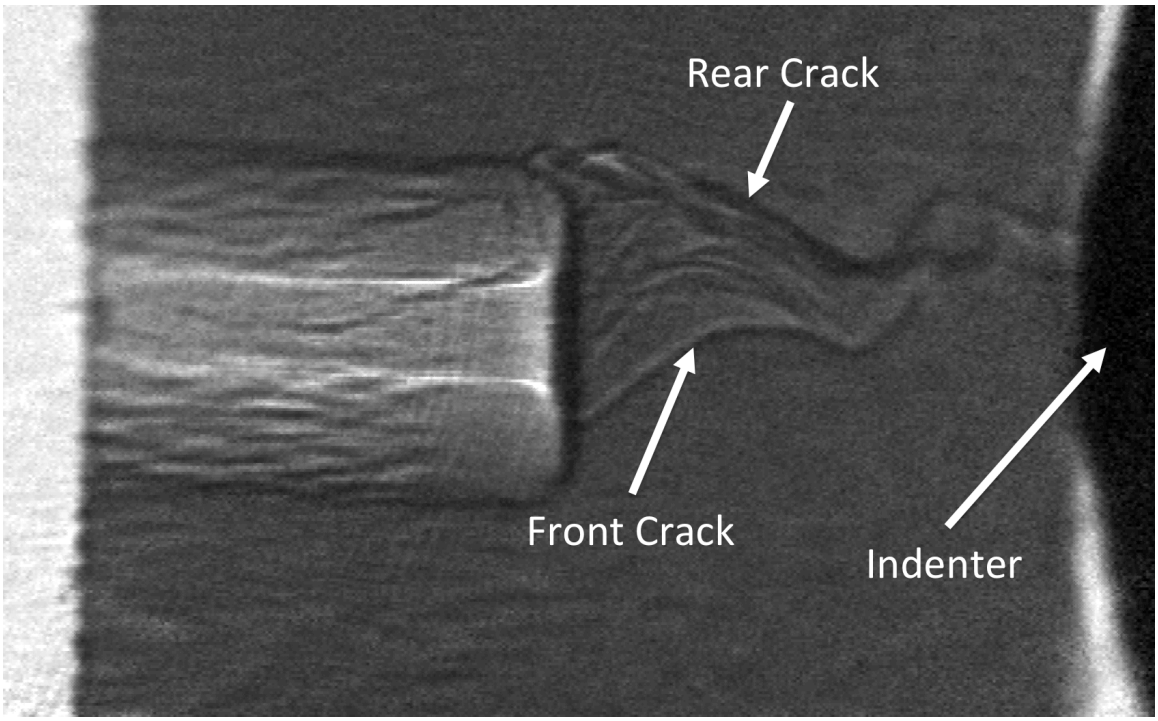

Figure 46- Identification of front and rear sample crack boundaries with indenter labeled for sample SQX4_4.

The crack speeds of these two front and rear cracks were tracked by measuring the change in position of the crack tip in both x and y. The Pythagorean theorem was used to approximate the total distance covered using the x and y pixel coordinates. The width of the view field was measured using a micrometer translation twice throughout the experiment, and was found to remain consistent during the experiment. Using the view field width, the time of each frame, and the number of pixels in the frame, the velocities were calculated and are shown for sample SQX4_4 in Figure 48 below.

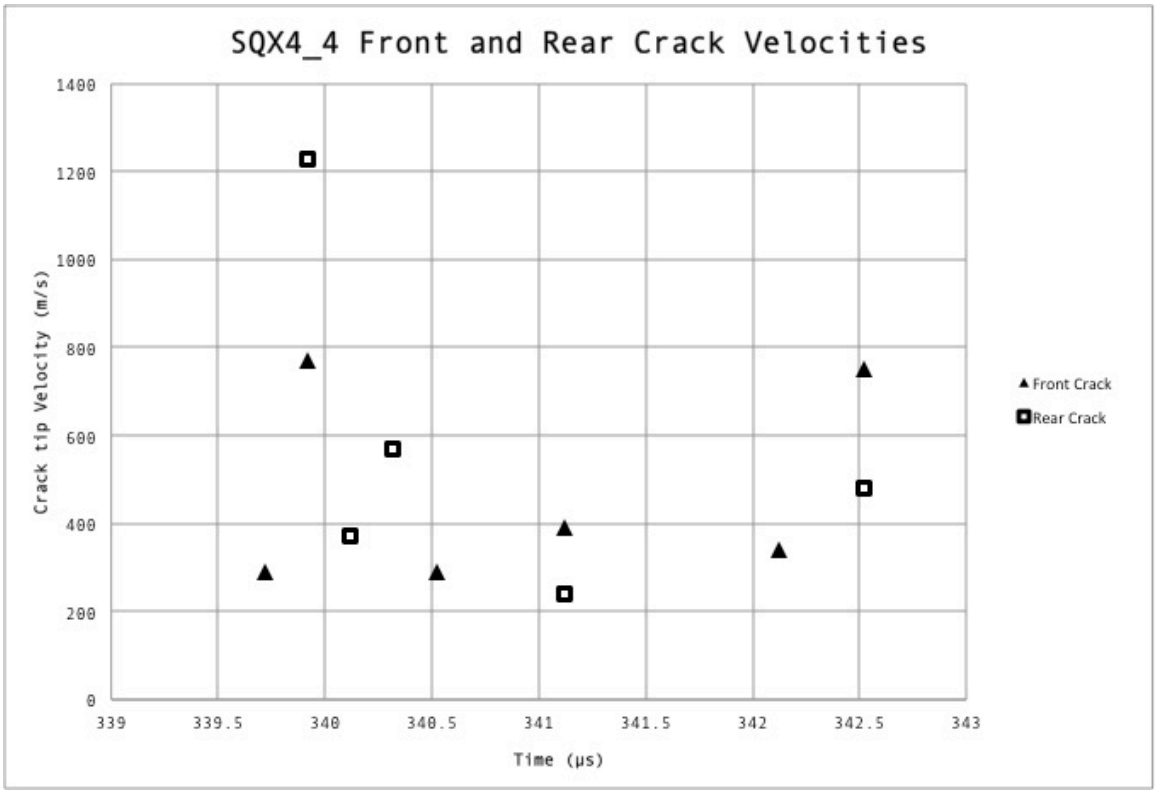

Figure 47- Crack velocities for each of the cracks identified in figure 40.

It is worth noting the sources of substantial error embedded in the measurements of crack speed here. First, when the analysis was conducted on three separate occasions, the results varied by an average of 55.7 m/s for each point. This is due strictly to experimenter error in identifying the exact tip of the crack. Second, for many frames, the crack appears to not move, so measurements are based on only a fraction of actual frames taken. If the resolution of the imaging technique improved, it would drastically improve the ability of the experimenter to accurately identify crack tip coordinates. Furthermore, the assumption that the crack tip is moving in a plane x-y plane

may reduce effective crack speeds from the actual value. Thus, these measurements should be taken as proof-of-concept evidence that crack speeds from multiple locations through the materials depth may be extracted from the PCI.

4.4 Discussion

Since the results are split into two sections, the discussion also treats the synchrotron results and the computational results as separate topics. Since there is some inherent coupling between the two categories of results in the context of the whole experiment, some discussion on the computational results may be found in the synchrotron results section and visa versa.

4.4.1 Synchrotron Results

The results from the synchrotron contain a vast array of information, but due to the scope of this work, only a few aspects of the results will be discussed.

4.4.1.1 Repeatability of Results

The results were not as repeatable as desired for a synchrotron experiment. For instance, although the velocities histories of the actuator were extremely repeatable, the performance of the specimen was not,

especially temporally. Temporal repeatability is critical for triggering of a synchrotron experiment with 5 Mfps imaging due to the 25.6 μs window that must contain the fracture event. Temporal repeatability was better in the SQX5 family as shown in Figure 38. There were 2 SQX5 trials that had peak forces within 2 N and failure times within 15 μs. However, the other SQX5 trial failed over 35 μs after the earliest albeit with consistent peak force. Although triggering was done using a force drop for the low strain rates of 20/s, in theory, the SQX5 samples are nearly consistent enough to be triggered using a nominal delay value set by the experimenter (i.e. a 300 μs delay would have captured 2/3 trials of the SQX5).

SQX4 samples faired much worse, and had an almost 100 μs spread in failure times. This does not correlate well with notch length although the spread of SQX4 notch lengths (60 μm) is 6 times that of SQX5 (10 μm) as seen in Figure 30. The order of notch length longest to shortest is SQX4_4, SQX4_3, SQX4_7. However, the order of failure time from longest to shortest is SQX4_4, SQX4_7, SQX4_3. The peak forces of the longest and shortest notches are also the closest while the middle length notch, SQX4_3, has a lower peak force. Preloads also do not seem to correlate well to failure times. The order of preloads from largest to smallest is SQX4_7, SQX4_3, SQX4_4 (reverse of the notch lengths because longer notches lead to weaker

samples). The last explanation of spread in SQX4 may be in how centered the notches were on the beam. As shown in Figures 32 (SQX4_4), 54 (SQX4_3), and 62 (SQX4_7), the only well-centered notch is SQX4_4 with SQX4_7 being low by ~300 μm, and SQX4_3 being high by ~200 μm. The only other experimental parameter that could be speculated to change the consistency of the experiment is volatility to crystal orientation. Because there was a zig-zag pattern observed in the SQX4_4 sample in particular, it may be that very small changes in notch orientation, notch chipping, etc. may force the crack to continually "decide" between cleavage planes leading to an embedded randomness from sample to sample. It is recommended that future samples are taller (while maintaining thicknesses < 1.6mm), and contain shorter, more consistent notch lengths to emulate the more consistent results observed in the SQX5 family.

4.4.1.2 Force Measurement

The force measurements also likely contain some mechanical filtering that needs to be taken into consideration. Because the piezocapacitive force sensor is in itself a mechanical oscillator, its resonant frequency of 50 kHz will prevent the measurement of any signals at higher frequencies than 50 kHz (20 μs). This can be seen in the zoomed in force history graph, Figure 31. Although the two halves of the quartz beam have completely separated,

and there is likely no force transmission (an expected vertical drop-off in force), the signal slowly drops off, and does not reach zero for another 25 μs. Additionally, the force signal can be seen oscillating at a frequency of approximately 12 kHz following the failure of the sample. This 12 kHz frequency may be due to the force sensor, oscillating as a spring, mass, damper system with the mass being the be Roller Support as shown in Figure 7. This added mass would reduce the oscillation frequency to some lower value than 50 kHz. Also, prior to fracture there are these consistently spaced drops in the rate of force at ~85 μs intervals (~12 kHz) which may also be caused by the addition of a mass to the end of the force sensor. Cumulatively, these distortions in the force signal during and after loading should not affect the peak force significantly, but likely will have an effect on the shape of the loading curve so modelers trying to match results to the exact shape of the loading curve need be mindful of its inaccuracies. Thus, the peak force values are the most useful quantitative output from the force data.

4.4.1.3 Imaging

Several limitations to the current data prevent a more in depth analysis of metrics such as crack speed and the identification of material deformation mechanisms. Foremost of these is the resolution. Our current resolution is 3

μm/pixel, although in theory this can be reduced to 1 μm/pixel [10]. Although the wavelengths of x-rays are on the order of angstroms, the thickness and properties of the scintillator drastically reduce the resolution to the scale of hundred's of nanometers. The thinner the scintillator becomes, the more refined the visible light image will be on the backside. This is due to the interaction cones formed within the crystal as shown in Figure 49. The blue lines represent dark spots that were formed from PCI as they passed through the sample. If these spots are too close to each other, once they pass through the scintillator to form a visible image, the interaction cones may overlap and form a 4^{th} even darker spot which is not present in reality. In our experiment, a robust 150 μm thick LuAg scintillator was used because the galvanometer (μs level shutter), was not yet implemented inside the hutch. Thus, the scintillator crystal was exposed to high power x-rays for long periods of time, and needed to be thick enough to withstand the heat load. The other reason for a thick scintillator is to form brighter visible light images for imaging. However, because we had sufficient visible brightness, a thinner scintillator could have been used if a galvanometer had been utilized. This would have reduced distortions in the visible light images, and enabled us to image at higher resolutions. Other improvements that could

have been made after the use of a thinner scintillator are a higher magnification tube lens, and a higher resolution camera.

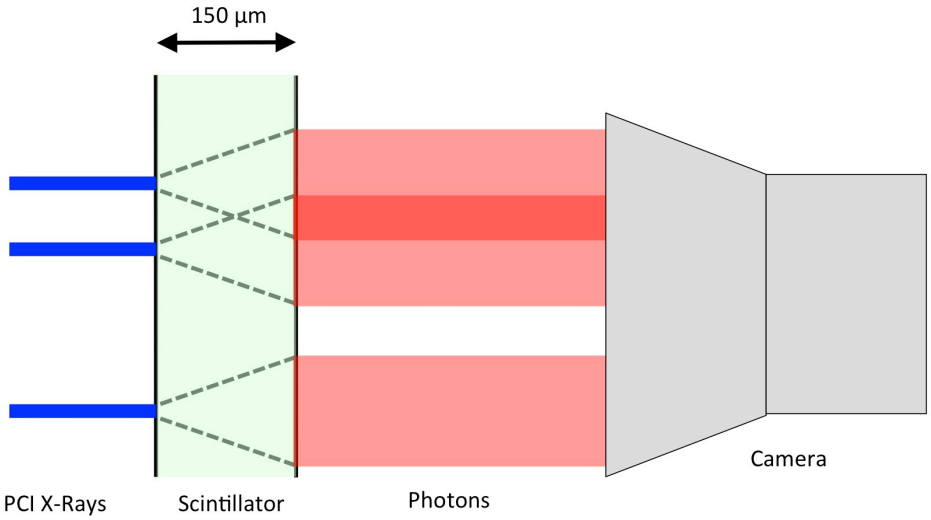

Figure 48- Illustration of the interaction cones formed inside the scintillator when x-rays get converted to visible light inside the crystal.

Other limitations to the data quality have to do with sample sizing. The thickness of the samples directly impacts the signal/noise ratio in the images. This is evidenced by the higher levels of darkness in the SQX5 series of PCI images. Although the brightness could have been increased further, some of the pixels are already near overexposure, so the maximum brightness set was based on keeping all pixels underneath the overexposure limit. The other sample dimension that could be changed is the height of the beam. With a higher beam (longer notch tip to indenter distance), and a

larger view field, crack speeds could be tracked more accurately. Currently, it seems that the cracks propagate across the specimen so fast, that only a few true data points are collected.

The crack speeds presented here contain a large amount of error. In most of the crack speed data, there are a few data points at the beginning of the event of 500+ m/s. Then in the subsequent frames, all the rest of the data, in general, is in the 100-300 m/s range. It is possible that the contrast is not high enough to see the true crack tip. The crack may have to open up by some multiple of the resolution, i.e. 3, 6, or 9 μm to see contrast from pixel to pixel. Thus, we may be tracking the speed of a "visible crack tip" which may be 100's of μm behind the actual crack tip. Thus, it is likely that the 500+ m/s data points are true crack speeds even though they are measuring the speed of an offset crack tip. However, the subsequent data points may simply be tracking rate at which contrast is formed during rigid body translation of the two fully separated halves of quartz.

4.4.1.4 Effects of Crystal Orientation

As can be seen in Figures 24 and 25, the orientation of the crystal was different (manufacturer mistake) between the SQX4 and SQX5 sample sets. It would be expected that fracture surfaces might differ between the two samples sets due to this difference in orientation. The desired orientation is

the SQX4 regime where crack propagation is promoted along the positive rhombohedral plane as observed in Tonge et. al. [24]. However, even in SQX4, it appears that this is not the case as the cracks seems to desire propagating diagonally up and to the right or down and to the right. Ball and Payne showed this "zig-zag" type of behavior for quartz crystals in uniaxial tension as early as 1976 [25]. Ball and Paynes figures of stair step fracture surfaces lack scale bars, however, so it is difficult to discern if the size of the stair steps in SQX4_4 (~250 μm) are similarly scaled to those seen in their experiment. Oddly, in SQX5_5 and SQX5_7, it does appear that the crack plane follows the notch plane rather effectively (no stair step), but the positive rhombohedra plane is almost exactly (~7˚ off) perpendicular to the notch plane in those samples. It is thus likely that crack propagation occurs on different planes than was observed in Tonge et. al. This may be due to the stress state difference between cube compression (interface failure on unloading due to tension) and 3 point bending (highly tensile character, largely plain strain stress state).

4.4.1.5 Compliance Issues

The system works excellently for samples with a low transmitted force (< 50 N), but for higher force samples like 3mm thick beams of boron carbide, the compliance of the translation stage becomes an issue. Following

the testing of the single crystal quartz, boron carbide samples were attempted. With knowledge from previous 3-point bend Kolsky bar experiments, the peak force was expected to be anywhere from 100 N to 200 N for 3mm thick beams of boron carbide. Accordingly, the preload was set to between 25 N and 30 N; much higher than the quartz samples. This was expected to elastically eliminate most of the uptake compliance in the translation stage so fracture could occur with a small additional 18 μm displacement from the actuator. However, no boron carbide sample was successfully fractured after 4 trials. Further testing at higher preloads was not possible due to time constraints. Since boron carbide testing is valuable to other research efforts, and its x-ray cross-section is very small (both B and C have low Z values), it would be very beneficial to modify PAIRLS to accommodate testing of higher force transmission tests. The force sensor can go up to 200 N accurately, and up to 500 N overload without damage so as long as the translation stage has a lower compliance, then higher forces should not be a problem. Other solutions include using thinner beams of boron carbide or using two stacked actuators in series to multiply overall displacement and velocity.

4.4.2 Computational Results

The estimation of strain rate from the computational results is a key part to this experimental method so the accuracy and convergence of the results is critical. As such, the convergence test results from the simulations are shown with some discussion, and a more in depth look is given into the methodology of estimating strain rate using simulations.

4.4.2.1 Convergence

Convergence of stress at the notch apex was established with the FEM results at a minimum element size along the notch of 500 nm. Convergence was defined by requiring a change of stress of less than 2% from previous notch seed lengths. Stress was taken as the stress 40 μs into the simulation before beam oscillations begin have a large effect. The convergence plot is shown below in Figure 50.

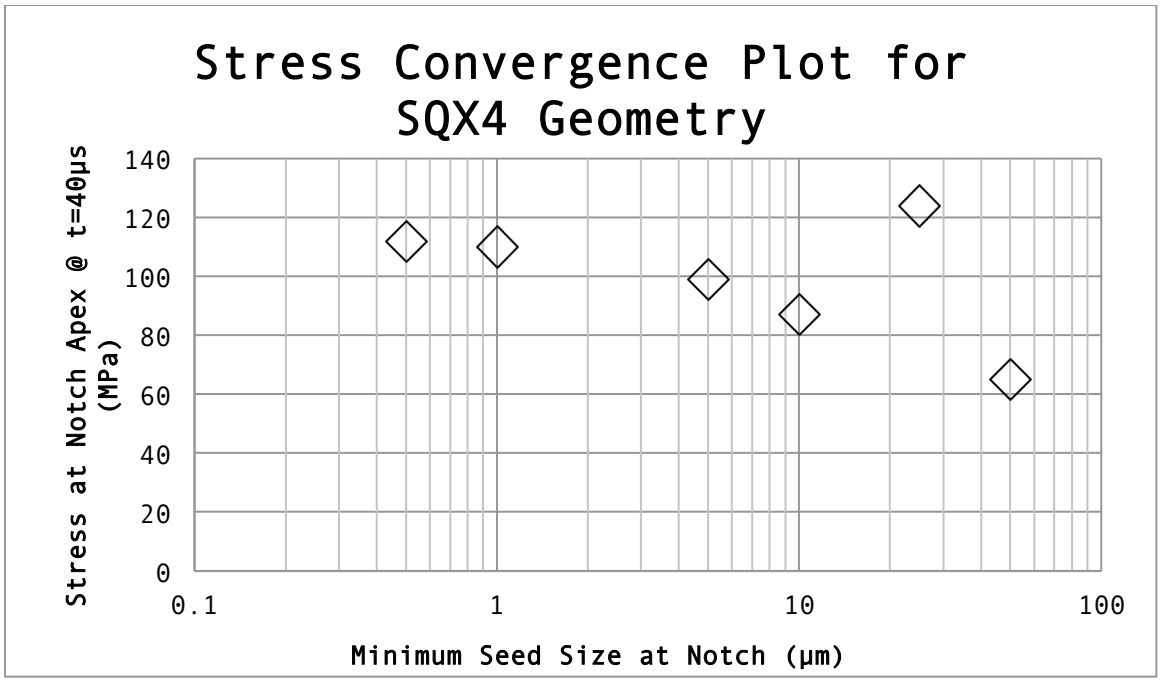

Figure 49- Stress convergence of several simulations run at decreasing minimum notch element seed sizes from 50 µm to 500 nm

4.4.2.2 Estimating Strain Rate from Input Rise Time

From the perspective of the experimenter, it is necessary to have an estimate of the strain rate of the test before the test is run. This allows for the efficient collection of data in certain strain rate ranges. Although the strain rate is most intuitively correlated with the velocity of the actuator, the experimenter does not directly control the velocity. However, the experimenter does indirectly control the velocity of the actuator by setting the input rise time of the signal generator. Thus, it is necessary to develop a simple relation between the input rise time on the signal generator, and the estimated strain

rate obtained through simulations. In Figure 44 is a graph showing the measured strain rate at the notch tip and the input rise time set on the signal generator. A power function was chosen because the relation between input rise time and peak strain rate should be inherently an inverse relation with some negative power. For the 3 point bend geometry with the actuator translating in negative y, negative strain rates (compressive strains) do not make physical sense at the notch for ε_{xx} and neither do negative rise times (actuator moving positive y) so the plot should be physically bounded to the first quadrant. The power function accomplishes this while other functions like polynomials cannot. Although a high order polynomial may be more accurate, it is more complex, and has no connection to the actual relationship between the two variables.

4.4.3 Overall PAIRLS Performance

4.4.3.1 Goals Attained

The goals presented in section 2.1 are presented again here in italics for convenience.

Primary Goals

1. The device should be small enough to transport via carry-on luggage on any domestic North American airline.

2. The device should output the time-dependent displacement of the top of the beam during loading.

3. The device should output the time-dependent force transmitted through the supports of the beam.

4. The device should be able to consistently acquire data in the collection window during the fracture process. To effectively match actuation time with imaging time, an actuation time repeatability less than +/- 100 ns will likely be required. Actuation time is defined as the time from actuator triggering to reaching 70% of max displacement. This requirement is to ensure the fracture event can be reliably captured in the context of the synchrotron shutter triggering sequence.

5. The device should be able to test 3 point bend samples of quartz, sandstone, and gneiss with lengths from 4mm to 10mm. Height and width of beams will be less than 2mm for all lengths.

6. The compliance of the superstructure should be small enough to reliably induce fracture in beams up to 100 N loads.

7. The device should be able to test three point bend specimens up to notch tip strain rates of 100 s^{-1}.

Secondary Goals

8. The device should be able to reliably induce fracture in 10mm long beams of boron carbide.

9. The device should be functional also as a fatigue loading device. This functionality should be able to produce fatigue pre-cracks in notched beams.

4.4.3.2 Attainment of Goals

1.) Partially Attained. The device can fit into an 6in tall, 8in x 12in box, but the accompanying piezoelectric amplifier, signal generator, oscilloscope, and charge amplifier cannot all fit into a carry-on luggage sized space.

2.) Attained. The method used for measuring displacements works very well when the frame rate of the camera is matched to the expected velocity of the actuator.

3.) Partially Attained. The piezoelectric force sensor works well for lower strain rates of 10-50 s^{-1}, but due to bandwidth limitations, may begin to distort signals using actuator velocities over 0.3 m/s.

4.) Not Attained. Out of the total number of tests run, only about 25% were successful. Some of these tests failed do to external beam line

problems and experimenter error so the actual failure rate of the PAIRLS system itself was closer to 35%. For efficient synchrotron data collection, this number should be at least over 50%.

5.) Partially Attained. The use of movable rollers allows the testing of a variety of different beam sizes, and 6 successful tests were conducted on quartz. However, there was no successful test on sandstone due to the lack of an actuator with large enough displacement, and other sample preparation issues.

6.) Not Attained. The excessive compliance in the precision vertical translation stage made testing samples to loads above 100 N nearly impossible because the actuator could not accommodate such large displacements in the stage.

7.) Partially Attained. Although theoretically possible given the performance of the actuator, there were many triggering issues for the samples tested at higher velocities. The maximum strain rates attained were in the 30-40 s^{-1} range, but actuator testing proved that 150+ s^{-1} is possible. With more consistent sample manufacturing, and shorter times to failure, it is quite possible that the triggering could be done using nominal delay times instead of force drops because force drops do not work well for higher strain rates.

4.4.3.3 Why Goals Were Not Met

This section references the goals not accomplished in section 4.4.3.1

4.) The failed tests can be separated into two categories. First, some experiments failed due to experimenter error. The majority of failed experiments due to experimenter error, failed because of overloading of the sample during preloading. There were two failed experiments due to adjustments that had to be made to the force drop triggering, but after the triggering was established, most failures from experimenter error were due to preloading errors. Second, the excessive compliance of the translation stage contributed to most of the failures. For all of the boron carbide samples, and a handful of SQX samples, the sample was left intact. For the SQX samples, this was largely due to lack of preloading the specimens to a high enough value, and the same for boron carbide. However, if the translation stage were stiffer, the preload amounts would not have to be as high. This could also lead to a lower failure rate due to experimenter overloading.

6.) The ability to fracture specimens with high peak force values requires a very low compliance fixture. Although the frame

compliance is very low, the translation stage compliance is very high, relatively speaking. As was described in goal 4, the inability to test high force samples like 3mm boron carbide beams is largely due to the excessive compliance in the translation stage.

4.4.4 Possible Future Utility of Results

4.4.4.1 Measurement of G_{1c}

Using the more reliable values of peak force, in theory, fracture mechanical properties of materials can be derived from experimental results. As shown in Figure 1, and the subsequent equations, for isotropic, homogeneous materials, the G_{1c} can be calculated using the peak force values, and the dimensions of the sample. However, for the single crystal quartz samples, the anisotropy in the crystal structure does not allow for the experimenter to use simply scalar values of E and ν. To further complicate matters, those equations assume a sharp crack oriented precisely vertically (line of force application is in plane of crack). SEM imaging of the notch tip showed small chipping around the edge of the notch, but no distinct sharp cracks were visible from surface secondary electron imaging. It could be that there actually are microcracks emanating from the notch in the middle of the samples thickness, but they could not be seen using the SEM as

they are too far from the edge. Also, it could be that the microcracks are present even at the surface near the chipping sites, but they are sub-micron so seeing them in a non-conductive material like quartz at that scale is extremely difficult. Supplementary nanometer thick gold-sputtered coatings may be necessary to prevent charging to image the micro cracks at that scale. Additionally, even if micro cracks are present, they are likely not optimally oriented, and techniques should be used to grow sharp cracks in the desired direction as done in Jiang et. al. [18].

4.4.4.2 Study Crack Front Shape

Most studies in the past regarding the shapes of crack fronts have been either in-situ on transparent materials like glass or epoxy [26, 27] or have been conducted post-mortem on a variety of materials [28, 29]. To the author's knowledge, very little, if any, publically available work has been done on in-situ crack front shape measurements in materials both transparent and non-transparent. This may be due to the low availability of camera technology with sub microsecond exposure times until recently. With these new in-situ techniques, it may be possible to see the crack front in non-transparent materials. In particular, the use of PAIRLS in conjunction with a

Kolsky bar would allow for the study of crack front shape as a function of strain rate.

4.4.4.3 Study of Crack Front Waves

It may be possible to see propagating crack waves in-situ with improvements in optics. Fineberg et. al. studied crack front waves optically in transparent materials using a shadowgraph method, and measured the velocity using the change in resistance of a conductive coating on the surface of the specimen [6]. Using a collimated incoherent light source, the sample was backlit so that small changes in the flatness of the transparent surface caused a local defocusing of light. This allowed for the visualization of very small changes in the flatness of the sample surface caused by crack front waves. The deviations in sample surface height from the waves were 3 μm, so with increasing resolution of the technique, it could be possible to visualize internal crack front waves if they cause local cracking above the micron scale. If crack front waves do not cause local cracking in the bulk material, it may be impossible to visualize them using x-rays because in PCI, the x-rays will not diffract off of internal strain fields/surface height variations as visible light does.

4.4.5 Recommendations

Main recommendations primarily have to do with the further optimization of the loading system for use across a wide variety of samples. Although the system works well for low reaction force quartz, It could not reliably induce fracture in 3mm x 3mm x 10mm beams of notched boron carbide. This is believed to be due to excessive compliance (>20 μm) in the vertical translation stage at loads of 60 N and above. To mitigate this problem, the preload could be increased drastically, but to avoid fracturing specimens during the preload phase, the system should be redesigned to include two translation stages in series. The first translation stage would have very low compliance, but would also have very low accuracy (±25 microns). On top of this stiff stage would be an amplified piezoelectric actuator, which could be carefully advanced to induce a small preload to ensure full contact.

5 Summary and Conclusions

A novel, portable device for observing fracture behavior in 3-point bend specimens was developed and tested. Finite element analysis was conducted using both static and dynamic linear elastic computational

methods to design the device, calculate strain rate in samples, and estimate notch stress during failure. Proof of concept tests using phase contrast imaging were conducted at the Advanced Photon Source to show functionality at the lower end of intermediate strain rates. Further study using this device could explore higher strain rates, or different brittle material systems.

The system largely functioned as designed for small single crystal quartz beams. It filled the gap of strain rates between the Kolsky bar tests and the quasi-static tests. Also, for small beams, the signal/noise ratio in the Kolsky bar was too high so this device also provided otherwise unattainable data for small specimens. The results show that, for brittle systems, a small-displacement piezoelectric actuator can be used to induce fracture at relatively predictable time scales. Crack speeds, and possibly crack front shapes can be investigated using these techniques. Upgrades may include a stiffer translation stage, or replacing the translation stage with an amplified piezoelectric actuator. Although proof of concept has been shown with transparent materials where x-ray imaging utility is low, the device should function equally as well with non-transparent materials of similar dimensions.

6 References

[1] North American Aerospace Defense Command. Office of History. A Brief History of NORAD. Pg. 16, 2012. Print.

[2] Wong, T., & Baud, P. (2012). The brittle-ductile transition in porous rock: A review. Journal of Structural Geology, 44, 25–53. http://doi.org/10.1016/j.jsg.2012.07.010

[3] Nemat-Nasser, S., and H. Horii (1982), Compression-induced nonplanar crack extension with application to splitting, exfoliation, and rockburst, J. Geophys. Res., 87(B8), 6805–6821, doi:10.1029/JB087iB08p06805.

[4] J. Kimberley, K.T. Ramesh, N.P. Daphalapurkar, A scaling law for the dynamic strength of brittle solids, Acta Materialia, Volume 61, Issue 9, May 2013, Pages 3509-3521, ISSN 1359-6454, http://dx.doi.org/10.1016/j.actamat.2013.02.045.

[5] P.R Guduru, A.T Zehnder, A.J Rosakis, G Ravichandran, Dynamic full field measurements of crack tip temperatures, Engineering Fracture Mechanics, Volume 68, Issue 14, September 2001, Pages 1535-1556, ISSN 0013-7944, http://dx.doi.org/10.1016/S0013-7944(01)00045-5.

[6] Fineberg, J., Sharon, E. & Cohen, G. Int J Fract (2003) 119: 247. doi:10.1023/A:1023954211188

[7] Guangli Hu, K.T. Ramesh, Buyang Cao, J.W. McCauley, The compressive failure of aluminum nitride considered as a model advanced ceramic, Journal of the Mechanics and Physics of Solids, Volume 59, Issue 5, May 2011, Pages 1076-1093, ISSN 0022-5096, http://dx.doi.org/10.1016/j.jmps.2011.02.003.

[8] Jensen, B.J., *Dynamic Experiments Using IMPULSE at the Advanced Photon Source*. Seminar given at New Mexico Tech. November 2013.

[9] E. Ferrié, J. Y. Buffière, W. Ludwig, "3D Visualisation of Short Crack Propagation in Al Alloy Using High Resolution Synchrotron X-Ray Microtomography", Materials Science Forum, Vol. 482, pp. 227-230, 2005

[10] Luo, S. N. and Jensen, B. J. and Hooks, D. E. and Fezzaa, K. and Ramos, K. J. and Yeager, J. D. and Kwiatkowski, K. and Shimada, T., Gas gun shock experiments with single-pulse x-ray phase contrast imaging and diffraction at the Advanced Photon Source, Review of Scientific Instruments, 83, 073903 (2012), DOI: http://dx.doi.org/10.1063/1.4733704

[11] J.E. Field, S.M. Walley, W.G. Proud, H.T. Goldrein, C.R. Siviour, Review of experimental techniques for high rate deformation and shock studies, International Journal of Impact Engineering, Volume 30, Issue 7, August 2004, Pages 725-775, ISSN 0734-743X, http://dx.doi.org/10.1016/j.ijimpeng.2004.03.005.

[12] ASTM Standard F736-95 (2011). Standard Test Method for Impact Resistance of Monolithic Polycarbonate Sheet by Means of a Falling Weight.

[13] Song, B., Chen, W. & Lu, W. J, Compressive Mechanical Response of a Low-Density Epoxy Foam at Various Strain Rates, Mater Sci (2007) 42: 7502. doi:10.1007/s10853-007-1612-z

[14] ASTM Standard C1421-16 (2016). Standard Test Methods For Determination of Fracture Toughness of Advanced Ceramics at Ambient Temperature.

[15] Casem, D.T., Dwivedi, A.K., Swab, J.J. et al., Analysis of a Three-Bar Kolsky Apparatus for High-Rate Three-Point Flexure, J. Dynamic Behavior Mater. (2015) 1: 75. doi:10.1007/s40870-014-0002-2.

[16] Klepaczko J. R., Application of the split Hopkinson pressure bar to fracture dynamics. In Mechanical Properties at High Rates of Strain, Institute of Physics Conference, Bristol, 1979, Ser. 47, pp. 201–214.

[17] F. Zhou, J.-F. Molinari, Y. Li, Three-dimensional numerical simulations of dynamic fracture in silicon carbide reinforced aluminum, Engineering Fracture Mechanics, Volume 71, Issues 9–10, June–July 2004, Pages 1357-1378, ISSN 0013-7944, http://dx.doi.org/10.1016/S0013-7944(03)00168-1.

[18] Jiang, Fengchun and Vecchio, Kenneth S., Experimental investigation of dynamic effects in a two-bar/three-point bend fracture test, Review of Scientific Instruments, 78, 063903 (2007), DOI:

[19] NIST Physical Reference Data (US Department of Commerce, 1st May, 2016), retrieved http://www.nist.gov/pml/data/xcom.

[20] A. P. Dorey and J. H. Moore, Advances in Actuators, Institute of Physics Publishing, 1995. Print. http://dx.doi.org/10.1063/1.2746630

[21] T. Sashida and T. Kenjo, An Introduction to Ultrasonic Motor, Clarendon Press, Oxford, 1993.

[22] www.physikinstrumente.com

[23] Thor Labs Technical Publications, Piezoelectric Tutorial, https://www.thorlabs.com/NewGroupPage9.cfm?ObjectGroup_ID=5030

[24] Andrew L. Tonge, Jamie Kimberley, K.T. Ramesh, The mechanism of compressive unloading failure in single crystal quartz and other brittle solids, International Journal of Solids and Structures, Volume 49, Issue 26, 15 December 2012, Pages 3923-3934, ISSN 0020-7683, http://dx.doi.org/10.1016/j.ijsolstr.2012.08.021.

[25] Ball, A. & Payne, B.W. J Mater Sci (1976) 11: 731. doi:10.1007/BF01209461

[26] Dally, J.W. Experimental Mechanics (1979) 19: 349. doi:10.1007/BF02324250

[27] Heepe, L., Kovalev, A. E., Filippov, A. E., & Gorb, S. N. (2013). Adhesion Failure at 180 000 Frames per Second: Direct Observation of the Detachment Process of a Mushroom-Shaped Adhesive. *Phys. Rev. Lett.*, *111*(10), 104301. http://doi.org/10.1103/PhysRevLett.111.104301

[28] H. Hosseini-Toudeshky, G. Sadeghi, H.R. Daghyani, Experimental fatigue crack growth and crack-front shape analysis of asymmetric repaired aluminium panels with glass/epoxy composite patches, Composite Structures, Volume 71, Issues 3–4, December 2005, Pages 401-406, ISSN 0263-8223

[29] Sherman, D. and Be'ery, I. (2011) 'Shape and energies of a dynamically propagating crack under bending', *Journal of Materials Research*, 18(10), pp. 2379–2386. doi: 10.1557/JMR.2003.0333.

7 Appendix

7.1 Actuator Testing Results

7.1.1 80 µs Input Rise Time

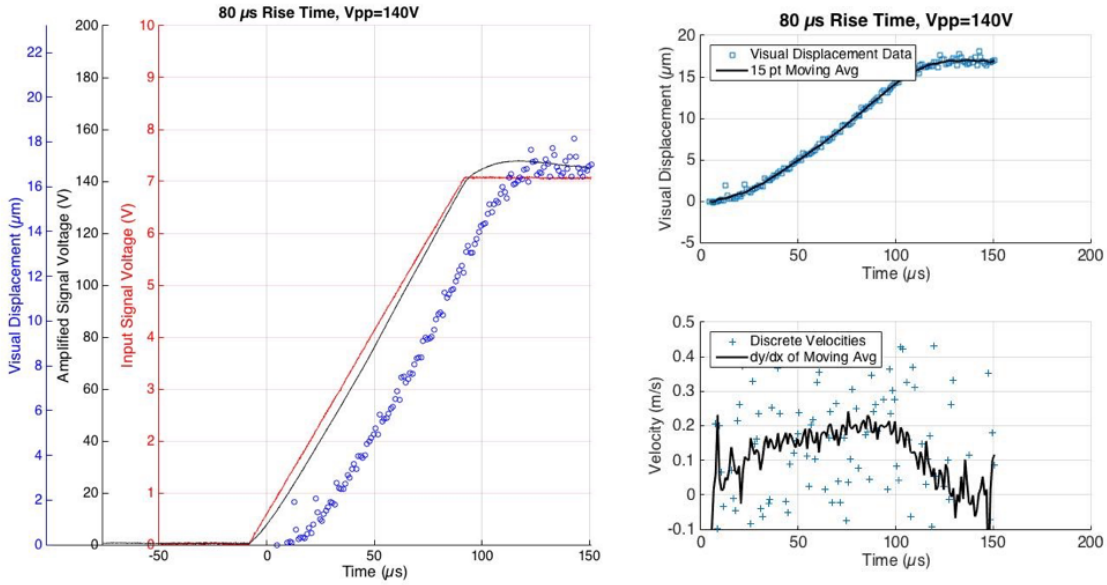

7.1.1.1.1 Figure 50- Actuator testing data for an 80 µs input rise time. Displacement tracked at 1,00,000 fps

7.1.2 60 µs Input Rise Time

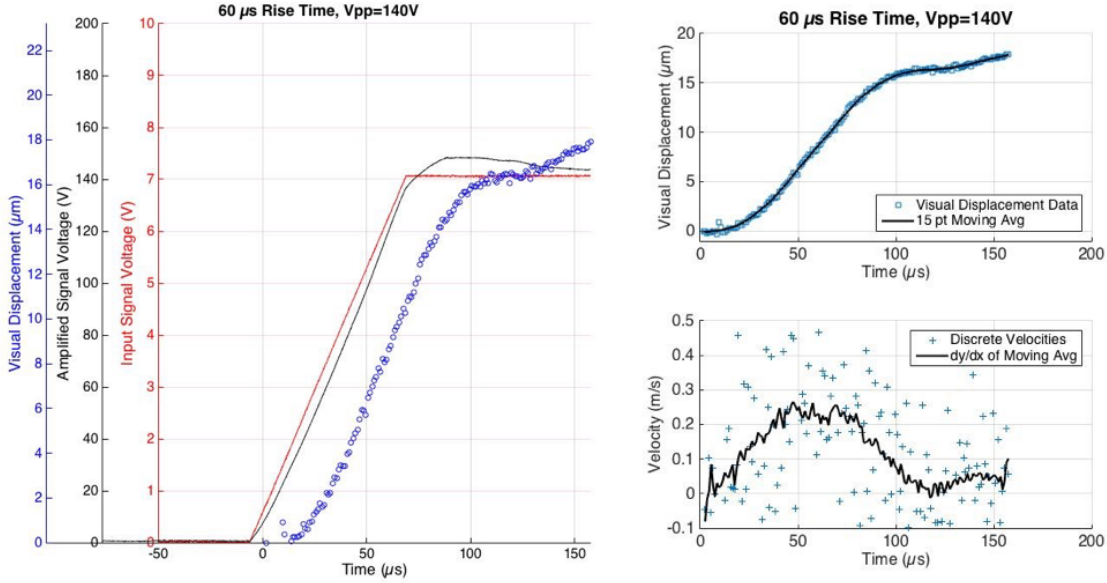

7.1.2.1.1 Figure 51- Actuator testing data for a 60 µs input rise time. Displacement tracked at 1,000,000 fps

7.1.3 40 µs Input Rise Time

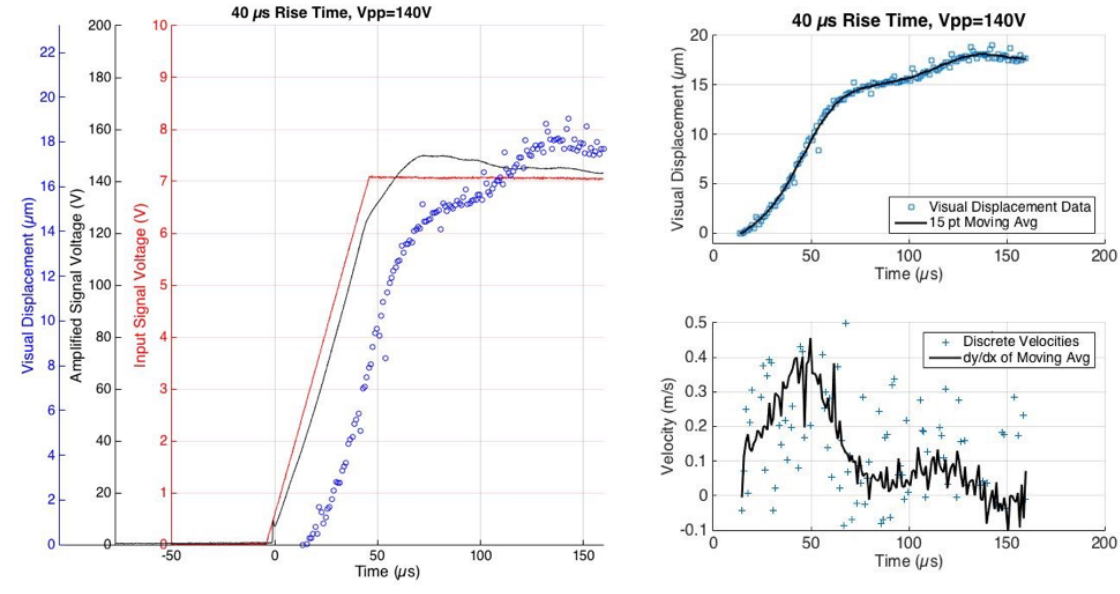

7.1.3.1.1 Figure 52- Actuator testing data for a 40 µs input rise time. Displacement tracked at 1,000,000 fps

7.1.4 15 µs Input Rise Time

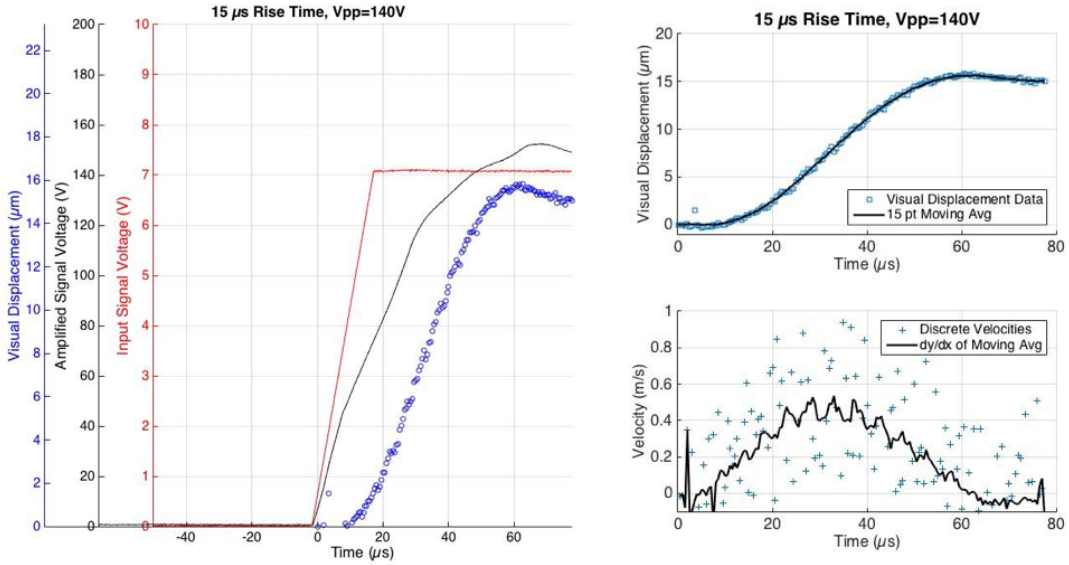

7.1.4.1.1 Figure 53- Actuator testing data for a 15 µs input rise time. Displacement tracked at 2,000,000 fps

7.1.5 10 µs Input Rise Time

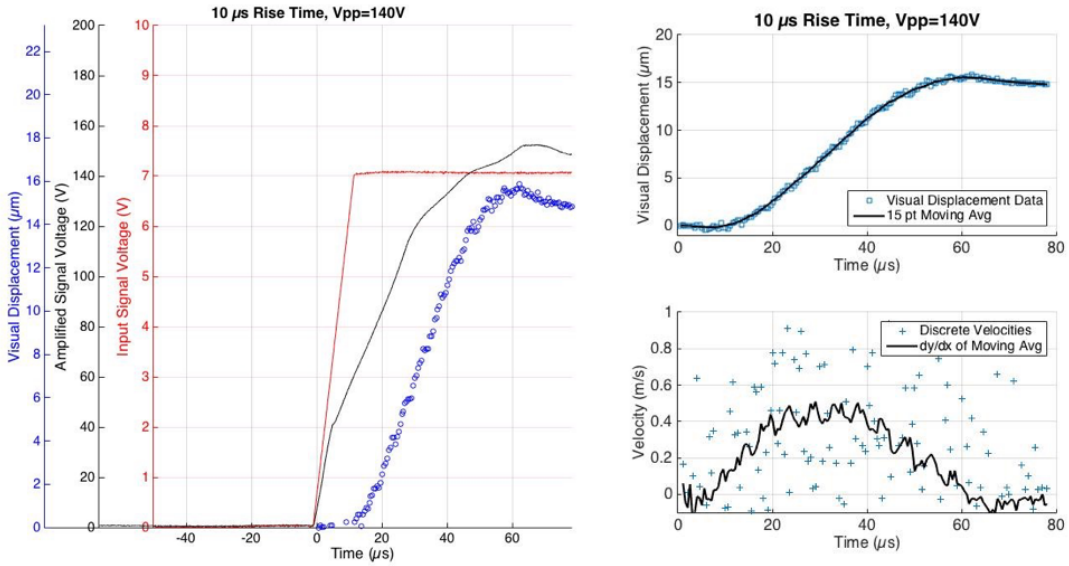

7.1.5.1.1 Figure 54- Actuator testing data for a 10 µs input rise time. Displacement tracked at 2,000,000 fps

7.2 Synchrotron Testing Results

7.2.1 SQX4_3

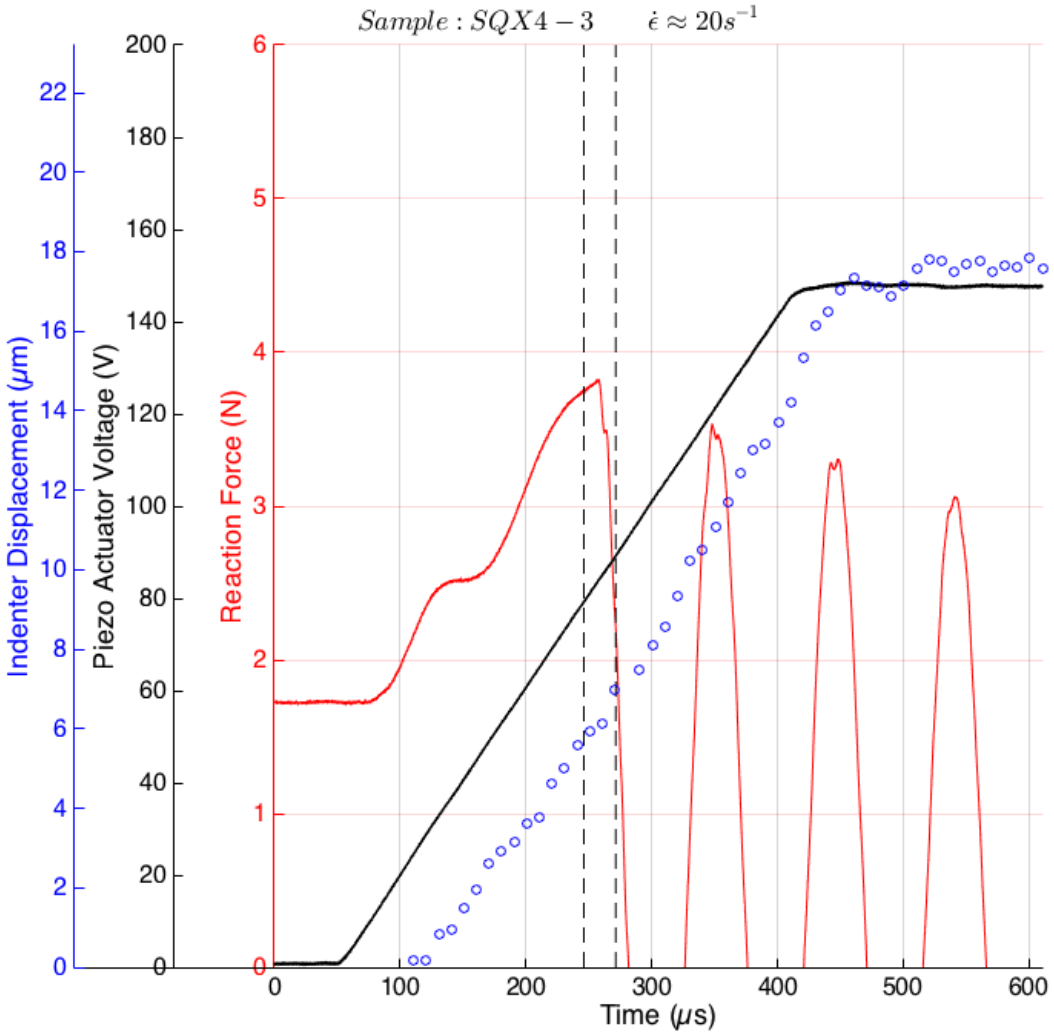

7.2.1.1.1 Figure 55- Actuator displacement was imaged at 100,000 fps. PCI Images were taken at 16.146 keV. Sample preload was 1.62 N

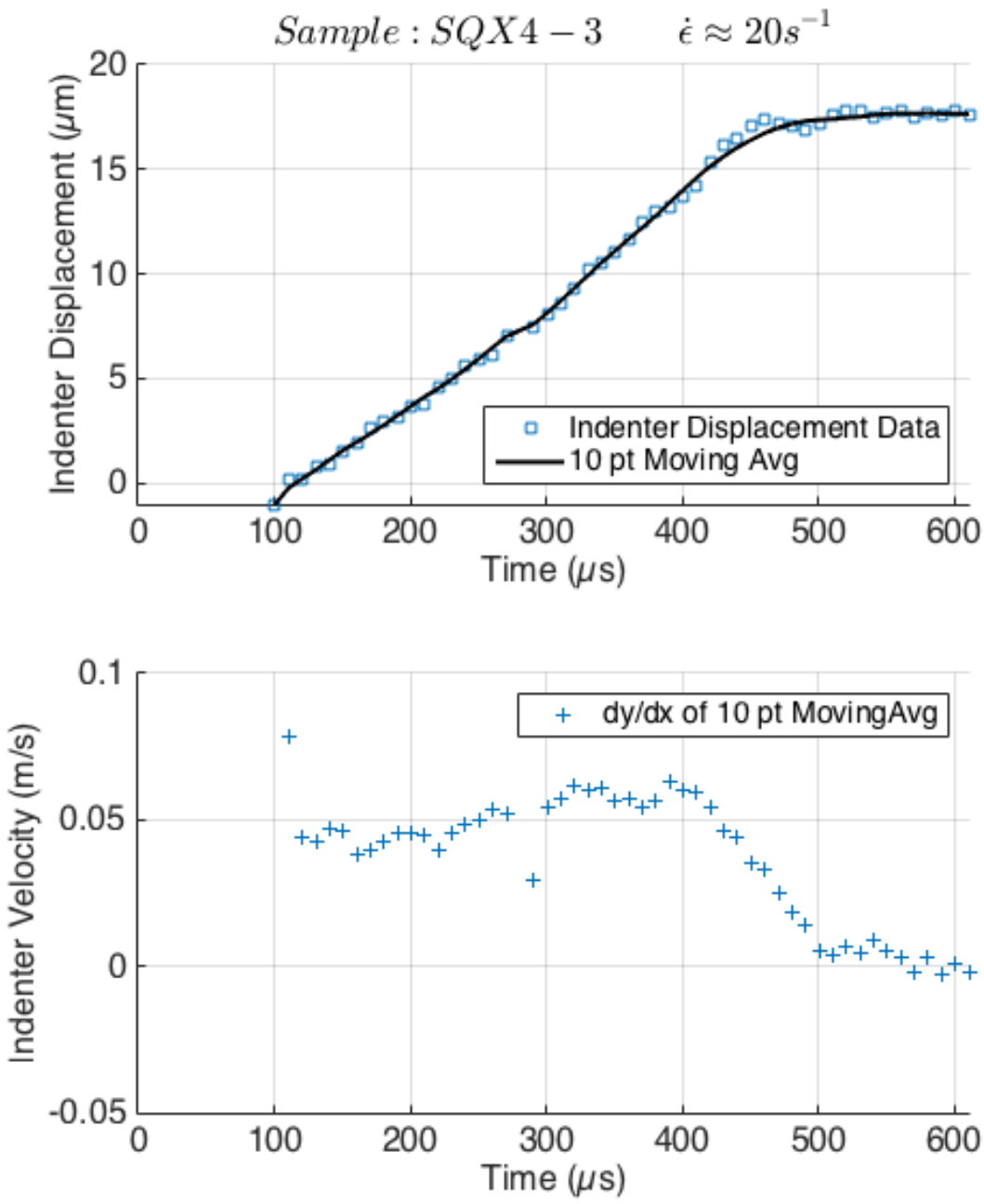

7.2.1.1.2 Figure 56- Top: Indenter displacement with a 10 pt moving average fit. Bottom: Indenter velocity generated from discrete derivatives of the 10 pt moving average fit.

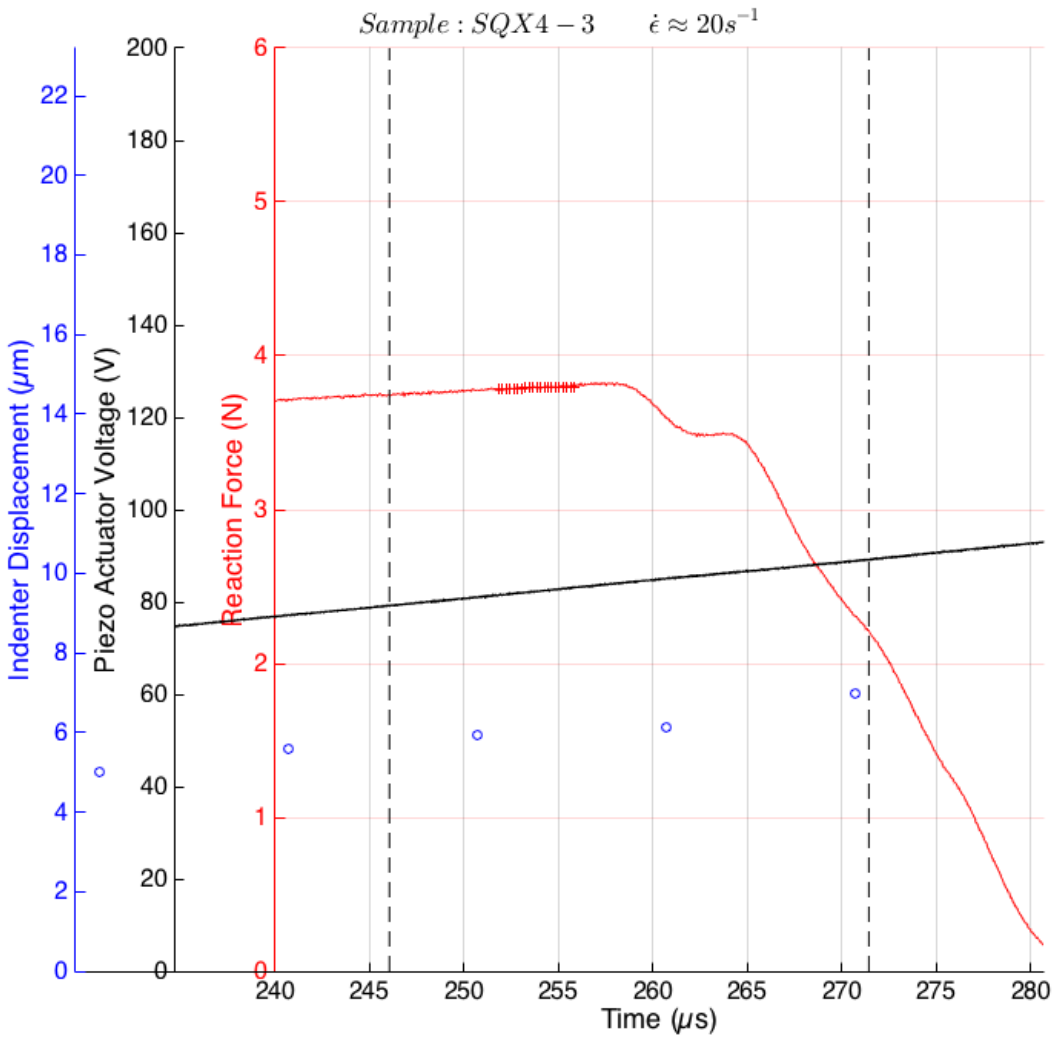

7.2.1.1.3 Figure 57-Vertical dotted lines indicate the beginning and end of the phase contrast imaging window. Small cluster of red markers on F(t) curve indicates the window from crack nucleation to complete fracture for t=[251.84, 255.84] μs

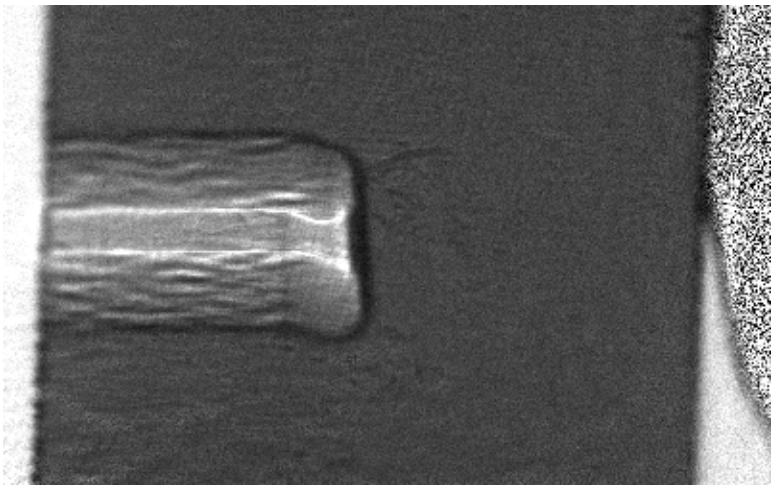

7.2.1.1.4 Figure 58- PCI image at t=251.84 µs.

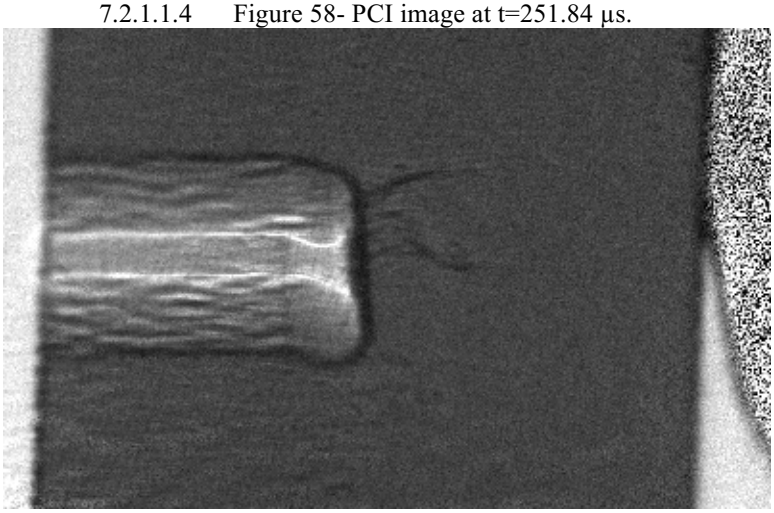

7.2.1.1.5 Figure 59- PCI image at t=252.84 µs.

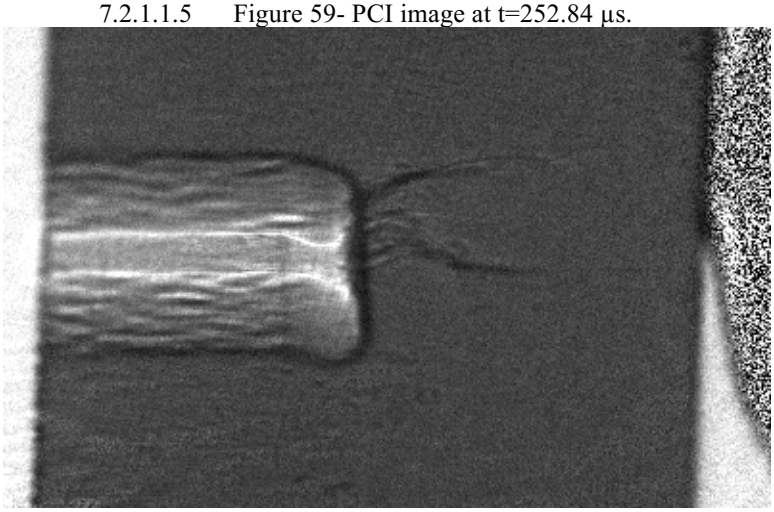

7.2.1.1.6 Figure 60- PCI image at t=254.44 µs.

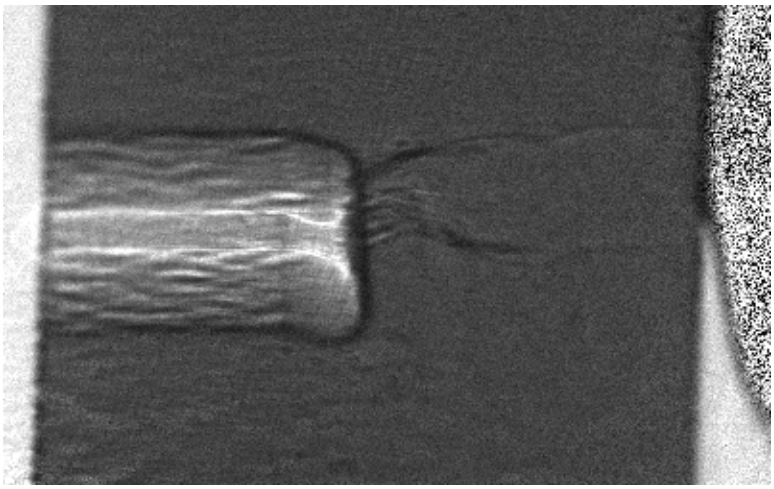

7.2.1.1.7 Figure 61- PCI image at t=255.84 µs.

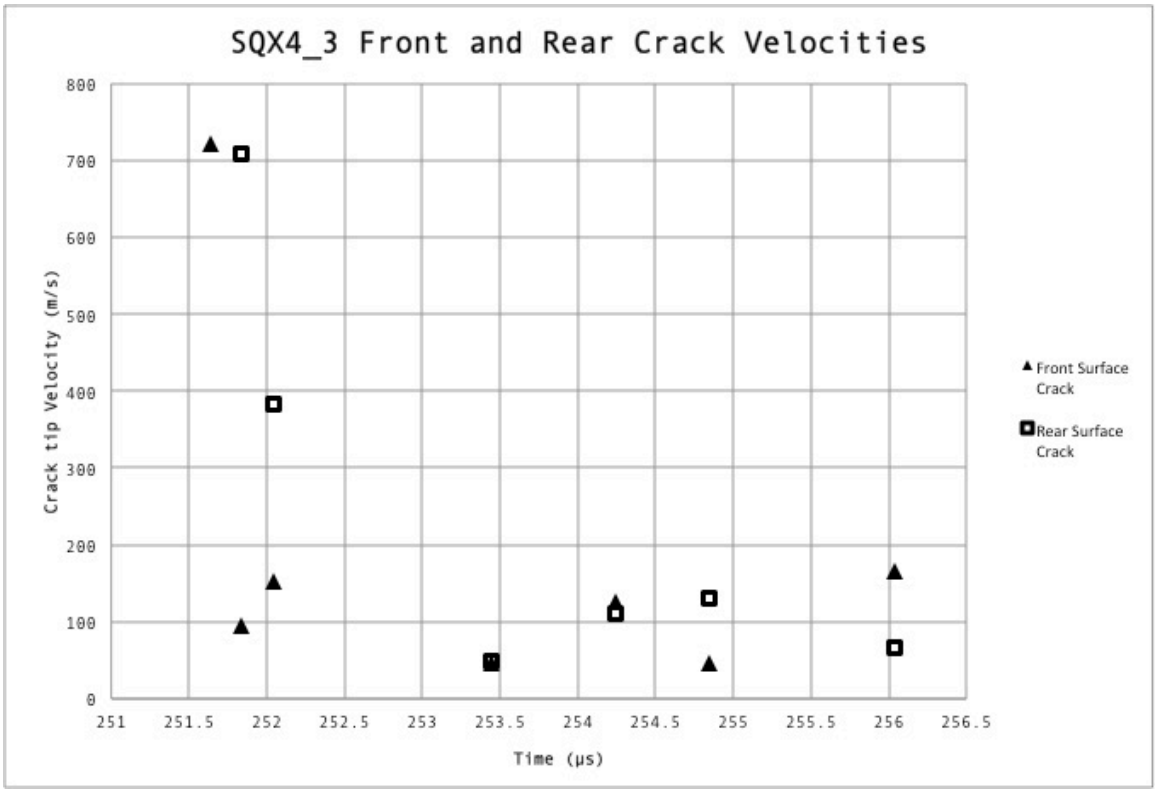

7.2.1.1.8 Figure 62- Crack velocities are shown based off estimated crack tip locations for frames that showed a significant change in crack tip location.

7.2.2 SQX4_7

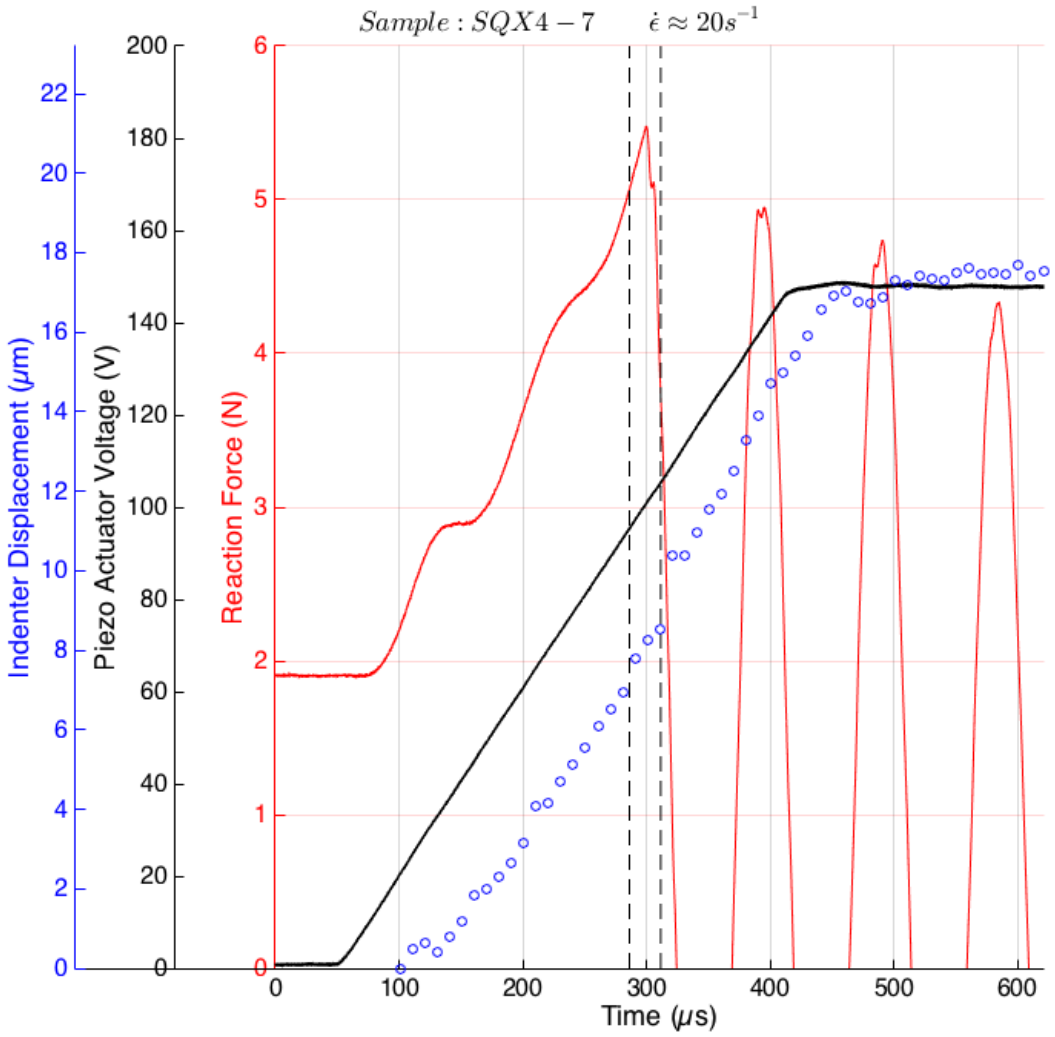

7.2.2.1.1 Figure 63- Actuator displacement was imaged at 100,000 fps. PCI images were taken at 15.902 keV. Sample preload was 1.87 N.

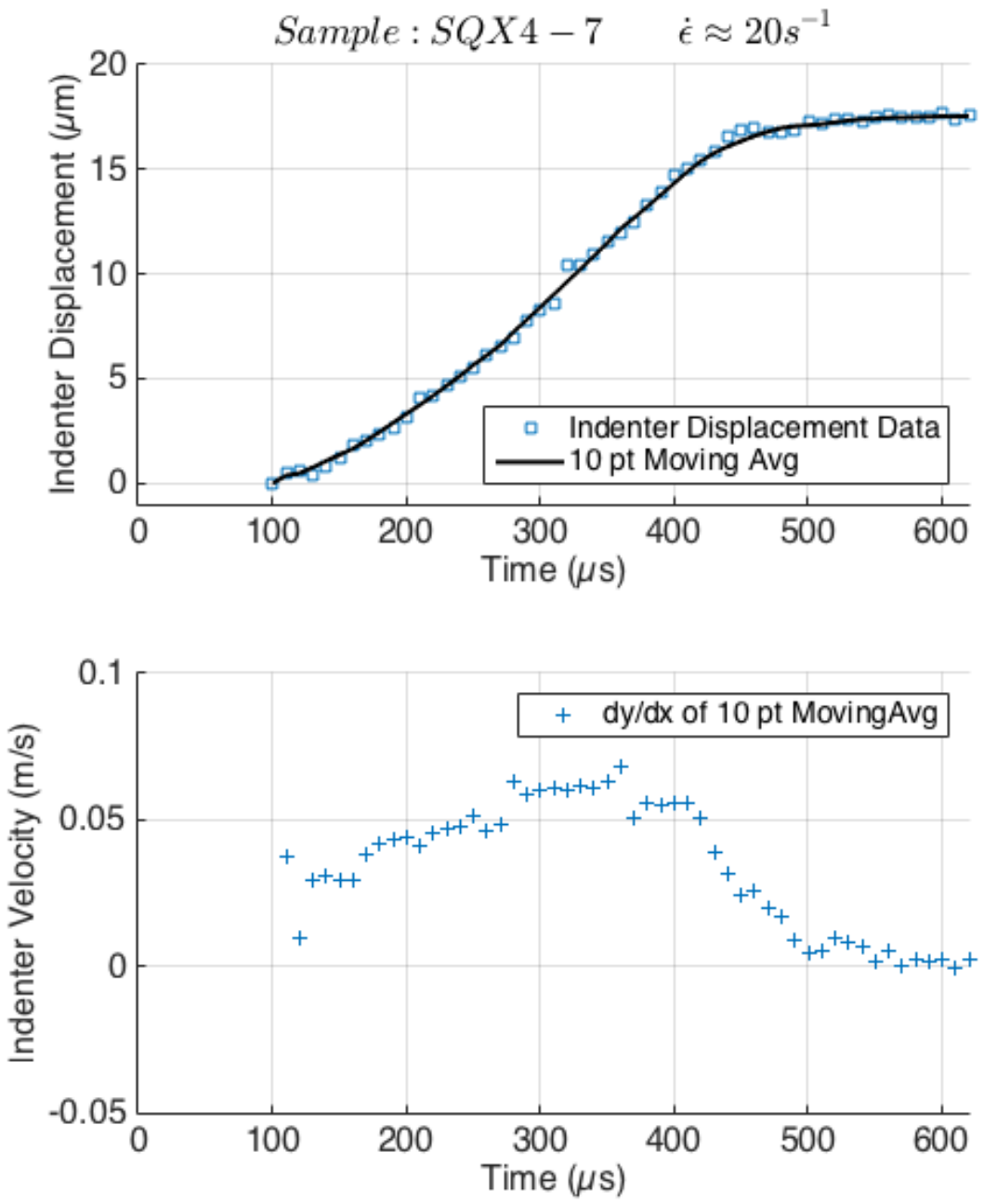

7.2.2.1.2 Figure 64- Top: Indenter displacement with a 10 pt moving average fit. Bottom: Indenter velocity generated from discrete derivatives of the 10 pt moving average fit.

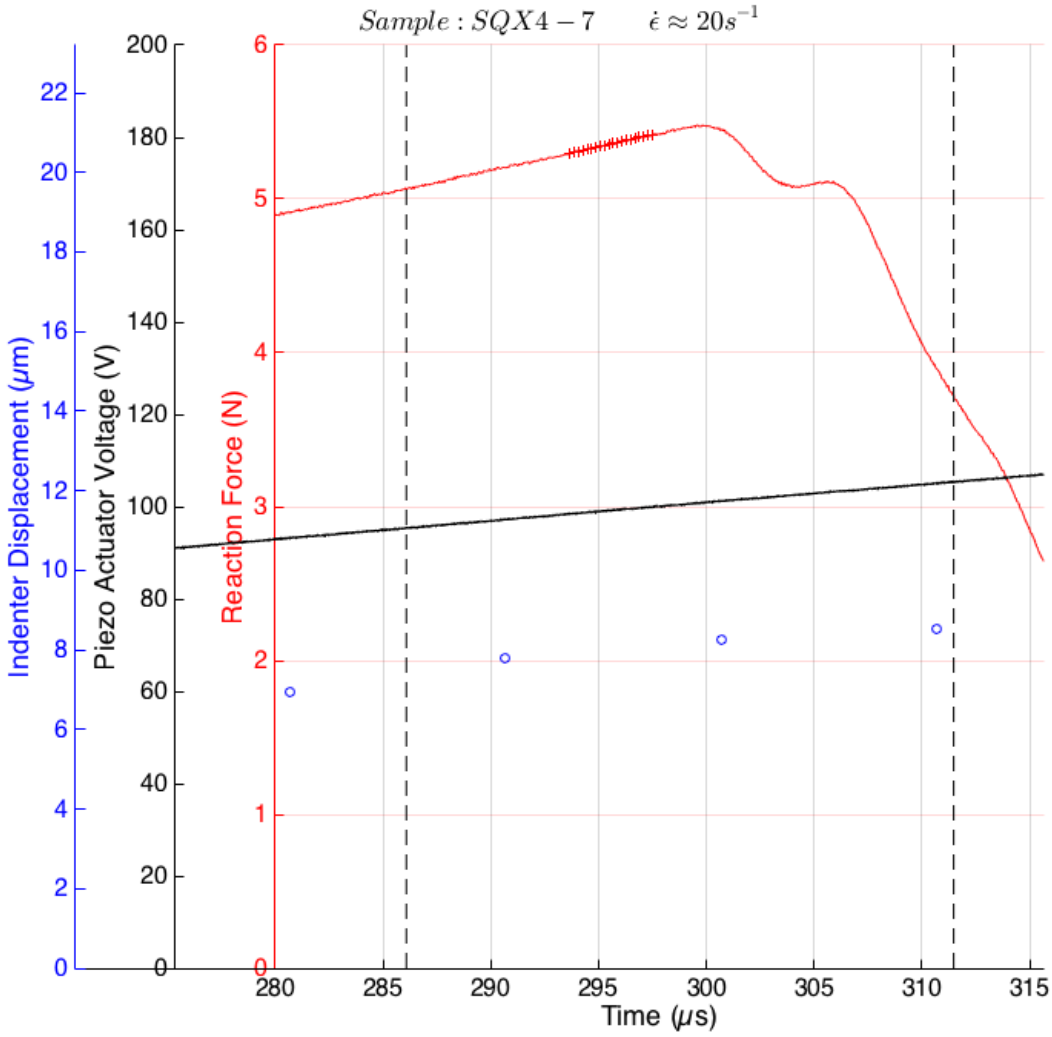

7.2.2.1.3 Figure 65-Vertical dotted lines indicate the beginning and end of the phase contrast imaging window. Small cluster of red markers on F(t) curve indicates the window from crack nucleation to complete fracture for t=[293.68, 297.68] μs

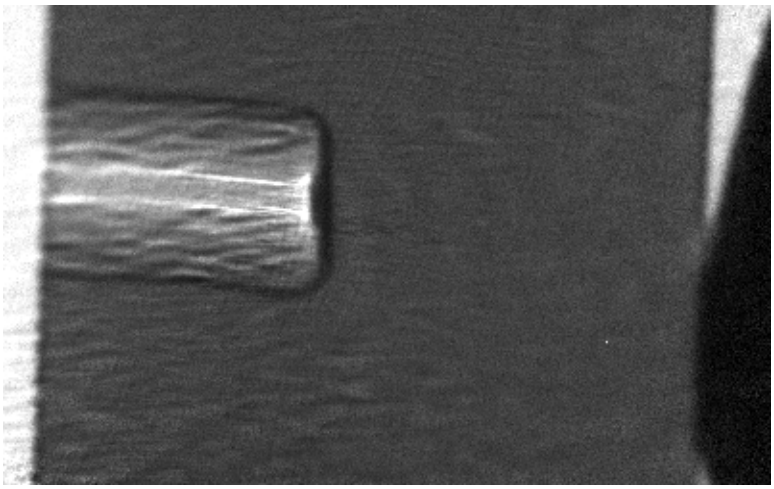

7.2.2.1.4 Figure 66- PCI image at t=293.68 μs.

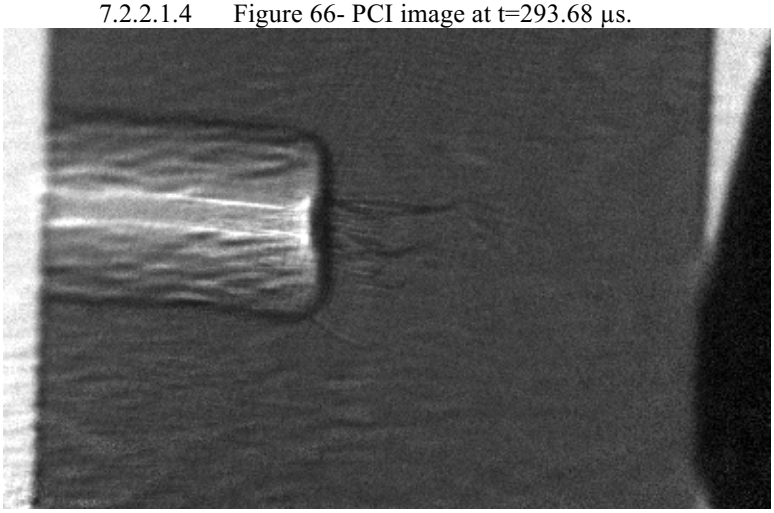

7.2.2.1.5 Figure 67- PCI image at t=294.88 μs

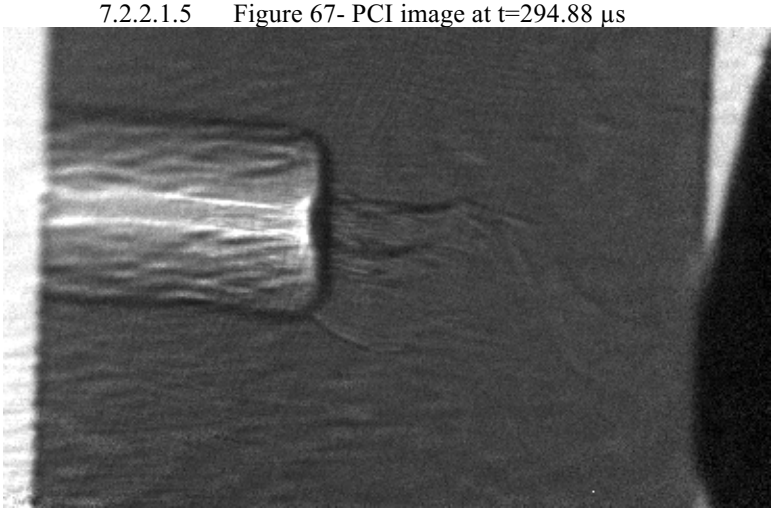

7.2.2.1.6 Figure 68- PCI image at t=296.28 μs

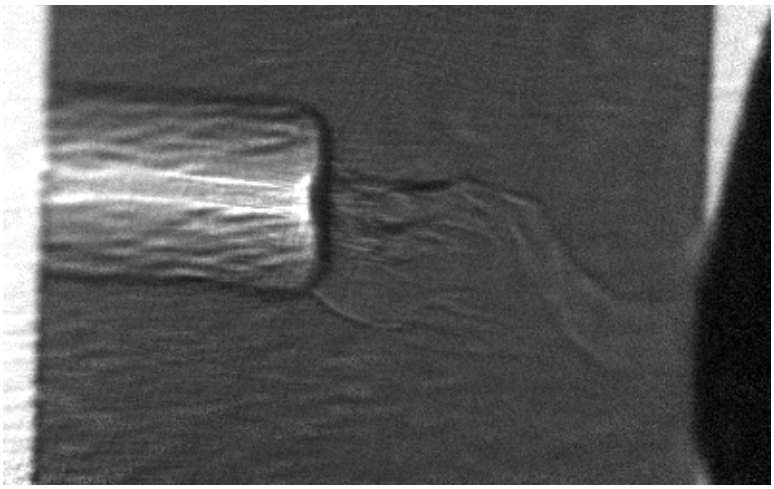

7.2.2.1.7 Figure 69- PCI image at t=297.68 μs

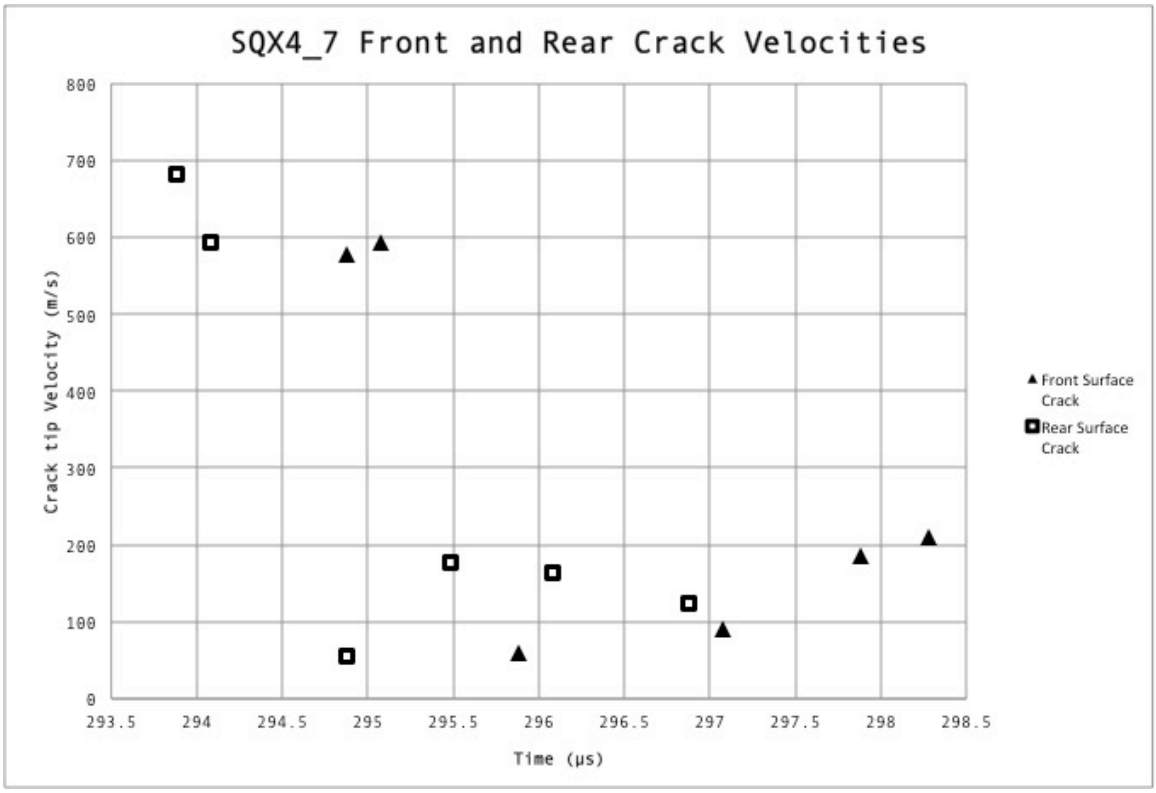

7.2.2.1.8 Figure 70- Crack velocities are shown based off estimated crack tip locations for frames that showed a significant change in crack tip location.

7.2.3 SQX5_5

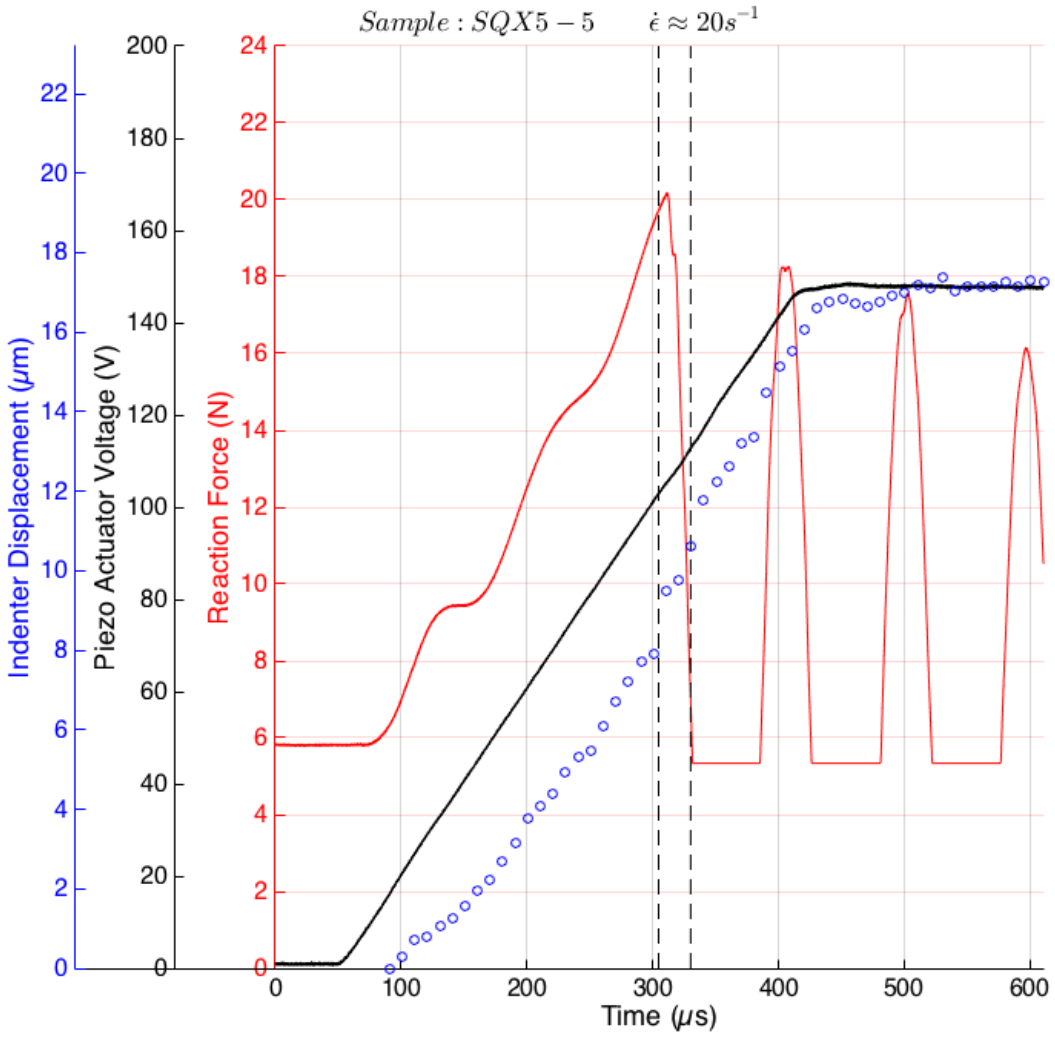

7.2.3.1.1 Figure 71- Actuator displacement was imaged at 100,000 fps. PCI images were taken at 16.146 keV. Sample preload was 5.95 N.

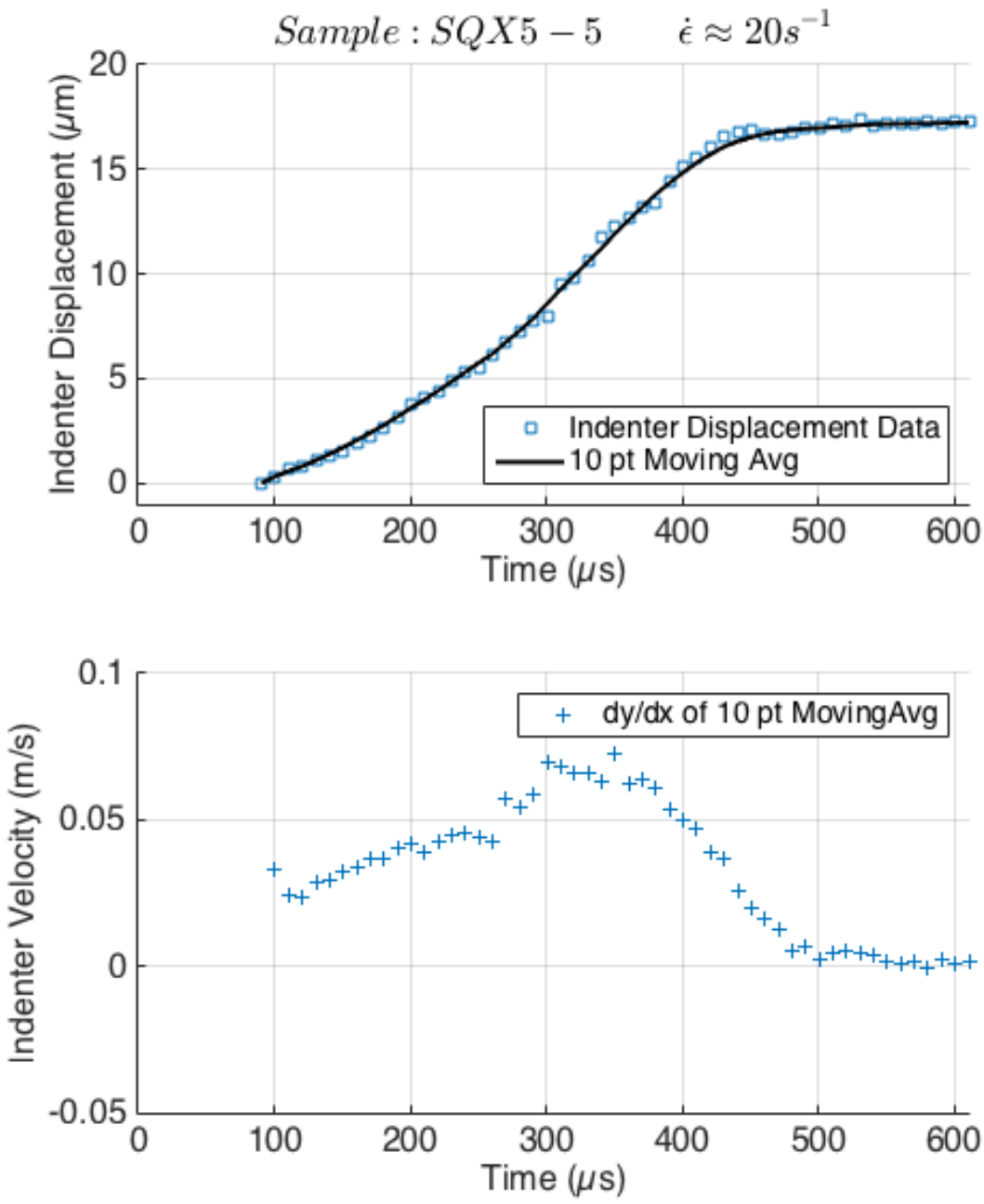

7.2.3.1.2 Figure 72- Top: Indenter displacement with a 10 pt moving average fit. Bottom: Indenter velocity generated from discrete derivatives of the 10 pt moving average fit.

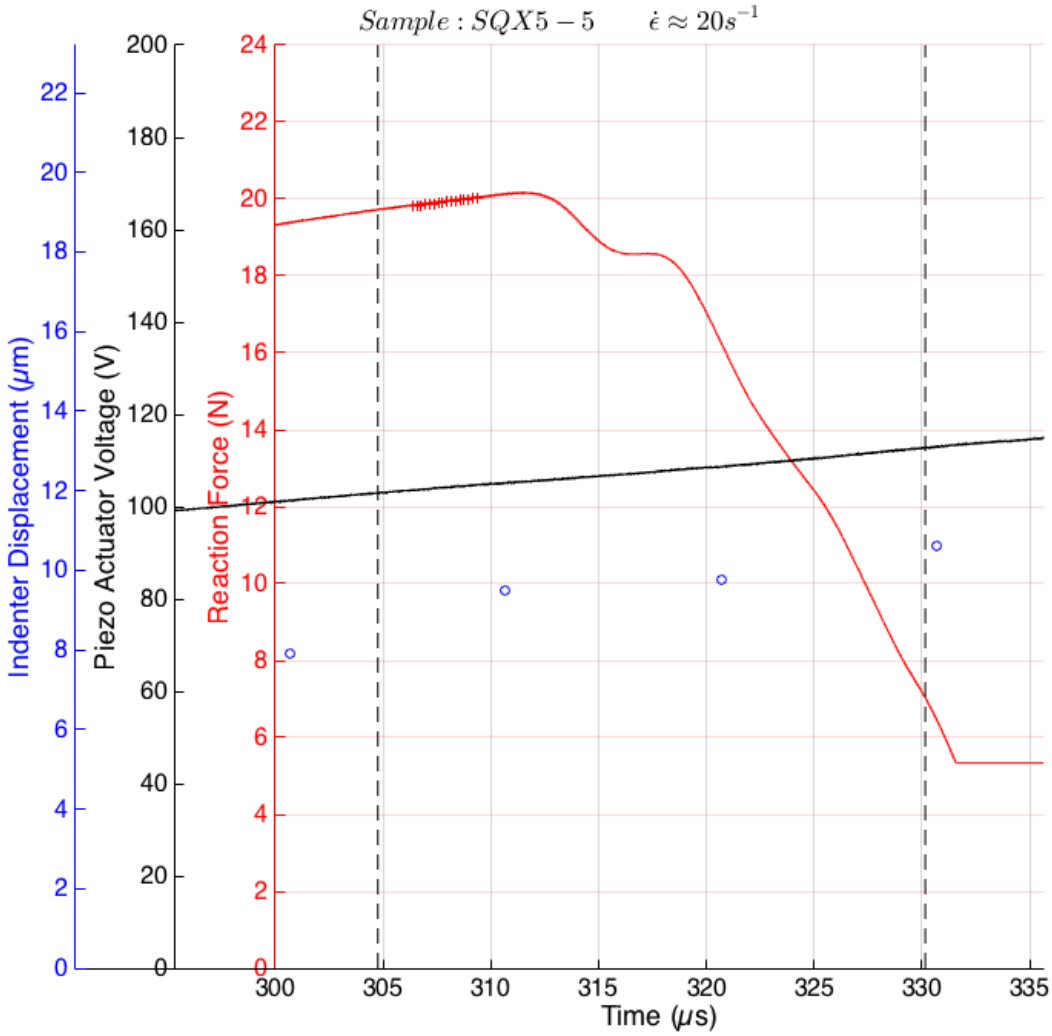

7.2.3.1.3 Figure 73- Vertical dotted lines indicate the beginning and end of the phase contrast imaging window. Small cluster of red markers on F(t) curve indicates the window from crack nucleation to complete fracture for t=[306.36, 309.56] μs

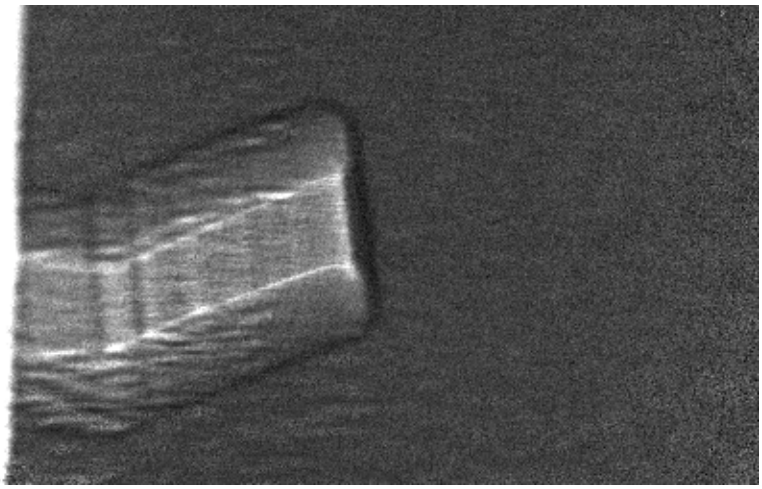

7.2.3.1.4 Figure 74- PCI image at t=306.36 μs

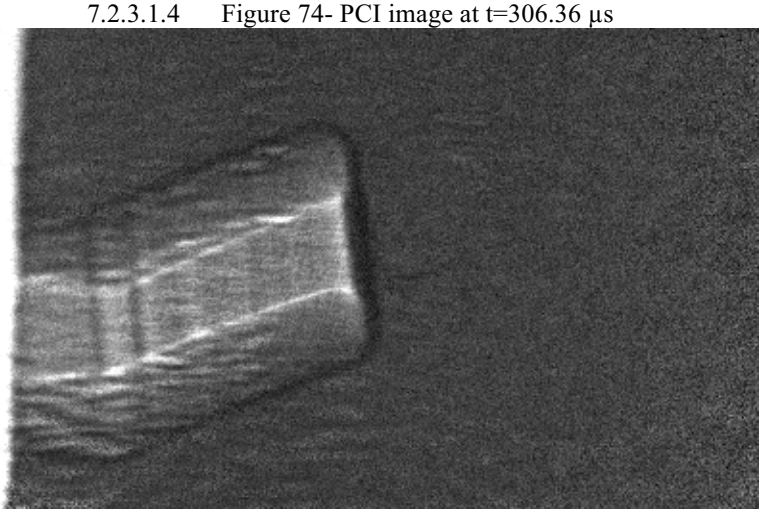

7.2.3.1.5 Figure 75- PCI image at t=307.56 μs

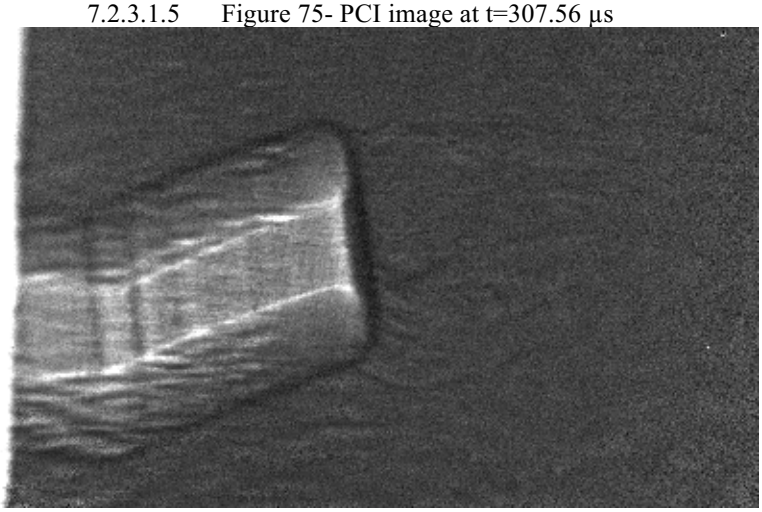

7.2.3.1.6 Figure 76- PCI image at t=308.56 μs

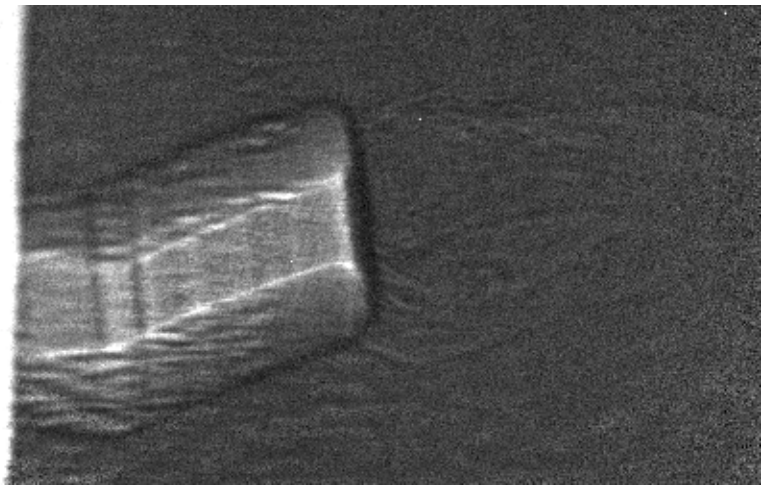

7.2.3.1.7 Figure 77- PCI image at t=309.56 μs

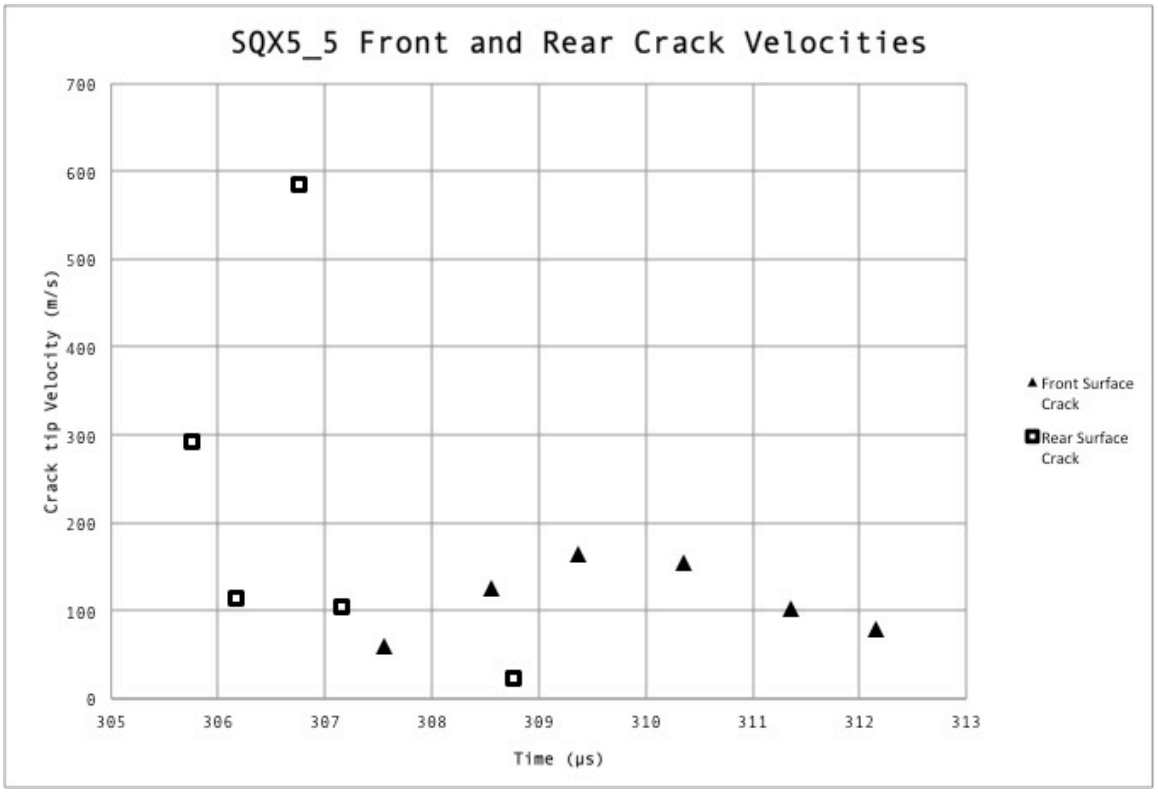

7.2.3.1.8 Figure 78- Crack velocities are shown based off estimated crack tip locations for frames that showed a significant change in crack tip location. Errors in SQX5 velocities are higher than SQX4 due to thicker samples and consequently less contrast.

7.2.4 SQX5_6

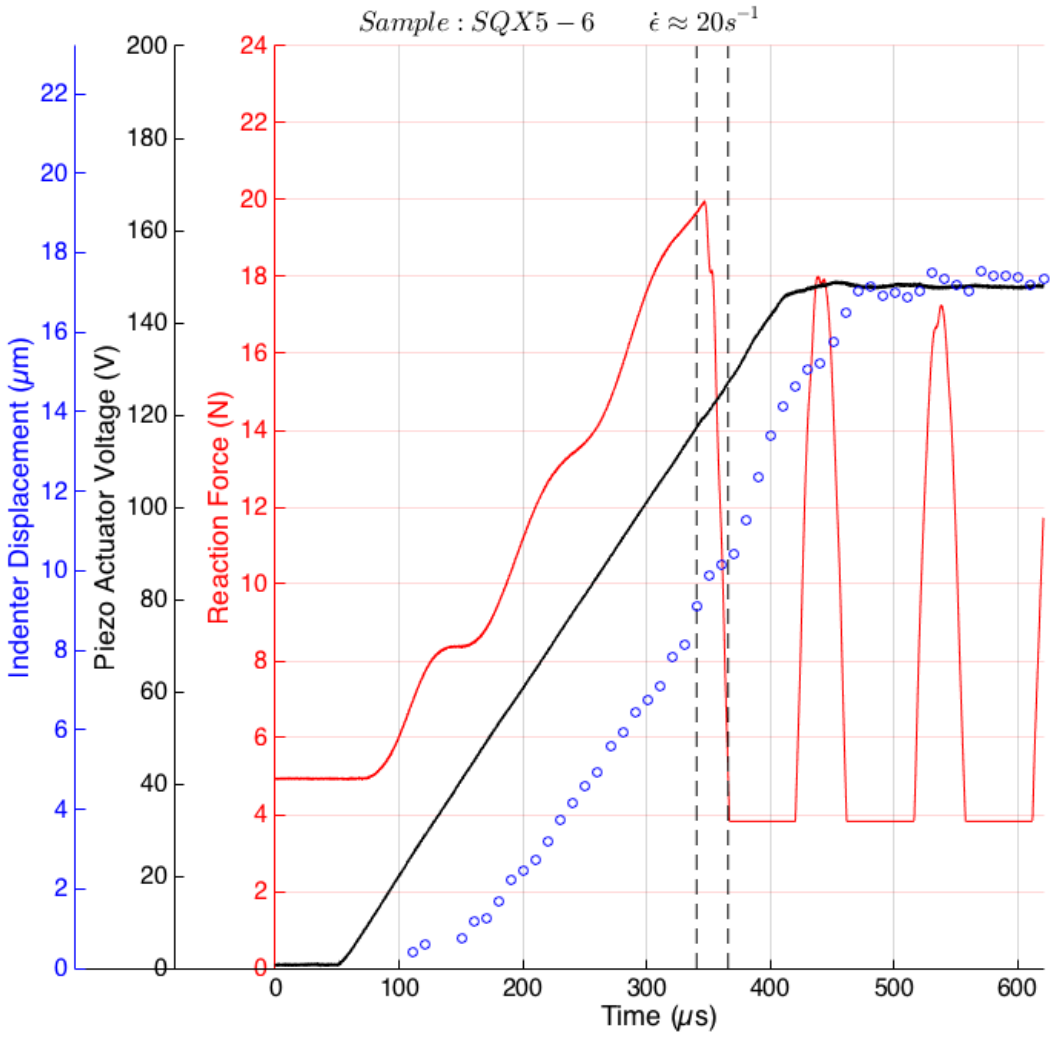

7.2.4.1.1 Figure 79- Actuator displacement was imaged at 100,000 fps. PCI images were taken at 16.146 keV. Sample preload was 4.69 N.

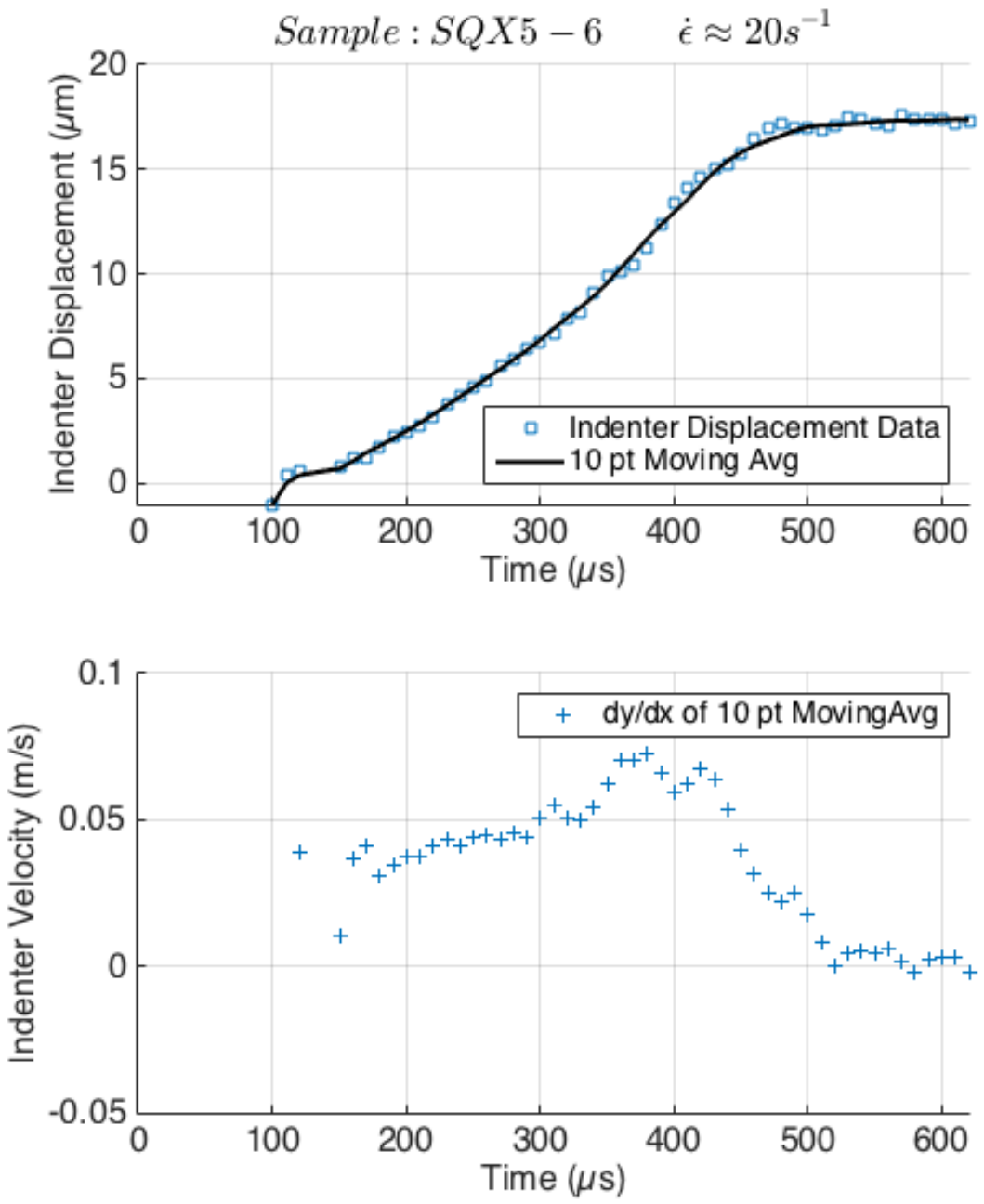

7.2.4.1.2 Figure 80- Top: Indenter displacement with a 10 pt moving average fit. Bottom: Indenter velocity generated from discrete derivatives of the 10 pt moving average fit.

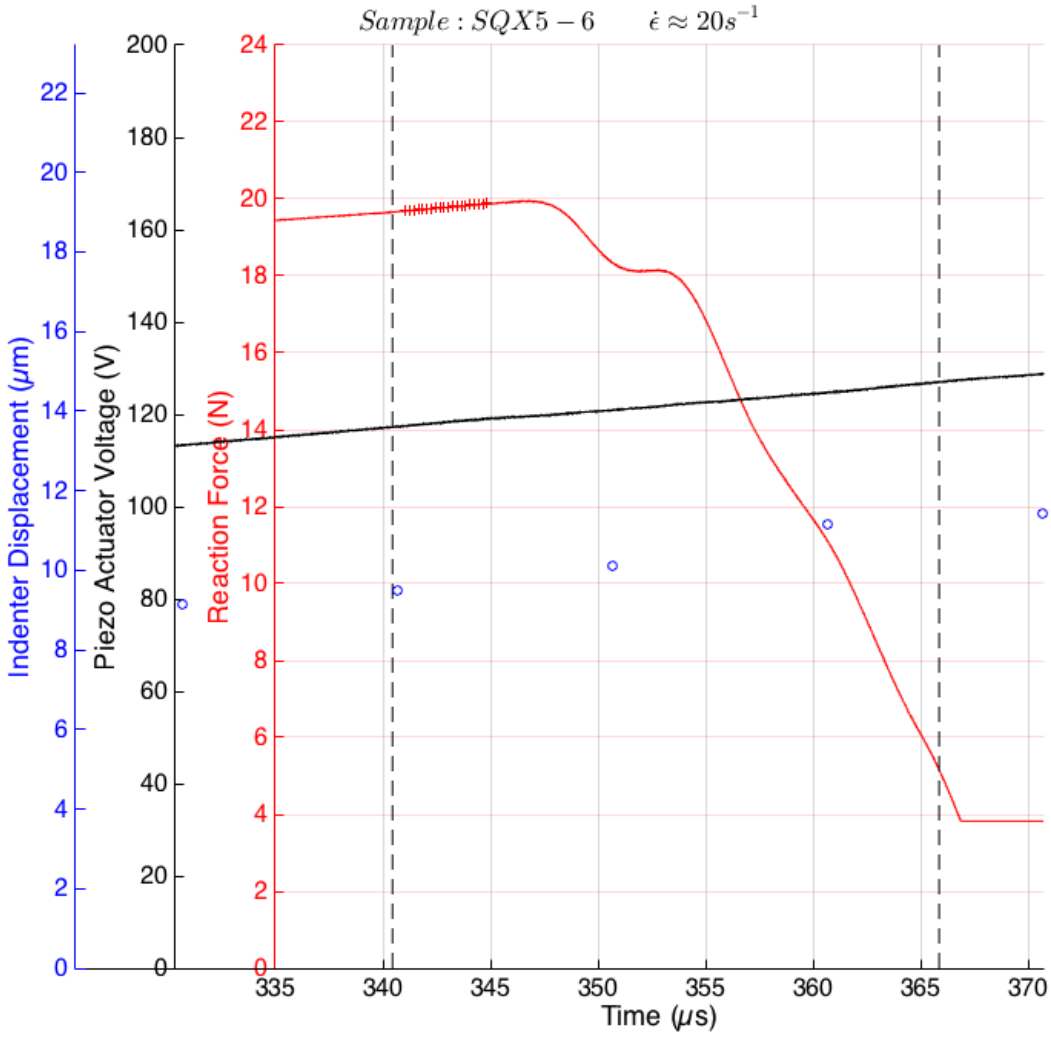

7.2.4.1.3 Figure 81- Vertical dotted lines indicate the beginning and end of the phase contrast imaging window. Small cluster of red markers on F(t) curve indicates the window from crack nucleation to complete fracture for t=[341.04, 345.04] μs

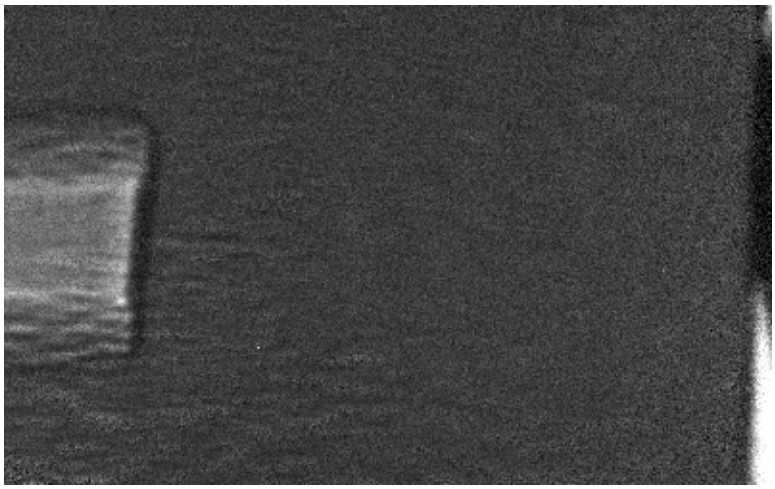

7.2.4.1.4 Figure 82- PCI image at t=341.04 μs

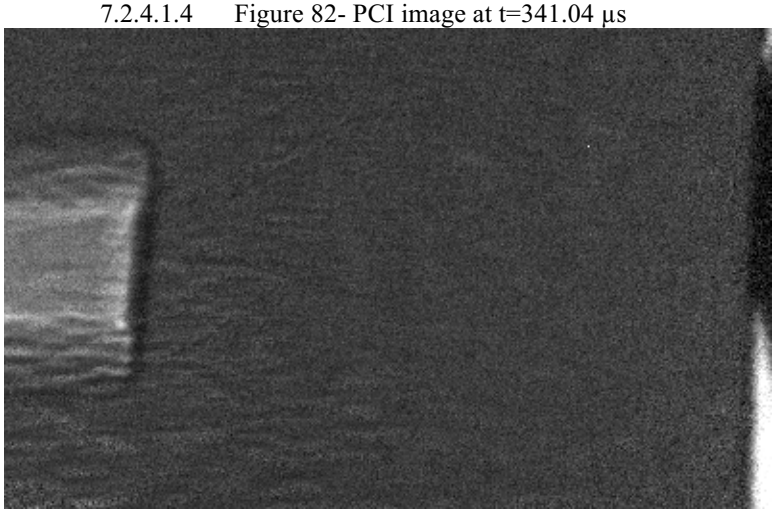

7.2.4.1.5 Figure 83- PCI image at t=341.84 μs

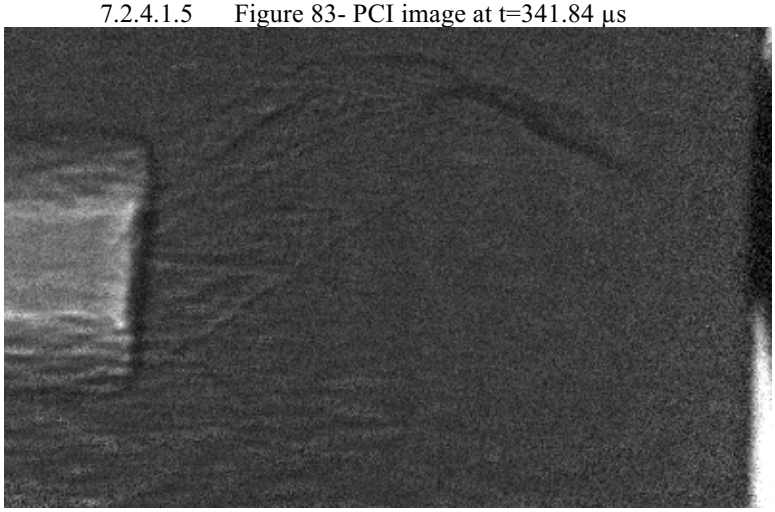

7.2.4.1.6 Figure 84- PCI image at t=343.44 μs

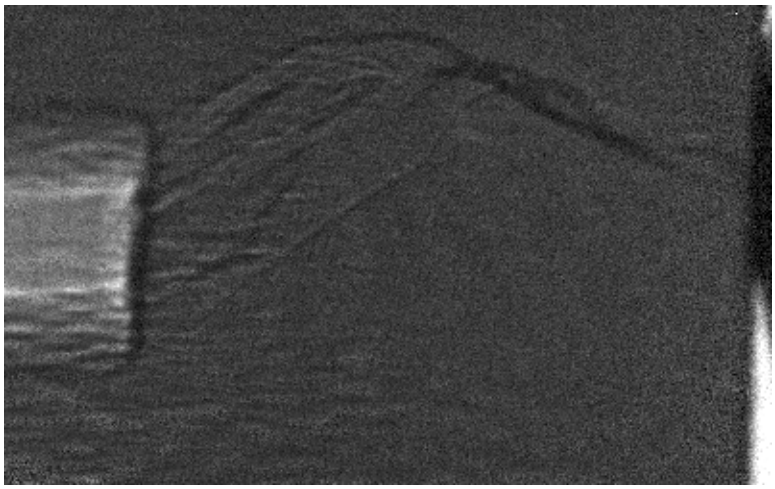

7.2.4.1.7 Figure 85- PCI image at t=345.04 μs

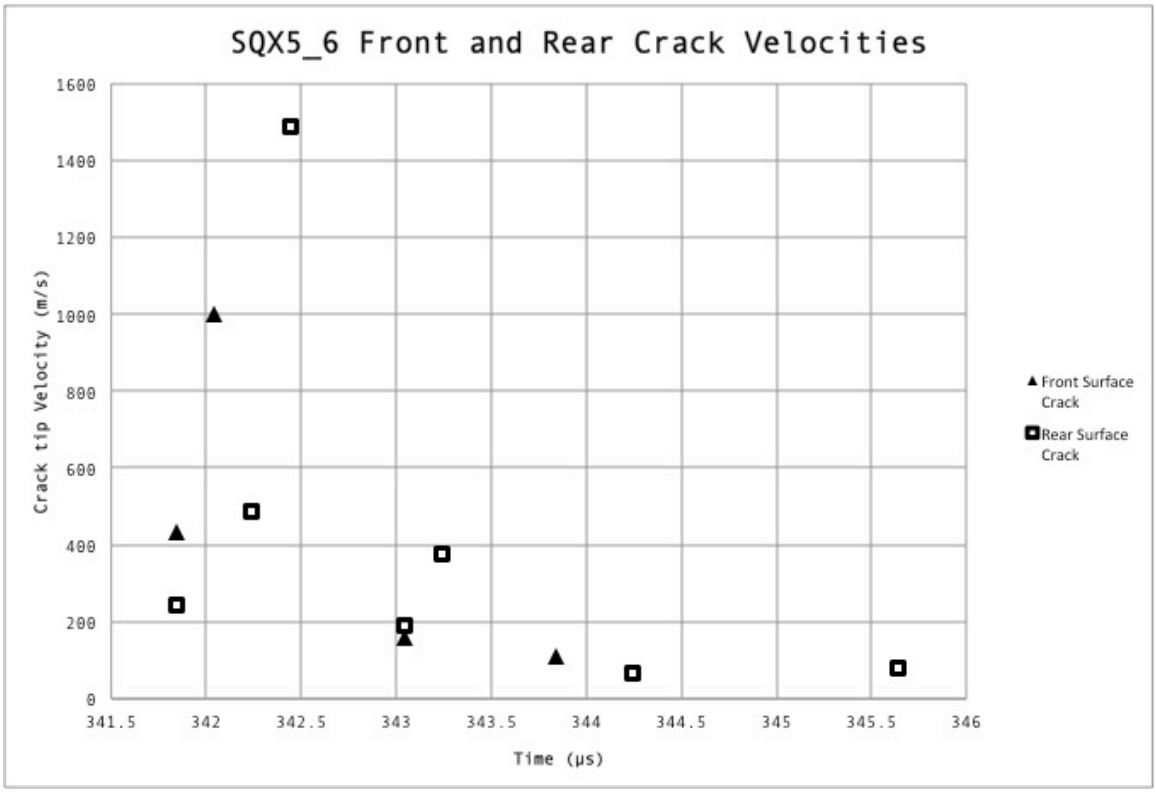

7.2.4.1.8 Figure 86- Crack velocities are shown based off estimated crack tip locations for frames that showed a significant change in crack tip location. Errors in SQX5 velocities are higher than SQX4 due to thicker samples and consequently less contrast.

7.2.5 SQX5_7

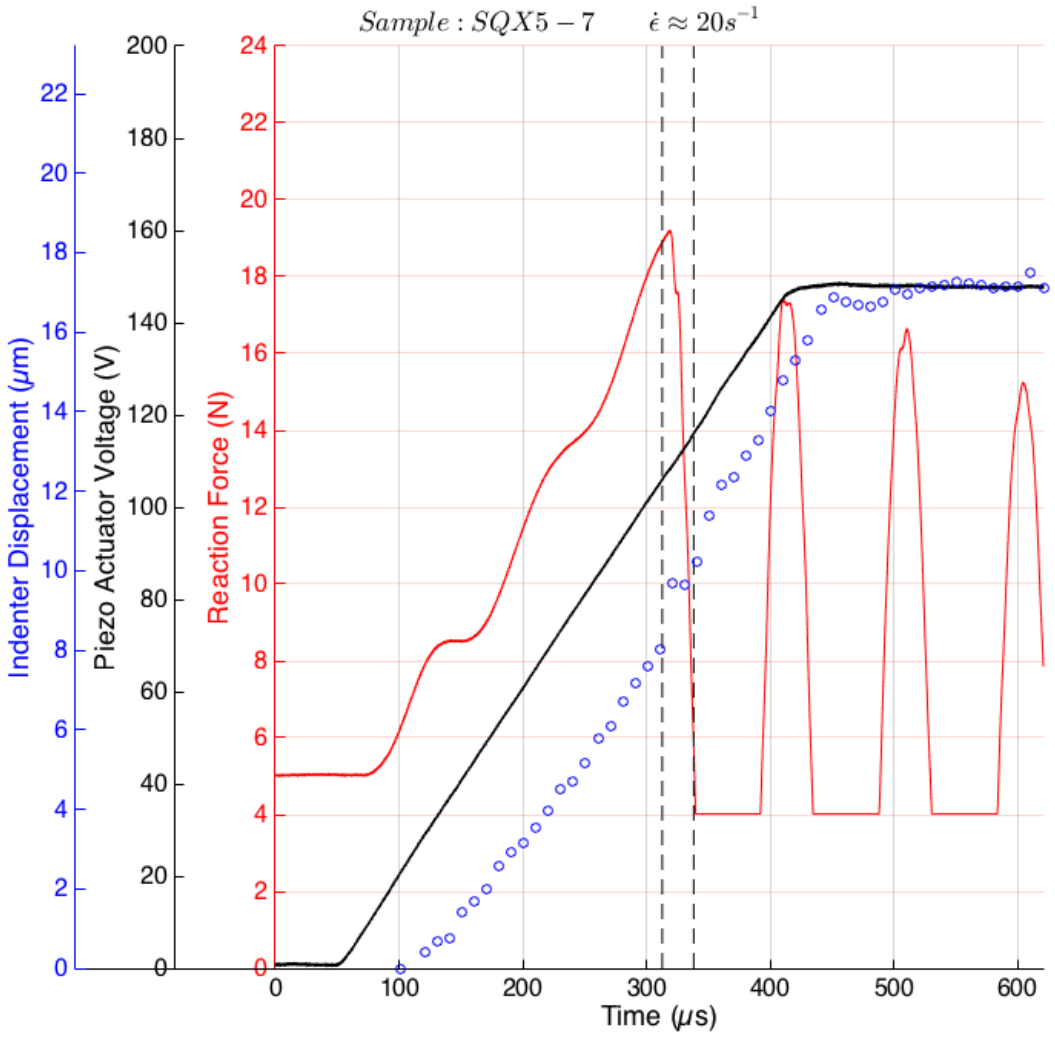

7.2.5.1.1 Figure 87- Actuator displacement was imaged at 100,000 fps. PCI images were taken at 16.146 keV. Sample preload was 4.88 N.

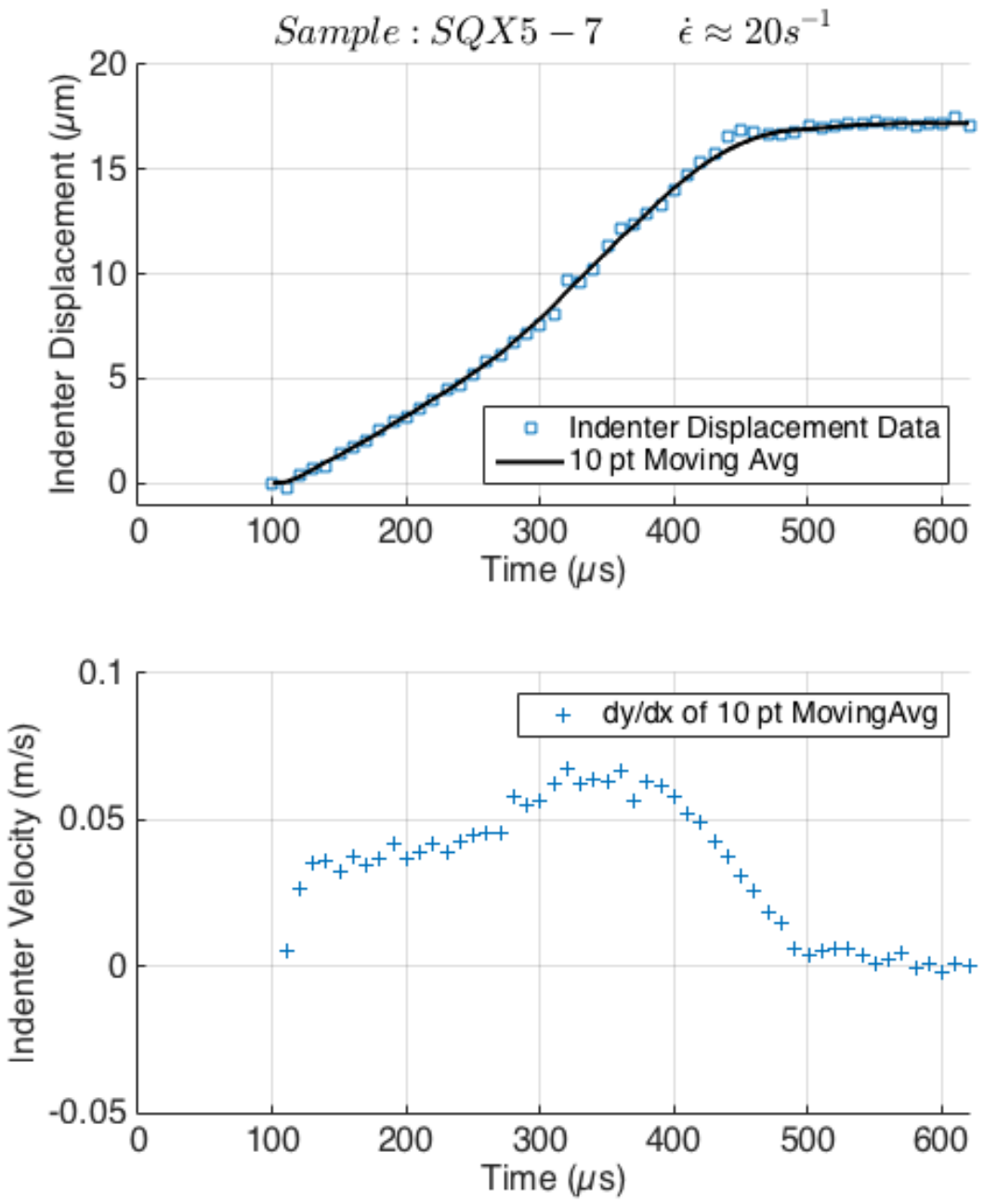

7.2.5.1.2 Figure 88- Top: Indenter displacement with a 10 pt moving average fit. Bottom: Indenter velocity generated from discrete derivatives of the 10 pt moving average fit.

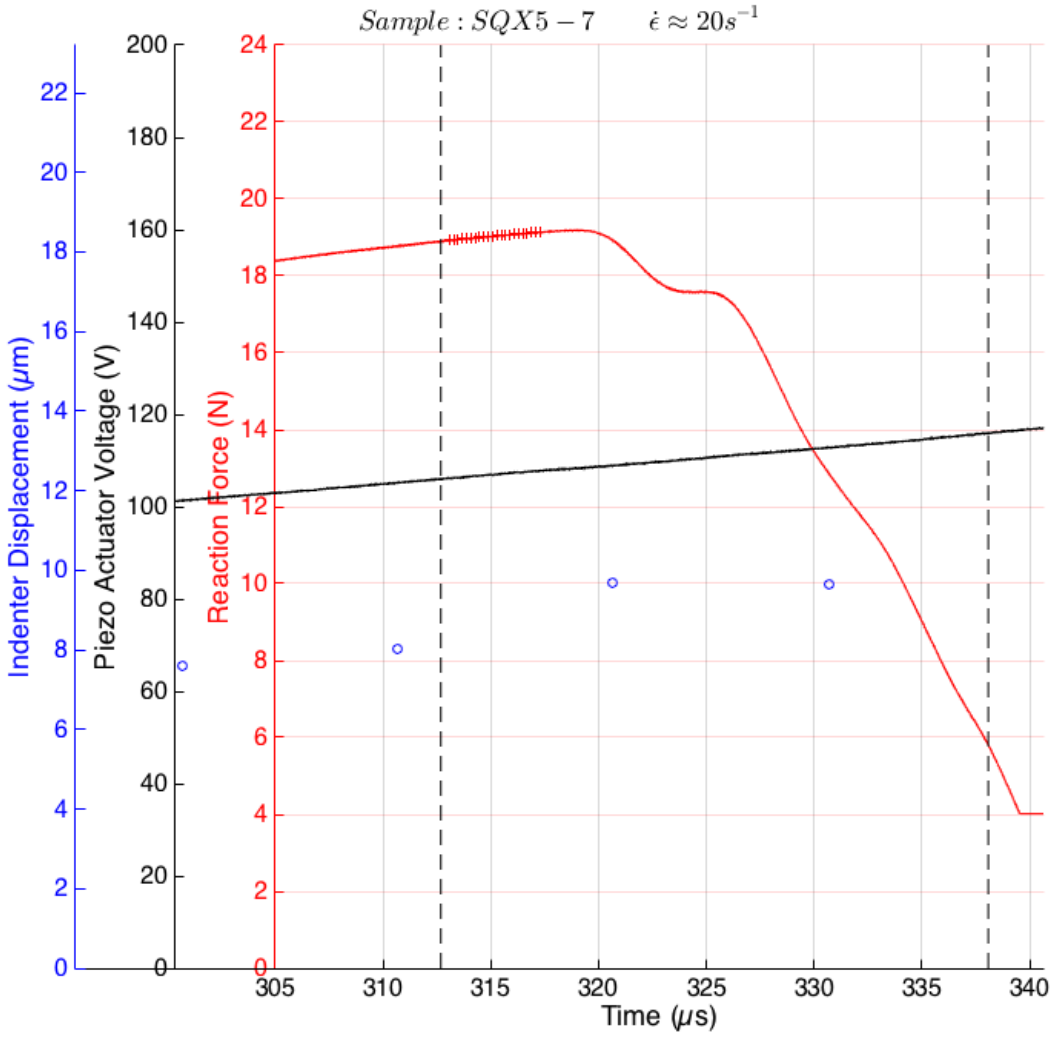

7.2.5.1.3 Figure 89- Vertical dotted lines indicate the beginning and end of the phase contrast imaging window. Small cluster of red markers on F(t) curve indicates the window from crack nucleation to complete fracture for t=[313.08, 317.48] μs

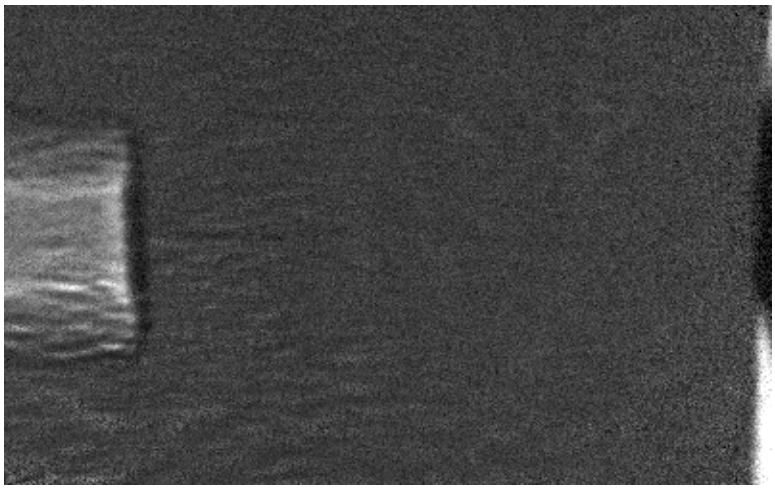

7.2.5.1.4 Figure 90- PCI image at t=313.08 μs

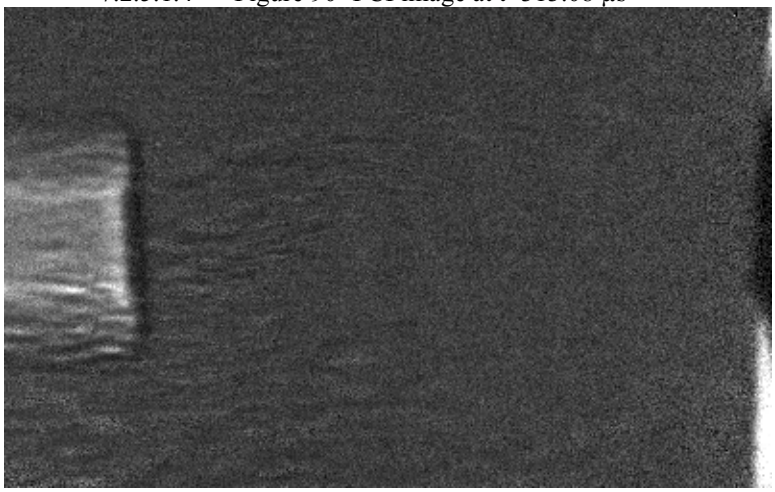

7.2.5.1.5 Figure 91- PCI image at t=314.88 μs

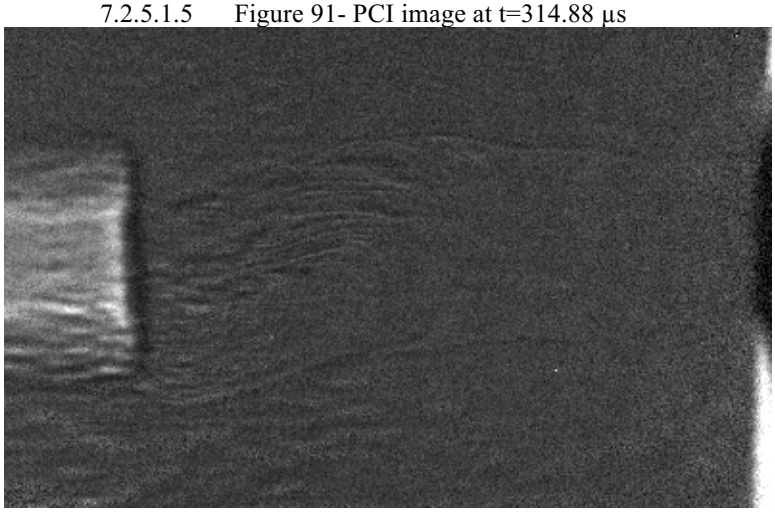

7.2.5.1.6 Figure 92- PCI image at t=316.68 μs

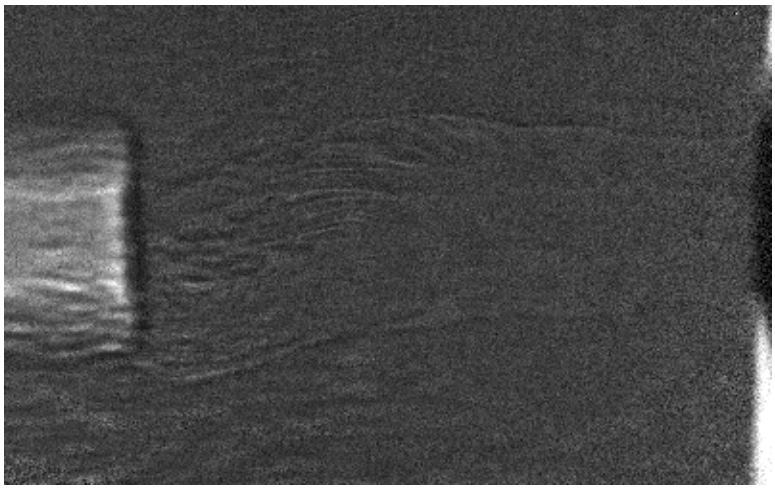

7.2.5.1.7 Figure 93- PCI image at t=317.48 µs

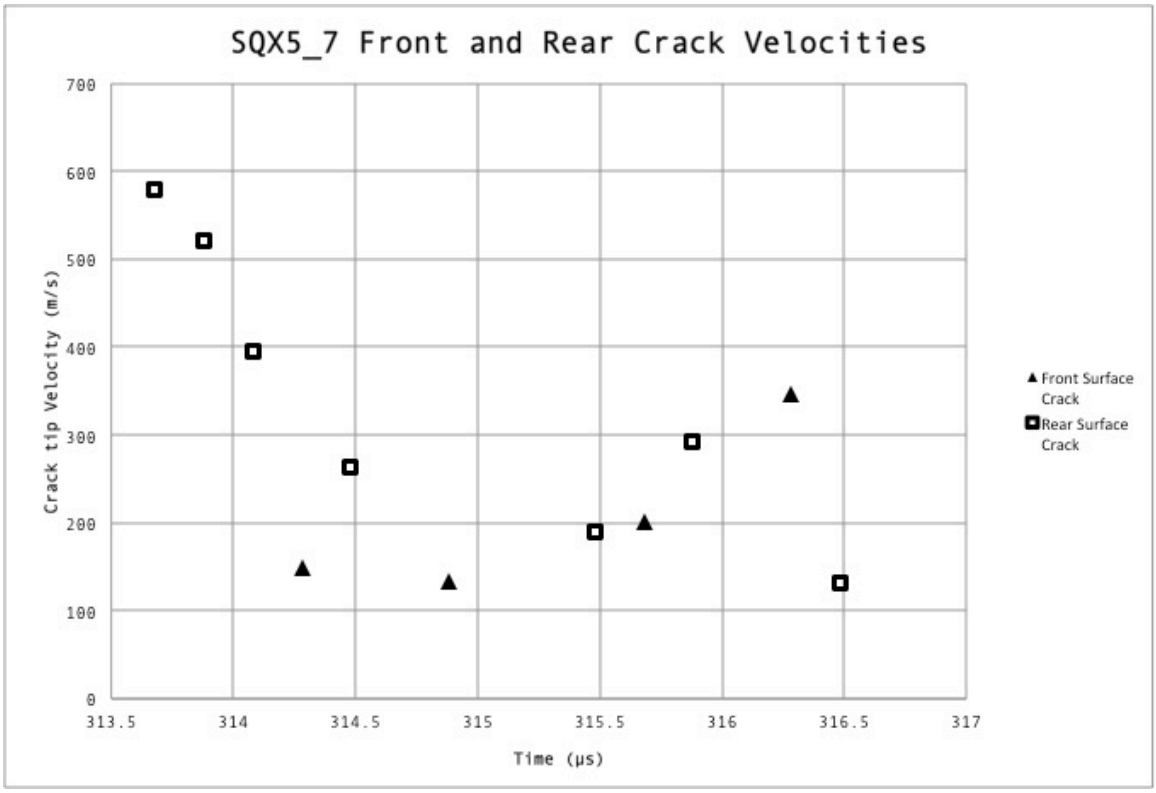

7.2.5.1.8 Figure 94- Crack velocities are shown based off estimated crack tip locations for frames that showed a significant change in crack tip location. Errors in SQX5 velocities are higher than SQX4 due to thicker samples and consequently less contrast.

7.3 Computational Results

7.3.1 Strain Rate Estimation

7.3.1.1 SQX4_3

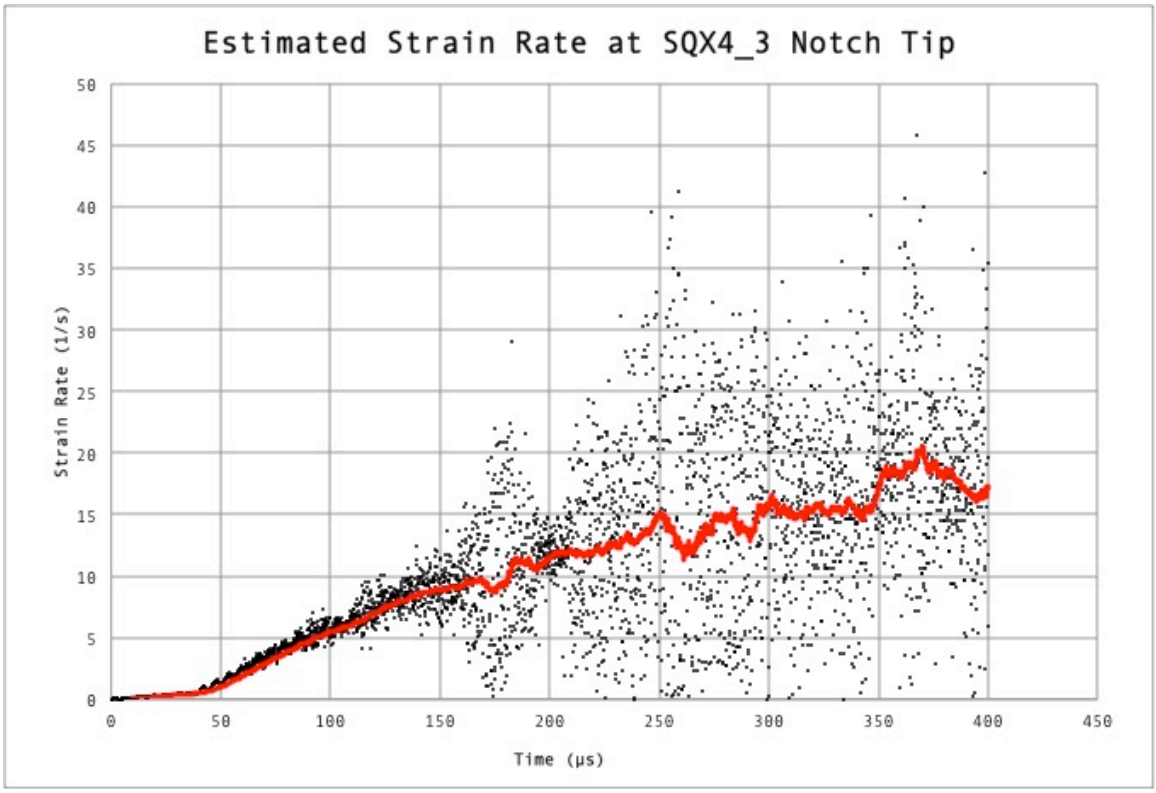

7.3.1.2 SQX4_7

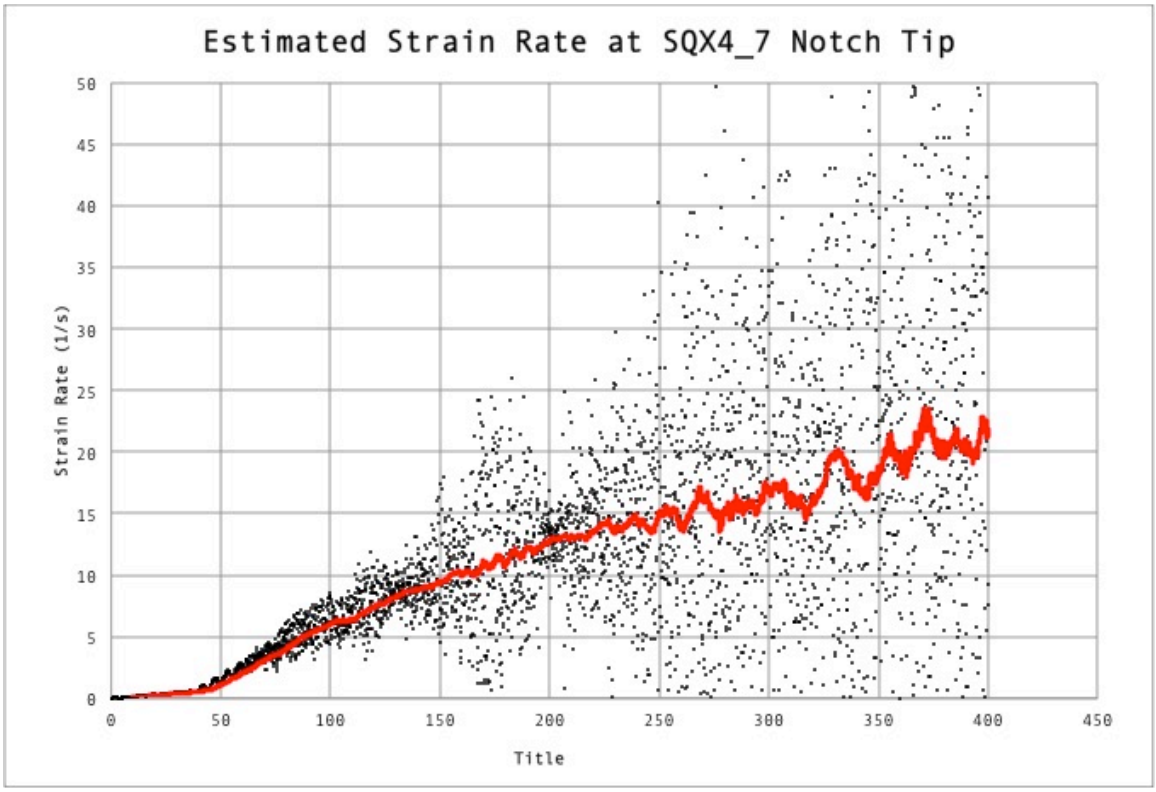
Estimated Strain Rate at SQX4_7 Notch Tip
Strain Rate (1/s)
Title
0
5
10
15
20
25
30
35
40
45
50
0
50
100
150
200
250
300
350
400
450

7.3.2 Input Rise Time Testing

7.3.2.1 SQX5 with 20 µs Pulse

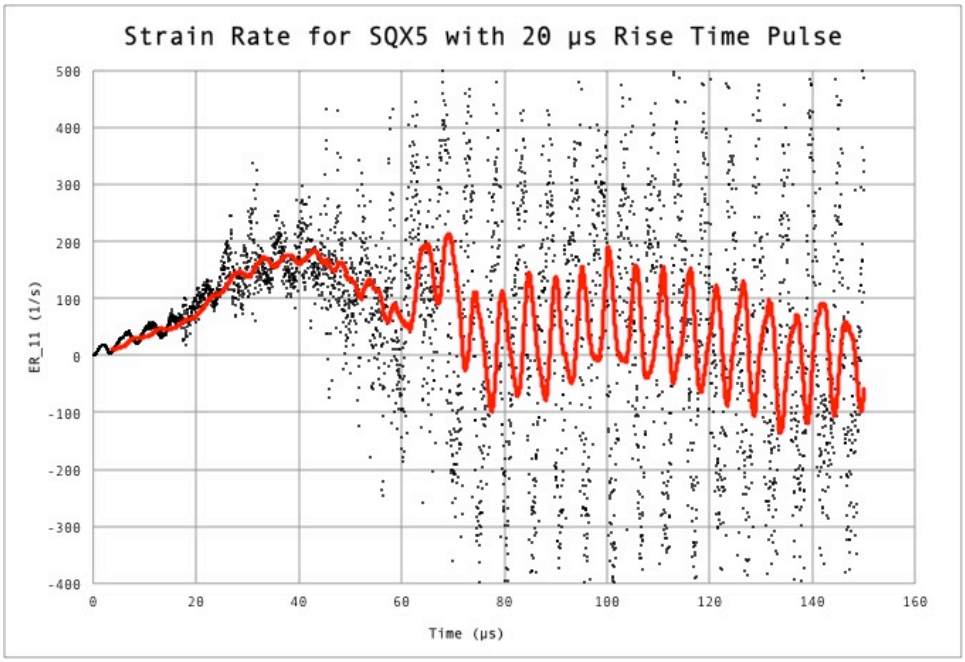

7.3.2.1.1 Figure 95- Red line is the 100-pt moving average of the raw discrete data. Peak strain rate is approximately 190 s^{-1} at roughly t=40 µs

7.3.2.2 SQX5 with 60 µs Pulse

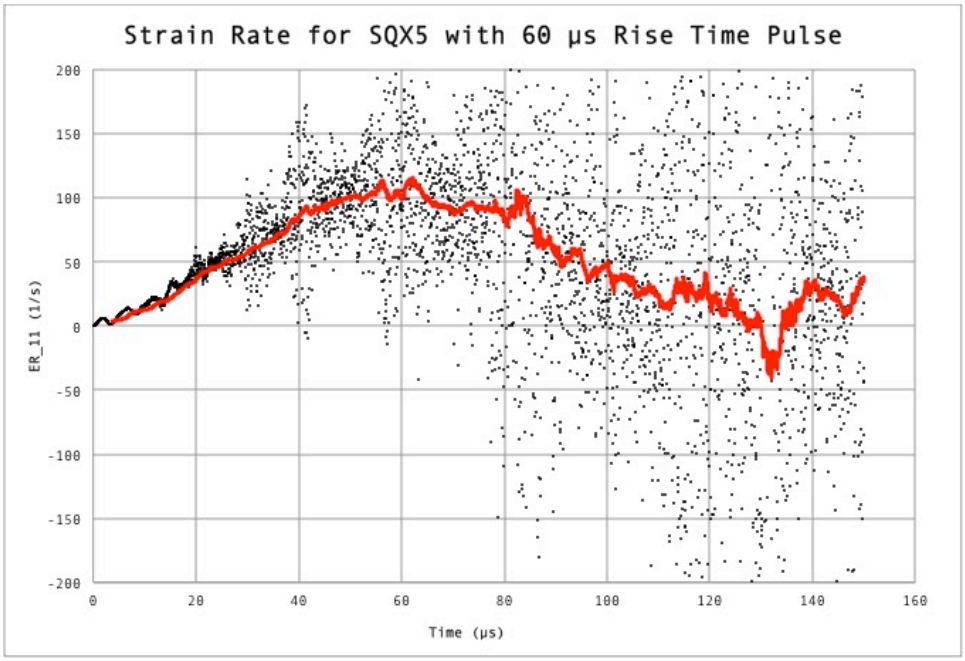

7.3.2.2.1 Figure 96- Red line is the 100-pt moving average of the raw discrete data. Peak strain rate is approximately 115 s^{-1} at roughly t=60 µs

7.3.2.3 SQX5 with 150 µs Pulse

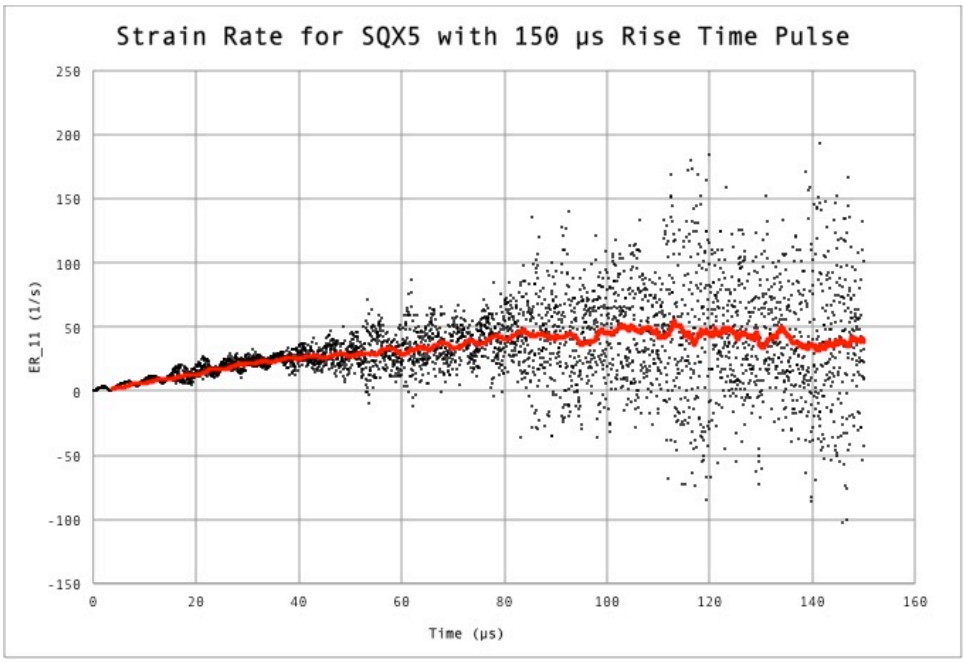

7.3.2.3.1 Figure 97- Red line is the 100-pt moving average of the raw discrete data. Peak strain rate is approximately 55 s^{-1} at roughly t=115 µs

ANDREW K. ROBINSON

5300 Iron Horse Parkway ◇ Dublin, CA 94568
(509) · 590 · 9660 ◇ andrewkrobinson@gmail.com

EDUCATION

Johns Hopkins University *2016*
M.S. in Mechanical Engineering, Fall 2016 graduation
Emphasis: Solid Mechanics
Thesis: Design, Construction, and Testing of an Intermediate Strain Rate Loading Device for Synchrotron-Based Testing of Geological Materials
Overall GPA: 3.28/4.0

Washington State University *2014*
B.S. in Mechanical Engineering
Minors: Materials Science and Engineering, Mathematics
Overall GPA: 3.43/4.0

EXPERIENCE

Lawrence Livermore National Lab September 2016 - Present
Materials Engineer, Materials Engineering Division *Livermore, CA*

- Improve instrumentation, sample design, and procedure for tests at the Advanced Photon Source, CHESS, and other synchrotron sources to study the properties of materials under dynamic loading conditions.
- Assist in other projects in the Mechanics of Materials Group when a knowledge of materials testing and in-situ characterization is needed

Johns Hopkins University August 2014 - September 2016
Research Assistant, Hopkins Extreme Materials Institute *Baltimore, MD*

- Characterize the microstructures of spark plasma sintered and hot-pressed boron carbides using SEM, EDS, EBSD, and optical techniques
- Develop image analysis code in MATLAB to quantify the microstructure of various boron carbides and measure time-resolved displacements of less than 20 microns with down to 500 ns interframe times
- Mechanically test the properties of commercial and university-sourced boron carbide specimens using quasi-static load frames and Kolsky bars
- Design a drop tower to investigate damage evolution (using APS sector 35 or sector 32) in single crystal quartz
- Investigate the effect of hydrostatic pressure (up to 500 MPa) on the porosity of JSC-1 lunar simulant using a quasi-static load frame

Idaho National Lab May 2013 - August 2013
Mechanical Engineering Intern, Armor Development Group *Idaho Falls, ID*

- Design a mounting platform for armor plate test samples that can withstand shocks from ballistics and explosives testing
- Help design experiments to test the multi-hit protection of ceramic armor arrays, the shock dispersion properties of steel/elastomer laminate armors, and the projectile erosion capabilities of bulging armor and semi-energetic armor systems
- Aid in ballistics testing at the National Security Test Range by helping with data acquisition, high speed camera footage, and assembly of test samples

- Present results of testing to customers, researchers, and managers using technical papers and research publications

Pacific Northwest National Lab January 2013 - May 2013
Engineering Consultant, Nonproliferation and International Security Group *Richland, WA*

- Work on a senior capstone project with a team of materials and mechanical engineering students at WSU to research, design, build, and test a large volume water sampler for collection of radionuclides to aid in international nuclear non-proliferation monitoring
- Write an operating and assembly manual so multiple units can be manufactured and shipped easily throughout the world for the International Atomic Energy Association's monitoring efforts

Washington State University November 2010 - January 2013
Research Assistant, Advanced Marine Vehicles Lab *Pullman, WA*

- Design, build and test experimental apparatuses to investigate phenomena associated with the operation of Air Assisted Marine Vehicles
- Write and help edit conference and journal papers published based on the findings of the experiments conducted in the lab

AWARDS

Whiting School of Engineering Fellow, Johns Hopkins University, 2014-2015
First Place, $500 Scholarship, MS&T Student Poster Competition, 2013
Semi-Finalist, $300 Scholarship, MS&T Student Speaking Competition, 2013
First Place, $500 Scholarship, WSU Undergraduate Research Oral Contest, 2011

PRESENTATIONS

Robinson, A.K., Munhollon, T., Farbaniec, L., Shaeffer, M., Haber, R., Ramesh, K.T., *Comparison Of Dynamic Strength and Failure Mechanisms Between Boron Carbides Processed by Hot Pressing and Spark Plasma Sintering Techniques*, International Conference and Exposition on Advanced Ceramics and Composites, Daytona Beach, FL, 2016.

Hogan, J.D., Robinson, A.K., Tilson, J., Krimsky, E., Ramesh, K.T., *On the Behavior of Fragmented Brittle Materials*, Society of Experimental Mechanics Conference, Costa Mesa, CA, 2015.

Robinson, A.K., *Using Al-PTFE Granular Composites and Natural Rubber for Semi-Reactive Armor*, Material Advantage Undergraduate Student Poster Competition, Materials Science and Technology Conference, Montreal, Quebec, Canada, 2013.

Robinson, A.K., *Using Al-PTFE Granular Composites for Energetic Reactive Armor Prototypes*, Material Advantage Undergraduate Student Speaking Contest, Materials Science and Technology Conference, Montreal, Quebec, Canada, 2013.

Robinson, A.K., *Polymers in Armor*, Idaho National Laboratory Summer Internship Poster Session, Idaho Falls, ID, 2013.

Robinson, A.K., *Slamming of Catamaran Hulls*, WSU Research Experience for Undergraduates Poster Symposium on Multi-scale Engineering, Pullman, WA, 2012.

Robinson, A.K., *Power Augmented Ram Vehicles*, WSU Undergraduate Oral Contest, Pullman, WA, 2011.

Matveev, K.I., Chaney, C., Robinson, A.K., *Novel Marine Vehicles with Air Assistance*, WSU Academic Showcase, Pullman, WA, 2011.

PUBLICATIONS

Hogan, J.D., Robinson, A.K., Tilson, J., Krimsky, E., Ramesh, K.T., *On the Behavior of Fragmented Brittle Materials*, Proceedings of the Society of Experimental Mechanics, Costa Mesa, CA, 2015.

Robinson, A.K., and Matveev, K.I., *Experimental Study on Water Entry of Catamaran Model Sections*, Journal of Engineering for the Maritime Environment, 207(2), pp. 190-193, 2013.

Chaney, C., Robinson, A.K., and Matveev, K.I., *Development of Air-Supported Amphibious Marine Transports*, Proceedings of ASNE Day: Naval Warfare - Critical Engineering Challenges, Arlington, VA, 2012.